

Reduced Graphene Oxide as Artificial Solid Electrolyte Interphase for Anodes of Aqueous Lithium Energy Storage Systems

by

Moin Ahmed

A thesis
presented to the University of Waterloo
in fulfillment of the
thesis requirement for the degree of
Master of Applied Science
in
Chemical Engineering

Waterloo, Ontario, Canada, 2018

©Moin Ahmed 2018

AUTHOR'S DECLARATION

I hereby declare that I am the sole author of this thesis. This is a true copy of the thesis, including any required final revisions, as accepted by my examiners.

I understand that my thesis may be made electronically available to the public.

Abstract

Rechargeable Aqueous Hybrid Battery (ReHAB) systems offer several advantages over the commercially available non-aqueous battery systems. The most noteworthy advantages include higher ionic conductivity, added safety, and more environmentally friendliness. However, the ReHAB exhibits faster capacity fading than their non-aqueous counterparts after repeated cycles of charge and discharge; this limits their wide-range commercial applications. Excessive corrosion of metallic anodes in the aqueous electrolyte and accelerated growth of dendrites during the charge/discharge processes are found to be the main reasons that severely impact the ReHAB's lifespan. In this work, we implement ultra-thin graphene film as artificial solid electrolyte interphase (SEI) on the anode of ReHAB to mitigate detrimental anode oxidation and suppress dendritic growth during battery operation.

First, we introduce the porous zinc anode into the ReHAB battery systems for the easier application of graphene coatings on the anode surface. Spectroscopy characterizations reveal that the porous anode has a significantly higher electrochemically active surface area than the commonly used planar zinc anode (a 15 μm by 15 μm area of porous anode have a surface area of 400 μm^2 compared to 225 μm^2 of the planar anode). Moreover, the porous anode displays higher wettability which makes it suitable for use in aqueous batteries. When compared to the batteries with the planar anode, batteries with the porous anode display a 32 % improvement in initial discharge capacity (136.28 mA h g⁻¹ for porous anode vs. 103.42 mA h g⁻¹ for planar anode) and higher cycling retention. Furthermore, batteries with the porous anode displayed a significantly higher discharge capacity at various C-rates ranging from 0.2C to 2C. Larger battery system (7 mA h) with the porous anode also shows an improvement in rate performance, which suggests the potential use of porous anode for large-scale commercial applications. Float charge and gas

evolution tests suggest that there is less hydrogen evolution during cycling in batteries with the porous anode. Electrochemical characterizations reveal that the porous anode exhibits lower corrosion current density and significantly better dendritic suppression than the planar anode.

Second, we introduce ultra-thin graphene films as artificial solid electrolyte interphase (SEI) on the surface of a porous zinc anode to improve the cycling stability of ReHAB system. The artificial SEI is fabricated at different thicknesses and areas ranging from $\sim 1 - 100$ nm and $\sim 1 - 10$ cm², respectively, via a Langmuir-Blodgett trough method, and deposited onto the surface of the porous zinc anode. Electrochemical characterizations show a significant reduction in corrosion current density (0.033 mAcm⁻² vs. 1.046 mAcm⁻² for the control), suppression of dendritic growth (~ 50 %) and reduction in charge transfer resistance (222 Ω vs. 563 Ω for the control) when artificial SEI is utilized. The aqueous battery system with the artificial SEI (100 nm thickness) on the anode also shows ~ 17 % improvement in cycling stability (82 % capacity retention after 300 cycles) compared to the control system. Comprehensive microscopy and spectroscopy characterizations reveal that the artificial SEI not only controls the ion transport between the electrolyte and the anode surface (lower corrosion) but also promotes a uniform deposition (less dendritic growth) of zinc on the anode.

Acknowledgments

The work herein was financially supported by Mitacs through the Mitacs Accelerate program and the University of Waterloo.

The author would like to acknowledge Professor Pu Chen for his valuable guidance and support throughout his master's program.

The author would also like to thank lab colleagues including Dr. Alireza Zehtab Yazdi, Dr. Jian Zhi, Aly Mitha, Wenlong Xiong, Dr. Tuan K.A. Hoang, Saad Saud Khan, Nathan Oh and Mathew Mars for their assistance and support.

The author would like to acknowledge his family, including his parents Munawar Ahmed and Mariam Siddiqa, and close friends for their love and support throughout the master's program.

Moreover, the author would like to acknowledge the thesis committee members, Professor Pu Chen, Professor Jeffrey Gostick, and Professor Irene Goldthorpe, for reviewing the thesis and providing valuable comments.

Table of Contents

AUTHOR'S DECLARATION	ii
Abstract	iii
Acknowledgments.....	v
List of Figures	x
List of Tables	xiv
List of Abbreviations	xv
Chapter 1: Aqueous Battery Systems: Introduction, Limitations, and Research Motivations	1
1.1 Introduction	1
1.2 Rechargeable Hybrid Aqueous Batteries	2
1.2.1 Limitations of Anode in Aqueous Batteries.....	5
1.2.2 Strategies to Overcome Anode Limitations in Aqueous Batteries	6
1.2.3 Strategies to Overcome Anode Limitations in Organic Lithium Batteries.....	7
1.3 Graphene Oxide and Reduced Graphene Oxide	12
1.3.1 Graphene Oxide	12
1.3.2 Graphene Oxide fabrication.....	13
1.3.3 Mechanism of Graphene Oxide Formation.....	15
1.3.4 Reduced Graphene Oxide	17
1.4 Reduced Graphene Oxide as Artificial Solid Electrolyte Interphase.....	18

1.5	Project Scope and Objectives	19
Chapter 2: Material and Electrochemical Characterization Techniques.....		21
2.1	Material Characterization Techniques	21
2.1.1	Scanning Electron Microscope	21
2.1.2	Atomic Force Microscope.....	23
2.1.3	X-ray Diffraction and Grazing Incidence X-ray Diffraction	25
2.1.4	X-ray Photoelectron Spectroscopy	28
2.1.5	Raman Spectroscopy.....	29
2.1.6	Contact Angle Measurement.....	30
2.2	Electrochemical Characterization Techniques.....	31
2.2.1	Tafel Characterizations	31
2.2.2	Chronoamperometry	33
2.2.3	Electrochemical Impedance Spectroscopy	34
2.2.4	Cyclic Voltammetry.....	35
2.2.5	Battery Testing.....	37
Chapter 3: Fabrication, Optimization, and Characterization of Porous Zinc Anode.....		39
3.1	Fabrication of Porous Zinc Anode.....	39
3.2	Optimization of Porous Zinc Anode.....	40
3.3	Characterization of Planar and Porous Zinc Anodes	42
3.3.1	Basic Characterizations.....	42

3.3.2 Battery Performance	45
3.3.3 Advanced Characterizations	48
3.4 Conclusions.....	55
Chapter 4: Graphene as Artificial Solid Electrolyte Interphase on Anode	57
4.1 Fabrication of Graphene coated Porous Zinc Anodes	57
4.1.1 Synthesis of Graphene Oxide.....	57
4.1.2 Fabrication of Porous Zinc Anodes	57
4.1.3 Coating of GO onto Porous Zinc Anode Surface	58
4.2 Basic Characterizations of RGO coating on Porous Zinc Anodes	61
4.3 Basic Electrochemical Characterizations.....	65
4.3.1 Linear Polarization Plot	65
4.3.2 Chronoamperometry	66
4.4 Battery Testing.....	68
4.4.1 Cyclic Voltammetry.....	69
4.4.2 Cycle Life.....	69
4.4.3 Rate Capability.....	73
4.4.4 Open Circuit Voltage	74
4.5 Advanced Characterizations	75
4.5.1 Electrochemical Impedance Spectroscopy	75
4.5.2 Scanning Electron Microscope	77

4.5.3 Raman Spectroscopy.....	82
4.5.4 X-ray Photoelectron Spectroscopy	83
4.5.5 Grazing Incidence X-ray Diffraction.....	86
4.6 Conclusions.....	87
Chapter 5: Summary of Thesis	89
References.....	93
Appendix.....	100
Appendix A: AFM Nano-indentation of graphene oxide (GO) layer.....	100
Appendix B: Rate performance of planar and porous zinc anode in 7 mAh batteries.....	101
Appendix C: Gas evolution test apparatus.....	102
Appendix D: XRD of porous anode before and after water vapor exposure.....	103

List of Figures

Figure 1: Demand for major battery systems over the past years [1]	1
Figure 2: Electrochemical window of various anode and cathode materials [7]	3
Figure 3: Working principle of the ReHAB during battery operation [7]	4
Figure 4: CV of the ReHAB showing the potential of redox processes [7]	5
Figure 5: Optical microscope of zinc dendrites growing from the anode surface after cycling and piercing the glass fiber separators in ReHAB system.....	6
Figure 6: SEM image of Li deposition on (A) Bare Cu electrode (B) Cu electrode with graphene coating [22]	10
Figure 7: SEM image of Li deposition after cycling on (A) separator and (B) doped graphene coated separator after 200 cycles [26]	10
Figure 8: SEM images of Li-ion deposition on Cu anode after using (a) separator (b) GO coated separator [27]	11
Figure 9: Schematic of Li-ion deposition in the presence of GO barrier [27].....	12
Figure 10: Chemical structure of GO-based on Lerf-Klinowski model [30].....	13
Figure 11: Schematics of mechanisms involved in the conversion of graphite to GO [35]	16
Figure 12: Proposed chemical structure of RGO [41]	17
Figure 13: Schematic of SEM instrument, including electron gun, column of lenses, sample chamber and detectors [50].....	22
Figure 14: Basic operation of AFM [52]	24
Figure 15: (A) Schematic of XRD instrument [55] (B) illustration of Bragg's diffraction, each horizontal line represents a crystal plane [56]	26

Figure 16: Illustration of x-ray diffraction conducted at (A) high and (B) low incidence angle [58]	27
Figure 17: (A) Schematic of XPS instrument (B) principle of the emission of photoelectron [59]	28
Figure 18: (A) Schematic of Raman instrument, and (B) vibrational energy levels [61].....	30
Figure 19: Apparatus for measuring the contact angle	31
Figure 20: Illustration of Tafel extrapolation on linear polarization curve. The intersection of anodic and cathodic Tafel slope gives corrosion potential and corrosion current density [64]....	32
Figure 21: (A) Waveform where chemical species under investigation is inactive at E_1 but is reduced at E_2 , (B) concentration profiles at different times, and (C) current-time profile [65] ...	34
Figure 22: (A) Potential scan with time (B) Resulting CV plot [65].....	36
Figure 23: Cycle life of anodes consisting of (A) different zinc powder types at 1C (B) different binder concentrations at 1C (C) different purum zinc powder sizes at 4C.....	41
Figure 24: SEM images of (A) planar and (B) porous zinc anodes.....	42
Figure 25: AFM images of (A) planar and (B) porous zinc anodes	43
Figure 26: Contact angle measurement of (A) planar and (B) porous zinc anodes.....	44
Figure 27: Cycle life of planar and porous zinc anode under a current density of 1C	45
Figure 28: Discharge capacity at different C-rates of planar and porous zinc anodes	47
Figure 29: Float charge current profile for planar and porous anode after 72 hours	48
Figure 30: Tafel plot of planar and porous zinc anodes.....	49
Figure 31: Current-time profile of planar and porous zinc anodes for 10 seconds.....	51
Figure 32: Current-time profile of planar and porous zinc anodes for 1 hour	52
Figure 33: SEM images of (A) planar and (B) porous zinc anodes after 1 hour of CA	52

Figure 34: CV plot of planar and porous zinc anodes	53
Figure 35: XRD of planar and porous zinc anodes before and after 1 hour of CA	54
Figure 36: Illustration of Langmuir trough instrument with a (1) balance, (2) trough, (3) barriers, (4) layer-builder, (5) dipper and (6) well	58
Figure 37: Surface pressure as a function of the trough area in the Langmuir trough method. Inset: Schematic of the Langmuir trough coating technique used in this work.....	60
Figure 38: SEM images of (A) blank (B) 10RGO and (C) 100RGO	62
Figure 39: Figure 12: EDX results of (A) blank (B) 10RGO and (C) 100RGO.....	63
Figure 40: AFM images of blank (left) and 100RGO (right)	63
Figure 41: Contact angle measurements of (A) blank (B) 100GO and (C) 100RGO.....	64
Figure 42: Tafel plot of blank and RGO coated porous zinc anodes.....	66
Figure 43: Current-time profile of blank and RGO coated porous zinc anodes for 30 seconds...	67
Figure 44: Current-time profile of blank and RGO coated porous zinc anodes for 1 hour	68
Figure 45: CV profile of Blank and RGO coated porous zinc anodes at a scan rate of 1 mV s^{-1} .	69
Figure 46: (A) Cycle life and (B) retention in discharge capacity of blank and RGO coated porous zinc anodes.....	71
Figure 47: Charge-Discharge curves of blank and 100RGO after 1 st and 300 th cycle.....	73
Figure 48: Discharge capacity at different C-rates of blank and RGO coated porous zinc anodes	74
Figure 49: Self-discharge curves of blank and RGO coated porous zinc anodes for 72 hours	75
Figure 50: Nyquist plots of blank and RGO coated porous zinc anodes after (A) first cycle and (B) 300 cycles.....	77

Figure 51: SEM images of (A) blank (B) 10RGO and (C) 100RGO after 170 milliseconds of CA	79
Figure 52: SEM images of (A) blank (B) 10RGO and (C) 100RGO. (D) 10RGO (demagnified) after 1 hr of CA.....	80
Figure 53: SEM images of (A) blank and (B) 100RGO after 300 battery cycles.....	81
Figure 54: Angled SEM image of 100RGO (A) before and (B) after 1 hour of CA	81
Figure 55: Raman of blank, 10RGO, and 100RGO before and after 1 hour of CA	83
Figure 56: Sample XPS survey	84
Figure 57: High-resolution XPS of Zn 2p (3/2) of blank and 100RGO before and after 1 hour of CA.....	86
Figure 58: GIXRD characterizations on blank and 100RGO anodes before and after 1 hour of CA	87
Figure 59: Picture showing (a) inner and (b) outer part of 7 mAh battery with a cathode surface area of 9cm ² [91].....	101
Figure 60: Discharge capacity at different C rates of planar and porous zinc anodes in 7 mAh batteries	101
Figure 61: (A) inside and (B) outside of gas evolution apparatus	102
Figure 62: XRD of the porous anode before and after 5 hrs of water vapor exposure.....	103

List of Tables

Table 1: Image surface area, average roughness (R_a) and root mean square roughness (R_q) of planar and porous zinc anodes	44
Table 2: Summary of discharge capacity (mA h g^{-1}) and retention (%) of planar and porous zinc anode after every 100 cycles.....	46
Table 3: Summary of corrosion potential and current density extrapolated from Tafel fit	49
Table 4: Summary of corrosion potential and current density extrapolated from fitting Tafel extrapolation	66
Table 5: Summary of initial discharge capacity and percent retention in discharge capacity after 300 cycles at the current density of 4C.....	72
Table 6: Summary of the elemental composition obtained from XPS	85
Table 7: Modulus of control (substrate) and GO coating	100

List of Abbreviations

AFM	Atomic Force Microscopy
Ag/AgCl	Silver chloride reference
CA	Chronoamperometry
CV	Cyclic Voltammetry
EIS	Electrochemical Impedance Spectroscopy
GIXRD	Glazing Incidence X-ray Diffraction
GO	Graphene Oxide
LIBs	Lithium-Ion Batteries
ReHABs	Rechargeable Hybrid Aqueous Batteries
RGO	Reduced Graphene Oxide
SEI	Solid Electrolyte Interphase
SEM	Scanning Electron Microscopy
XPS	X-ray Photoelectron Spectroscopy
XRD	X-ray Diffraction

Chapter 1: Aqueous Battery Systems: Introduction, Limitations, and Research

Motivations

1.1 Introduction

The growing global energy crisis, primarily due to the limited supply of non-renewable energy sources, has increased the drive to find environmentally friendly energy sources. This crisis has led to intense research in areas of green transportation and renewable energy generation systems. Green transportations, such as electric and hybrid electric vehicles, and renewable energy generation systems, such as wind and solar energy power plants, require the use of batteries to store electricity in chemical form. Figure 1 shows the steady increase in demand for batteries over the last years. It also shows the battery systems with dominant battery market share, which are lithium-ion (LIB), nickel metal hydride (NiMH) and nickel cadmium (NiCD) and lead-acid batteries.

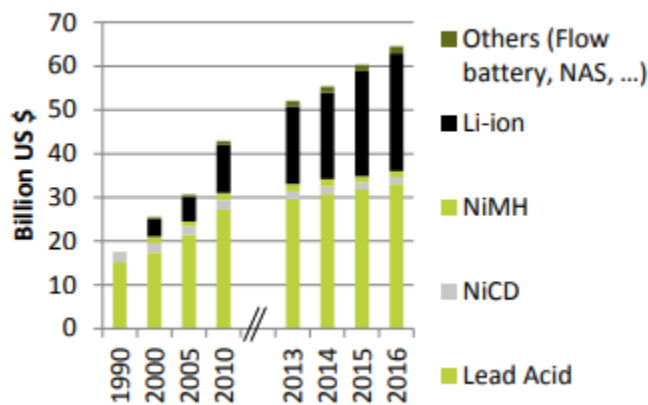


Figure 1: Demand for major battery systems over the past years [1]

However, these major commercially available battery systems pose several economical, ecological and safety issues. For example, the lead-acid and NiCD batteries use highly toxic metals, such as

lead and cadmium, which make their assembly and disposal a primary environmental concern [2]. Moreover, the main environmental risk with lead-acid batteries is the leakage of sulfuric acid electrolyte [3]. The manufacturing of NiMH batteries are expensive and has an adverse negative environmental impact [4]. Furthermore, it uses nickel which is toxic to plants. The LIBs use toxic and flammable electrolyte, which makes its assembly, and use a safety hazard. Furthermore, LIB's battery assembly requires stringent conditions because its electrolyte is sensitive to air and moisture [5]. In contrast, aqueous battery systems, which use aqueous electrolytes, can overcome some of the limitations posed by the major commercially available battery systems. Aqueous battery systems use safer materials, are easy to assemble, and manufacture. Moreover, compared to the organic electrolyte, aqueous electrolytes have about two orders of magnitude higher ionic conductivities. Hence, aqueous battery systems have good rate performance and low over-potential [6].

1.2 Rechargeable Hybrid Aqueous Batteries

Rechargeable Hybrid Aqueous Battery (ReHAB), a class of aqueous battery, were developed by Chen's research group [7]. This battery system uses zinc metal as the anode and lithium manganese oxide (LiMn_2O_4) as the cathode material. Its electrolyte consists of an aqueous solution containing lithium and zinc ions at pH 4. Zinc, while being abundantly available and economical, has low redox potential, high reversibility, and requires high potential for detrimental hydrogen evolution in acidic solution [8]. LiMn_2O_4 , a popular cathode material for lithium-ion batteries, has a spinal structure which facilitates lithium ion insertion and extraction during battery charge and discharge cycles [9]. ReHAB systems exhibit a high operating potential of 2 V because, at pH 4, the operating potential between zinc and LiMn_2O_4 is 2 V (Figure 2). Furthermore, the ReHAB have a practical energy density of 50-80 Wh kg^{-1} .

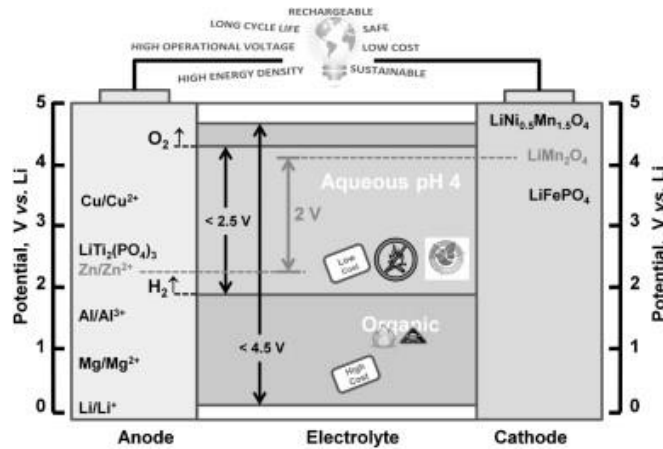


Figure 2: Electrochemical window of various anode and cathode materials [7]

Figure 3 illustrates the working principle involved during the charge and discharge of the ReHABs. When the ReHAB battery is charging, lithium de-intercalates from the crystals of LiMn_2O_4 cathode. Meanwhile, zinc ions from the electrolyte gain an electron from the anode and deposits on the anode as zinc metal. Similarly, during discharge lithium ions in the electrolyte intercalates into the cathode and zinc dissolves into the electrolyte as zinc ions. These batteries are called hybrid because during charge and discharge two types of chemistries, namely de-intercalation/intercalation (on the cathode) and deposition/dissolution (on the anode), happens simultaneously.

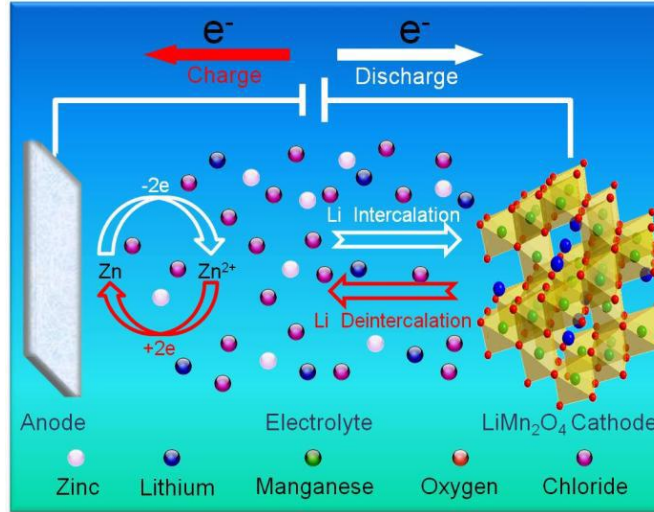
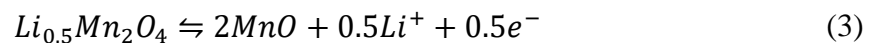
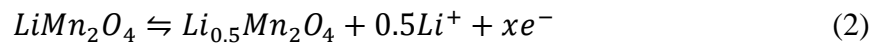


Figure 3: Working principle of the ReHAB during battery operation [7]

Figure 4 shows the cyclic voltammetry profile of the ReHABs versus Zn/Zn^{2+} . It shows the redox processes involved in ReHAB at different potentials. Peaks observed at 0V are associated with zinc deposition/dissolution. Zinc deposition (during charge) and dissolution (during discharge) follow the equation:



Peaks observed at 1.76 V and 1.9 V are associated to two-step reaction during lithium deintercalation (during charge)/intercalation (during discharge) into $LiMn_2O_4$ cathode [10], the reactions are given as [11]:



Both these redox processes are highly reversible, which makes the ReHAB a secondary battery. Furthermore, the peaks at -0.5 V and 2.2 V are associated with hydrogen and oxygen evolution, respectively. These potentials indicate the limit of stability of electrolyte, as surpassing these potentials will result in water decomposition in the electrolyte.

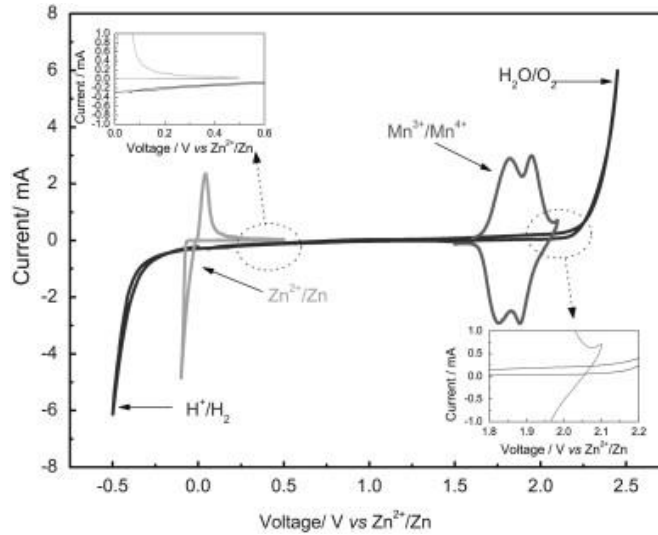


Figure 4: CV of the ReHAB showing the potential of redox processes [7]

1.2.1 Limitations of Anode in Aqueous Batteries

During cycling, the zinc anode undergoes metal corrosion and dendritic growth [12] which results in the capacity fading and short cycle life of the batteries [13]. In ReHABs, zinc anode is in direct contact with an acidic medium which results in zinc corrosion [14]. This corrosion leads to capacity fading in the ReHAB due to the following two reasons. First, corrosion leads to the production of hydrogen gas bubbles on the surface of a zinc anode and hence less electrolyte is in contact with the zinc anode surface. Second, corroded regions on the anode surface cannot be utilized for redox reactions for battery operation [15]. Second, during charging of the ReHAB, zinc ions from the electrolyte deposit on the anode surface as zinc metal. However, this electrodeposition of zinc on the anode surface is not uniform because of apparent anode surface roughness, which results in

current density localization. This situation leads to the formation of sharp needle zinc depositions (Figure 5). After successive charge cycles, these dendrites grow laterally, pierces the separator as they grow and can, eventually, make contact with the cathode. This contact leads to short-circuiting and failure of the ReHAB. This situation can also cause a safety issue due to the uncontrolled release of energy [16].

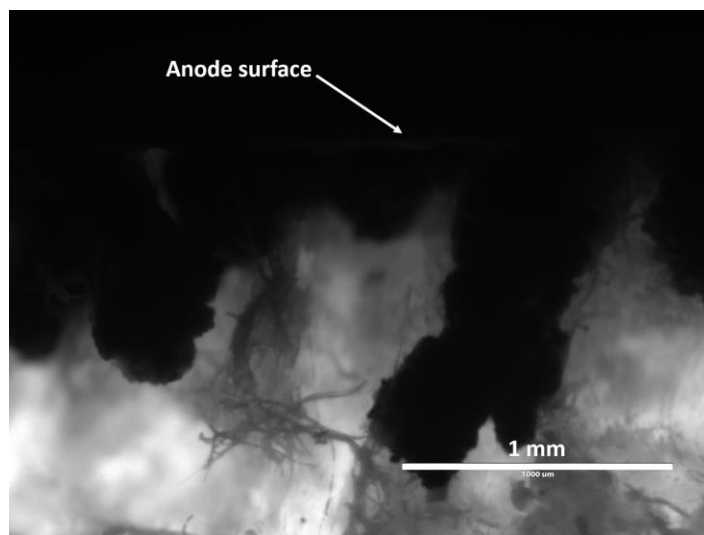


Figure 5: Optical microscope of zinc dendrites growing from the anode surface after cycling and piercing the glass fiber separators in ReHAB system

1.2.2 Strategies to Overcome Anode Limitations in Aqueous Batteries

Many strategies have been applied to overcome dendritic growth and surface oxidation limitations (see Section 1.2.1) faced by the anode of the ReHAB, Most noteworthy strategies to mention, include the use additives in the electrolyte, electroplate additives on zinc anode, and replacement the aqueous electrolyte with gel electrolyte.

Aly et al. reported an improvement in cycling performance of the ReHAB battery system when polyethylene glycol (PEG, the molecular weight of 200) was used as an additive in electrolyte [17]. Adding PEG additive to the electrolyte mitigates the oxidation of the zinc anode.

Furthermore, the specific interactions of PEG molecules with the zinc anode surface during battery charging suppresses the zinc dendrites.

Sun et al. reported the use of various organic additives that were electroplated with zinc to form the respective anodes [13]. Various additives, which includes cetyltrimethylammonium bromide (CTAB), sodium dodecyl sulfate (SDS), polyethylene glycol (PEG, the molecular weight of 8000), and thiourea (TU), were added individually to an aqueous solution containing zinc sulfate. These solutions were electroplated on a brass substrate. They reported an improvement in corrosion rate and dendrite suppression of anodes with SDS, PEG and TU anodes, which resulted in improved cycling performance of the batteries containing these anodes.

Tuan et al. demonstrated that replacing aqueous electrolyte with a gel electrolyte, containing pyrazole additives, mitigates some of the corrosion and dendritic growth during battery cycling [18]. The aqueous electrolyte was mixed with fumed silica and varying concentrations of pyrazole additive to create gel electrolyte. Fumed silica gel minimizes the dendritic growth in the anode. However, it also increases its corrosion. Hence pyrazole was added as a corrosion inhibitor. Applying this electrolyte in the ReHAB system, significantly improved its cycling performance life. Tuan et al. also used lead ions (Pb^{2+}) as the additive in the gel electrolyte for the ReHABs [19], which also improved cycling performance.

1.2.3 Strategies to Overcome Anode Limitations in Organic Lithium Batteries

Lithium metal (Li-metal) batteries faces a similar problem of dendritic growth and research community have explored and employed some strategies to address it. One common strategy is to add additives in the electrolyte to suppress dendritic growth in lithium batteries. When the organic electrolyte is used, a solid electrolyte interface (SEI) naturally forms on the anode surface during

battery cycling. These additives aid in strengthening this SEI layer which can act as a barrier to dendritic growth. The use of a wide variety of chemical species as SEI additives have been reported. Lee et al. introduced organic SEI additive Triacetoxyvinylsilane (VS) into the electrolyte in the Li-metal batteries [20]. Authors of this work concluded that VS made the SEI formation more uniform on the anode surface and provided mechanical strength to it. This added mechanical strength resulted in dendritic suppression and ultimately improvement cyclability of Li-metal batteries. Ding et al. used metal cations (e.g., cesium and rubidium) in the electrolyte as additive SEI [21]. During charging, these cations get electrostatically attracted and, as a result, adhere to the surface of the dendrite's tip. The presence of these cations repels the incoming Li-ions, which are forced to deposit on the areas adjunct to the growing dendrites. This deposition leads to a more uniform Li-ion deposition. This electrolyte displayed a more stable cycle life in Li-metal batteries. However, despite the added mechanical strength aided by the additives, the SEI of these batteries eventually disintegrate after many successive cycles of lithium plating/stripping [22].

Another popular approach involves the use of a composite separator with a ceramic material to inhibit dendritic growth. The idea of this approach is that adding ceramic to separator will increase the mechanical strength of the separator. Hence, it can act as a physical barrier to stop the dendrites from piercing through it. Park et al. fabricated a porous, flexible and mechanically robust composite separator containing alumina (Al_2O_3) and polyethylene glycol (PEO) [23]. Electrochemical tests followed by SEM images show that dendrites are stopped from penetrating through the composite separator. This composite separator was optimized for use in lithium and sodium redox flow batteries and improvement in cycle life was reported. Similarly, Professor Archer's research group reported the use of a separator that consists of alumina layer laminated between poly (vinylidene fluoride-co-hexafluoropropylene) (PVDF-HFP) polymer layers in

lithium metal batteries (the anode of lithium metal battery is lithium metal) [24]. This separator exhibited high mechanical strength from alumina, while polymer layers added to its flexibility. The batteries, which used this separator, showed good ionic transport and stable cycle life for over 1000 cycles. The use of ceramic particles other than alumina in the separator has also been reported. In Wang et al. work, a thin layer of silica (SiO_2) and polyethyleneimine (PEI) was coated on the surface of polyethylene (PE) separator [25]. An improvement in cycling performance, notably in initial discharge capacity and capacity retention, was observed. However, the fabrication of these separators requires an elaborate and time-consuming procedure that limits their practical large scale use. Moreover, batteries that use these separators suffer from low ionic conductivity and high interfacial impedance. These ceramic layers are usually thick and add to the weight of the batteries and decrease their energy density.

Another approach is to use the 2D material to suppress dendritic growth in Li-metal batteries. Two-dimensional materials are substances with a thickness in few nanometer ranges, for example, graphene, boron nitride, and phosphorene. Yan et al. coated 2D materials, hexagonal boron nitride (h-BN) and graphene onto the copper metal current collector [22]. These 2D materials provided excellent interfacial protection of Li metal because of their unique properties, such as high mechanical strength, flexibility, and chemical stability. Furthermore, this coating allowed the Li-ion to penetrate through them during battery operation. These electrodes were used as the anode of the LIBs. Figure 6 compares the surface of the bare electrode (figure 6a) and an electrode coated with graphene (figure 6b) after battery cycling. As can be seen from the figure, the surface of the electrode with graphene appears flatter with fewer signs of dendritic growth compared to that of the bare electrode. Improvement in cycling performance was observed after coating the electrode with 2D materials and this improvement is mainly attributed to the dendritic suppression.

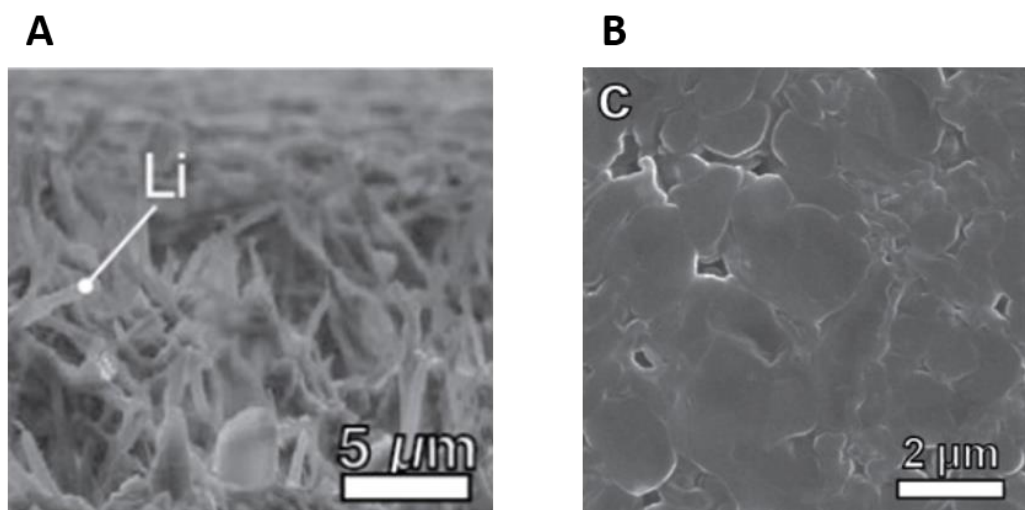


Figure 6: SEM image of Li deposition on (A) Bare Cu electrode (B) Cu electrode with graphene coating [22]

Similarly, Shin et al reported the use of nitrogen and sulfur-doped graphene layer on the separator side which faces the anode surface via a simple vacuum infiltration method [26]. These separators were used in lithium metal batteries, where the anode is lithium metal. Figure 7 compares the compares the lithium deposition after cycling on the blank and graphene-coated separator. As found in the previous study, graphene coating effectively suppresses dendritic growth.

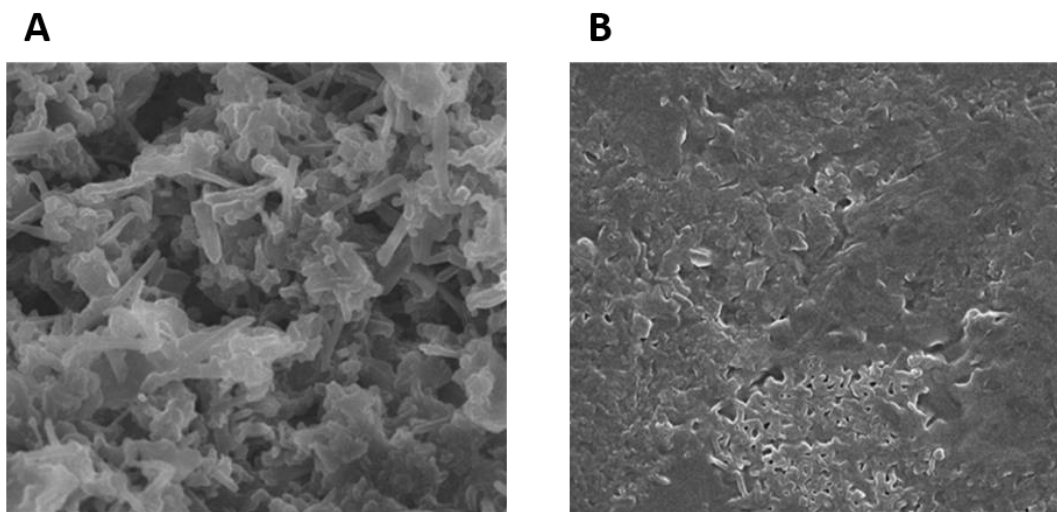


Figure 7: SEM image of Li deposition after cycling on (A) separator and (B) doped graphene coated separator after 200 cycles [26]

Foroozan et al. reported the use of a 3D conformal coating of graphene oxide onto the separator surface (facing the anode) of the Li-metal batteries to suppress dendritic growth [27]. They used the spray-coating technique to coat GO onto the separator surface. This coating allowed easy Li-ion permeation through it while preventing dendrites from passing through them. Figure 8 compares the Li deposition on Cu electrode with and without the graphene oxide coated separator after cycling. Again without graphene coating, uneven and dendritic lithium deposition is observed, while with graphene coating Li deposition is more even and uniform. Cycling performance of batteries with graphene-coated separator was better than that of the control (capacity retention of 83 % after 160 cycles as compared 80 % retention after only 80 cycles in the control sample).

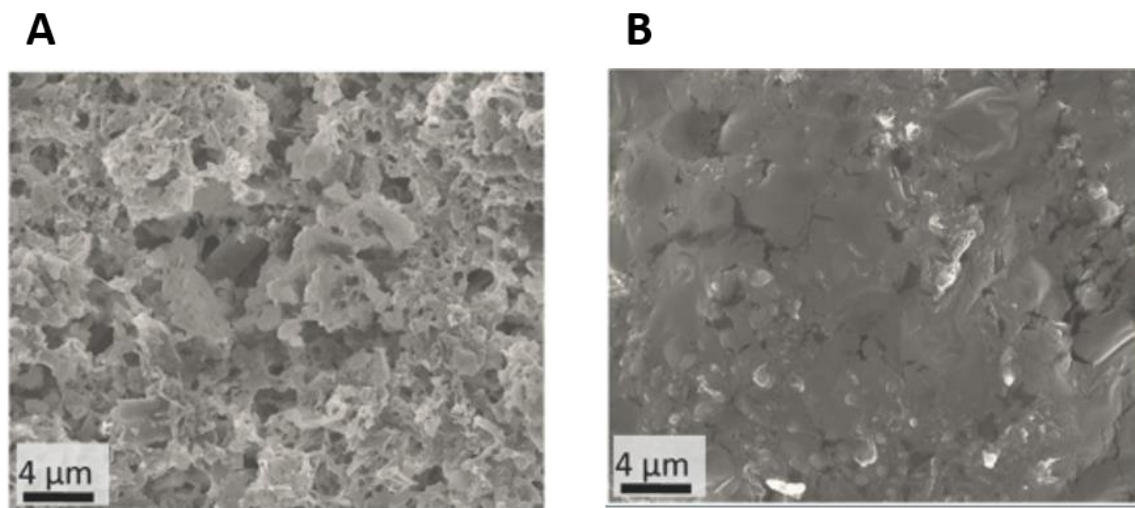


Figure 8: SEM images of Li-ion deposition on Cu anode after using (a) separator (b) GO coated separator [27]

Furthermore, the mechanism for lithium deposition on the anode in the presence of GO coating was presented in their work. In a typical anode surface, Li-ions will deposit on the pre-existing tips on the metal anode surface. This phenomenon is known as the tip effect. Tip effect leads to the nucleation and growth of lithium dendrites. However, in the presence of GO coating, during

charging Li-ions will migrate towards the anode and will first face GO barrier. GO will bind these Li-ions. Eventually, the Li-ions will travel through the GO layers because of the presence of spaces between the GO sheets and also defects within the individual GO sheets. These Li-ions will deposit on the anode surface. This process causes the Li-ion to deposit on the anode surface randomly and homogeneously, instead of deposition on the tips. This random and uniform deposition eliminates the ‘tip effect’ and leads to a more uniform Li-ion deposition. Afterward, the GO layer will act as a mechanical barrier to further suppress dendrites.

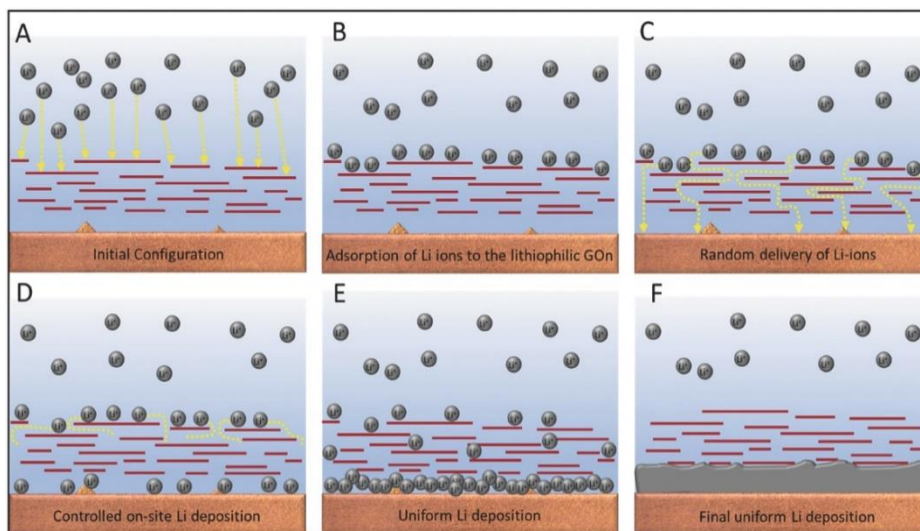


Figure 9: Schematic of Li-ion deposition in the presence of GO barrier [27]

1.3 Graphene Oxide and Reduced Graphene Oxide

1.3.1 Graphene Oxide

Carbon exists in many different allotropes, including diamond, graphite, and amorphous carbon. Graphite is a naturally occurring crystalline form of carbon. It has a planar and layered structure, where each layer consists of covalently bonded carbon. Each carbon atom bonds with three other carbon atoms. Weak van der Waals forces hold the layers together and hence these layers can easily slide over each other, which makes graphite an excellent lubricant.

Graphite oxide has a similar planar structure as graphite. However, the plane of carbon atoms contains oxygen functionalities. A single plane of graphite oxide is called graphene oxide (GO). GO is a single-atom-thick-layered material comprising of carbon, oxygen, and hydrogen [28].

Determination of the exact chemical structure of GO has been challenging. This is because, during GO synthesis, many variables are involved; each of these variables plays a critical role in GO's final chemical composition. These synthesis variables include synthesis method, oxidation medium, and graphite source. Hence GO should be considered as a family of materials and not a single composition [29]. Nonetheless, the structure of GO proposed by Anton Lerf and Jacek Klinowski is widely accepted and cited in the literature (Figure 10) [30]. In this model, the basal plane of GO contains hydroxyl and epoxide functional groups, while carboxylic and carboxylates are present on its edges.

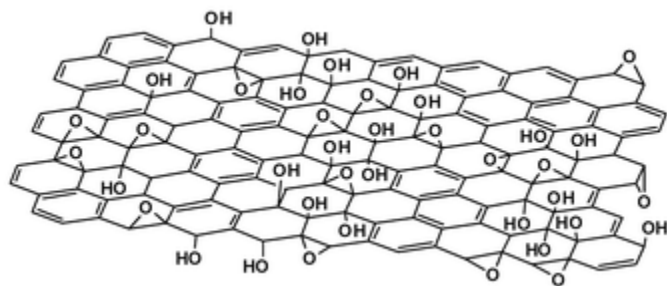


Figure 10: Chemical structure of GO-based on Lerf-Klinowski model [30]

1.3.2 Graphene Oxide fabrication

The fabrication of GO dates back to more than a century ago. In 1859, Brodie was able to synthesize GO by treating graphite with an oxidizing mixture containing potassium chlorate (KClO_3) and nitric acid (HNO_3) at $60\text{ }^\circ\text{C}$ for three to four days [31]. The mixture was then diluted in water and decanted. The solution was then dried in a water-bath, and the oxidation process

repeated until no further change in the final product was observed. He was able to determine the elemental composition of the final product, which contained mainly carbon, oxygen, and hydrogen with a molecular formula of $C_{2.19}H_{0.80}O_{1.00}$. In 1898, Staudenmaier improved Brodie's method by replacing two-thirds of fuming nitric acid with concentrated sulfuric acid and adding potassium chlorate in batches. This method made the synthesis of GO more practical in a single reaction vessel [32]. However, Brodie and Staudenmaier's method was time-consuming, hazardous and toxic due to the evolution of chlorine dioxide (ClO_2) gas.

In 1958, Hummer and reported an alternative method of synthesizing graphene oxide that mitigated these problems [33]. In this method, graphite is treated with sodium nitrate ($NaNO_3$) and sulfuric acid. Then potassium permanganate ($KMnO_4$) is added to the suspension. The temperature of the solution is brought up to $35\text{ }^\circ\text{C}$ and maintained for 30 minutes. After 30 minutes, a brownish grey paste is formed. The solution is diluted in water and treated with hydrogen peroxide (H_2O_2) to reduce residual permanganate and manganese dioxide to soluble manganese sulfate which is then removed by filtration. The solid obtained is washed in water and treated with anion and cation exchange to remove any residual salts. Dry graphene oxide is obtained by centrifuging this solution followed by dehydration. A similar degree of oxidation (C:O ~ 2:1) as Brodie and Staudenmaier's methods were obtained. Hummer's method is widely used nowadays; however, it has a major one drawback. The final product may contain contamination from permanganate ions which can be removed by hydrogen peroxide treatment followed by washing and dialysis.

In 2010, Marcano et al. reported an improvement to Hummer's method, which produces no toxic gas. Moreover, the synthesized graphene oxide has lower surface defects than the one synthesized by Hummer's method [34]. This improvement can be due to the use of phosphoric acid. In this method, graphite is added to a mixture containing a 9:1 volume ratio of sulfuric acid: phosphoric

acid (H_2PO_4). Potassium permanganate is then added to this mixture to aid in the oxidation of graphite. The solution is heated and stirred. After hydrogen peroxide treatment the solution is purified via filtration, centrifugation, and washing with water, hydrochloric acid and ethanol. These purification steps are repeated, and the obtained solid is coagulated, washed, filtered, and dried.

1.3.3 Mechanism of Graphene Oxide Formation

Dimiev and Tour investigated the mechanism behind the formation of graphene oxide from graphite during Hummer's method [35]. In their investigation, the authors identified three distinct steps in GO formation. First, when graphite is mixed with the acidic oxidizing mixture, an intermediate is formed which is called 'sulfuric acid-graphite intercalation compound' (H_2SO_4 -GIC). In this compound, sulfuric acid molecules and ions (HSO_4^-) enters and expands the gaps present between the layers of graphite. This compound is characterized by deep-blue color and forms within 3-5 minutes after exposure of graphite to acidic oxidizing medium.

In the second step, GIC is converted to pristine graphite oxide (PGO), which is the oxidized form of graphite. During this step, there is no rearrangement of graphitic layers. Also, this conversion of GIC to PGO starts at the edges of the graphite source, and the reaction continues to the center. The color of graphite flakes turns from deep-blue to brown during this step. During this step, the oxidant species tries to diffuse between the interlayer galleries of GIC. It diffuses by replacing the existing intercalated species. Once it diffuses, it oxidizes the graphene layers. The diffusion of oxidant species is slower than the oxidation chemical reaction itself, and hence this process is diffusion-limited. Also, this step is rate-determining step of GO formation. Moreover, different graphite flakes in the solution oxidized at different rates. This is due to different sizes and morphologies of these flakes which allow for different diffusion rates for oxidation species.

Smaller flakes oxidized at a faster rate compared to bigger flakes because oxidation species have to diffuse through a relatively smaller distance. Likewise, a more crystalline flake will allow oxidant species to diffuse faster and hence oxidize at a faster rate compared to a lesser ordered flake. After oxidizing agent gets reduced, it remains between the PGO interlayers until the beginning of the third step.

The third step involves the formation of GO from PGO when individual GO layers exfoliate from PGO structure after water exposure. After PGO is exposed to water, water incorporates into the GO structure and chemically transforms it through different chemical reactions. Figure 11 summarizes the process involved in the conversion of graphite to GO.

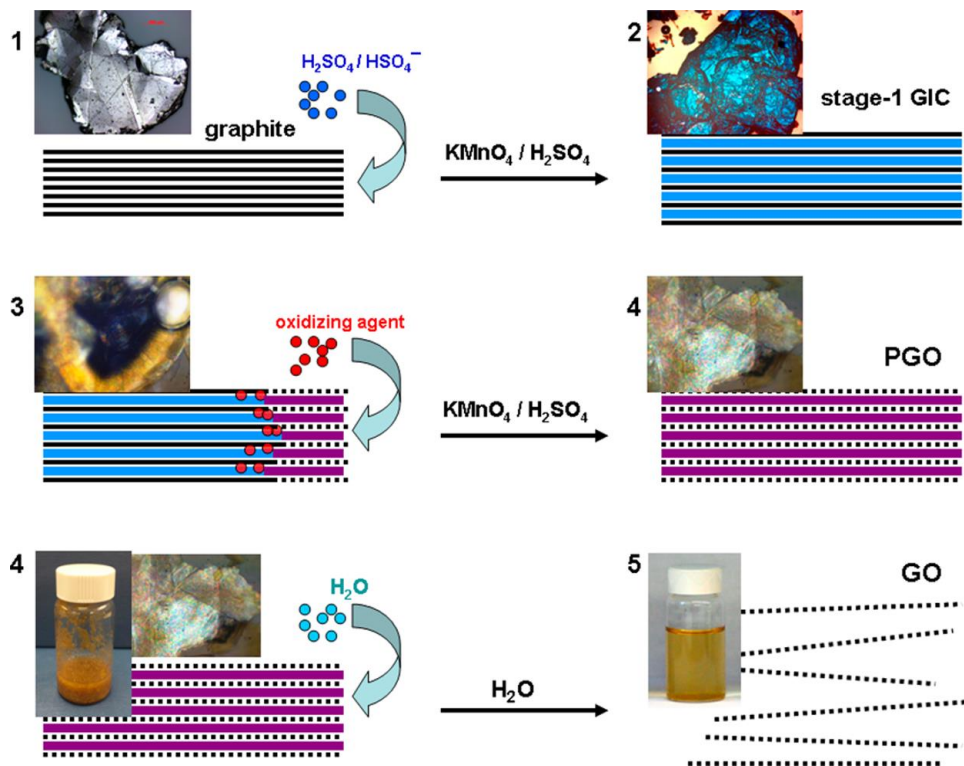


Figure 11: Schematics of mechanisms involved in the conversion of graphite to GO [35]

1.3.4 Reduced Graphene Oxide

The reduced form of GO is known as reduced graphene oxide (RGO). Several methods have been developed by the researchers to convert GO into RGO. These include treating GO with hydrazine, exposing GO to hydrogen plasma or pulse of light, heating GO in distilled water and linear sweep voltammetry. RGO can be formed by thermally reducing GO, and this process is highly desirable because of its low cost, simplicity, reliability, scalability and high yield [28].

RGO has a lower carbon to oxygen ratio than GO; the exact composition depends on its synthesis route. Its chemical composition can range from carbon to oxygen ratio of around 12:1 in most cases [36], [37]. In this work, GO was reduced to RGO by thermally reducing it with water vapor. Reduction of GO via deionized water has been reported with carbon to oxygen ratio of around 6:1 [38]. The proposed chemical structure of RGO, obtained from reducing GO, is shown in Figure 12. Oxygen-containing functional groups, including epoxy and hydroxyl groups, located within a GO sheet have lower binding energy compared to ones located on the edge of the GO sheet and hence are more accessible to remove during reduction process [39]. Therefore, some oxygen-containing functional groups are left on the edges of the GO sheet. Furthermore, there are some point and line defects on the RGO sheets from the residual oxygen-containing defects [40].

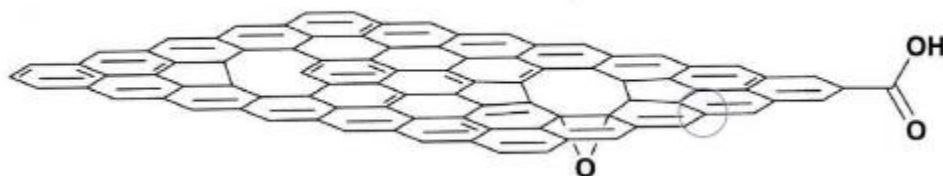


Figure 12: Proposed chemical structure of RGO [41]

1.4 Reduced Graphene Oxide as Artificial Solid Electrolyte Interphase

In this work, RGO was introduced as an artificial SEI in the aqueous batteries to prevent the anode oxidation and dendritic growth during cycling. Generally, an SEI does not form naturally in the aqueous batteries, because the decomposition products formed during its battery cycling do not deposit as a solid state on the electrode surface [42]. Hence an SEI has to be artificially introduced in the aqueous batteries.

The desired characteristics of an SEI include high electronic resistance, high mechanical strength, high ionic permeation, sub-micron thickness, chemical stability and high tolerance to expansion and compression stresses [43]. An SEI with high mechanical strength is better able to prevent dendrites from piercing through it and making contact with the cathode. Moreover, an ideal SEI should not impede the flow of ions between the electrolyte and anode surface as such impedance affects the rate of redox reactions on the anode surface required for battery operations. Also, a desirable SEI property is chemical stability since any side-reactions can decrease the coulombic efficiency of the batteries. Two-dimensional materials that match the mentioned SEI characteristics are ideal for this application since they have low thickness. Graphene was chosen as the ideal candidate for an artificial SEI because its characteristics meet or exceed these characteristics.

Electronic conductivity of graphene is highly anisotropic. Even though graphene has high electron conductivity along the graphene basal plane due to the alignment of carbon pi orbitals, which create pathways for electronic transport, it has very low electronic conductivity in the direction perpendicular to graphene basal plane [44]. Moreover, the electronic conductivity of the RGO is about three orders of magnitude less than that of the graphene because of the presence of point and line defects on the basal plane of the RGO [45]. Hence for this application, where the RGO sheets

are coated such that they are parallel to anode surface, RGO exhibits high electronic resistance as required for a good SEI. Furthermore, Young's modulus of graphene monolayer is reported to be 200 GPa, which is two times higher than that of zinc [46]. This high mechanical strength of graphene layers ensures that zinc dendrites do not pierce through it. From our nano-indentation measurement using AFM, a thick GO coating has Young's modulus of 4-5 GPa (see Appendix A). Additionally, it has been reported that micron-thick GO coating allows atoms with hydrated radii of greater than 4.5 Å to permeate through itself [47]. The hydrated radius of zinc ions is around 4.3 Å [48]. Hence, RGO coating does not impede the ionic transfer of hydrated zinc ions to and from the zinc anode surface during battery operations. Furthermore, the RGO layer is chemically stable and hence does not affect the coulombic efficiency of the aqueous batteries during cycling. Also, the thickness of the RGO layer used in this work ranges from 1 – 10 nm and hence is the ideal thickness for an SEI.

1.5 Project Scope and Objectives

Overall, the work in this thesis is based on two main objectives:

- 1) The fabrication of the porous zinc anode: Planar zinc anodes (or zinc foil) have been extensively used as the anodes for ReHAB systems. A planar zinc anode does not provide a good adhesion with the RGO layer, and hence an RGO-based artificial SEI for the anode cannot be used. Thus, the porous zinc anode is implemented in the ReHAB battery system for this purpose. Chapter 3 deals with the optimization of the porous zinc anode and its implementation in the ReHAB battery system. Furthermore, the porous anode is characterized and compared with the planar anode using various material- and electrochemical-characterization techniques.
- 2) The application of RGO as an artificial SEI on the porous zinc anode: RGO-based artificial SEI on the porous zinc anode of the ReHAB battery system was implemented. Chapter 4 deals

with the implementation of RGO as an artificial SEI in ReHAB systems, its effect on battery performance, and a study of possible reasons behind ReHAB's improved performance when artificial SEI is implemented.

Chapter 2: Material and Electrochemical Characterization Techniques

2.1 Material Characterization Techniques

2.1.1 Scanning Electron Microscope

Scanning electron microscopy (SEM) is a useful characterization technique to analyze the surface structure, morphology, phase information and the chemical composition of the samples. In SEM, the sample is irradiated with an electron beam. The SEM consists of the electron gun, the electron optics, the raster generator, and a set of detectors (Figure 13). All of the SEM components work in tandem to create an image. The position of the electron beam is scanned on the object by varying the current through the raster scanners. For each scanned point, the intensity of the electrons is detected by the detector, and this intensity is converted into an optical intensity, which is viewed on the computer screen.

Three different characterizations can be performed on an SEM instrument; namely secondary electron image, back-scattered electron image, and energy dispersive x-ray (EDX). Secondary electron image is most useful for studying surface topography. When the incident electron beam strikes the surface sample, it can collide with the sample atom's electron. This collision can impart high kinetic energy to the sample atom's electrons so that they can free themselves from the orbital into free space. These electrons have limited kinetic energy and hence are released only from the sample's surface. Backscattered electron image gives an image with an elemental contrast. When incident electron beam passes close to the sample atom's nucleus, it is attracted by the positive nuclear charge. This attraction causes the incident electron beam to deviate from its path and some of them can be redirected towards the sample surface. These backscattered electrons are detected by the detector. Atoms with the higher nuclear charge will increase the number of backscattered electrons and hence will appear brighter on screen than the atoms with lower nuclear charge.

Hence, an image with an elemental contrast is created. X-rays are created when the incident electron beam knocks off a core electron from the sample's atom. The electrons on the outer shells fill up this vacancy by demoting to the lowest electron configuration and in the process, releases energy in the form of photons. The energy of these photons depends on the bandgap of the element present. The detector detects the energy and frequency of photons and can identify the elemental composition of the sample [49]. This information about the photon is used by EDX to identify the elements and their respective atomic (or weight) percents present in the sample.

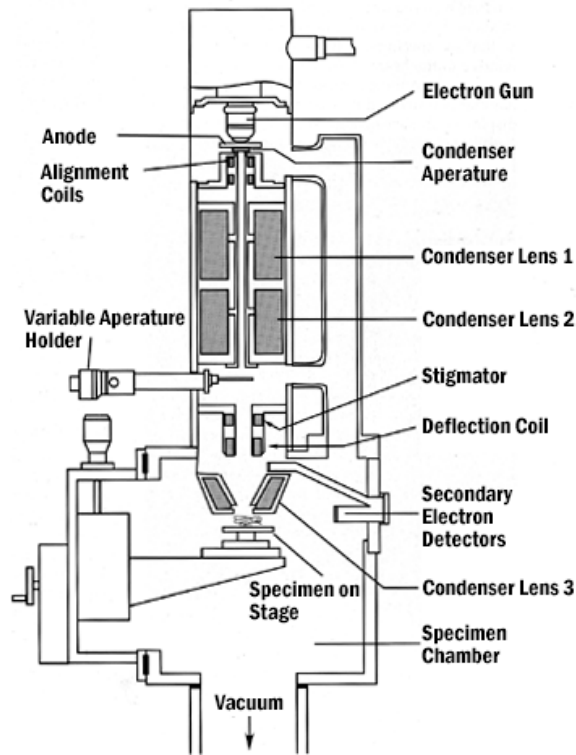


Figure 13: Schematic of SEM instrument, including electron gun, column of lenses, sample chamber and detectors [50]

In this work, SEM was used to study the surface morphology of various samples, including planar and porous zinc anode and RGO coatings on the porous anode. It was mostly used in secondary electron mode, and EDX was used to confirm the elemental composition whenever needed. A

Zeiss Leo FESEM 1530, with an accelerating voltage of 5 kV was used for all SEM characterizations.

2.1.2 Atomic Force Microscope

Atomic force microscopy (AFM) allows the characterization of the sample surface with extreme resolution and accuracy. Unlike SEM, where the electron beam is focused on the sample to image, AFM physically contacts the sample's surface to build a map of the sample's height at each point. AFM consists of a cantilever with a sharp tip mounted on it, a laser beam source and a photodetector. The cantilever has a mirror-like surface that reflects laser light from the laser source onto the photodetector. AFM images by scanning the tip over the sample surface and as the cantilever move up or down along the contours of the sample surface, a laser beam reflecting from the cantilever surface gets deflected up and down as well. This deflection in laser gets detected by the photodetector. Feedback from the photodetector enables the tip to maintain either a constant height or constant force over the sample surface. The basic operation of AFM is illustrated in Figure 14. In constant force, the height deviation of the tip as it scans the sample is recorded. In constant height, the force experienced by the tip as it scans the sample is recorded [51].

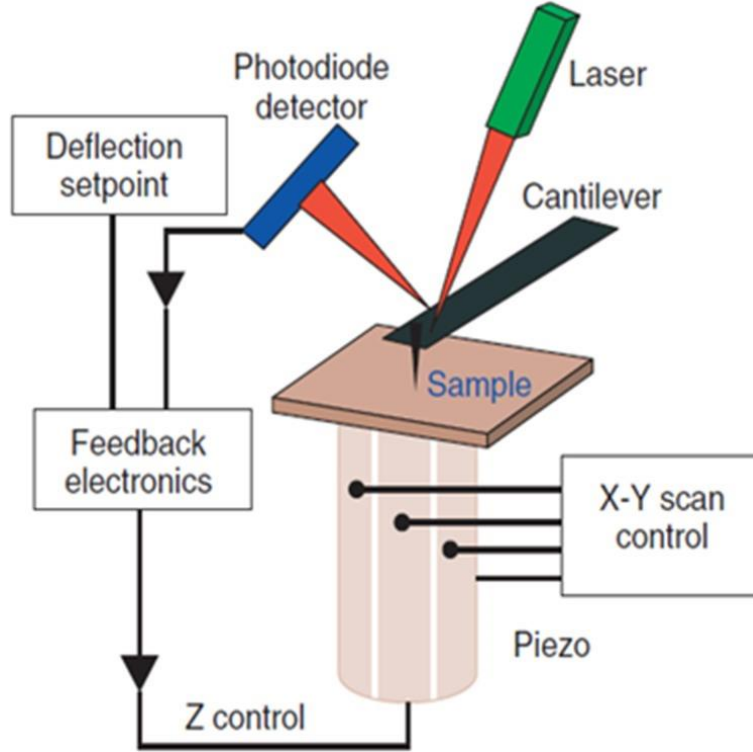


Figure 14: Basic operation of AFM [52]

Moreover, AFM can be used to characterize the sample surface including height parameters quantitatively. One of the most widely used height parameters for comparing sample surfaces are average roughness (R_a), and root mean square roughness (R_q). R_a is measured by taking the arithmetic mean of the absolute values of the height at each measurable point of the sample surface. R_q is measured by taking the mean of the square of the absolute values of the roughness profile [53]. R_a and R_q are expressed in the following equations:

$$R_a = \frac{1}{L * W} \sum_{x=1}^L \sum_{y=1}^W (z(x, y) - \bar{z}(L, W)) \quad (4)$$

$$R_q = \sqrt{\frac{1}{L * W} \sum_{x=1}^L \sum_{y=1}^W (z(x, y) - \bar{z}(L, W))^2} \quad (5)$$

Where $z(x,y)$ is the absolute height of the sample at a position (x,y) , L and W are the length and width, respectively, of the area over which the roughness is measured and $\bar{z}(L,W)$ is the arithmetic mean of the surface height [54].

In this work, AFM was used to obtain images of various samples based on their height profile. The images of planar and porous zinc anodes were analyzed for sample surface area and roughness. Moreover, nano-indentation in AFM was used to characterize the strength of graphene coatings on glass fiber substrate. AFM was also used to image RGO coating on the porous zinc anode. The AFM imaging was carried out on Bruker Dimension Icon machine using antimony (n) doped silicon tip.

2.1.3 X-ray Diffraction and Grazing Incidence X-ray Diffraction

X-ray diffraction (XRD), a non-destructive characterization technique, is used for structural and phase compositional studies. X-ray diffractometers consist of the X-ray tube, sample holder, and an X-ray detector. X-ray tube generates x-rays, which are then collimated and directed to the sample on the sample holder (Figure 15A). The intensity of the reflected x-rays from the sample is detected by x-ray detected. The sample and detector rotate, and the reflected x-ray intensity is recorded after every set rotation.

When the incident x-ray strikes the sample surface, the x-ray can get reflected, scattered or absorbed by the sample. Bragg's law governs the scattering of x-rays from the crystal lattice. Crystal planes can be assumed to be a set of parallel lines that are separated by a distance d , as illustrated in Figure 15B. The scattered X-ray from each successive planes will have different travel distance and when they meet at the detector, they will interfere with each other. At a specific

angle θ , as calculated from Bragg's law these scattered x-rays will interfere constructively, which will appear as high-intensity beam at the detector called the diffracted beam. The equation governing the Bragg's law can be expressed as:

$$n \lambda = 2 d \sin \theta \quad (6)$$

Where n is the integer, λ is the incident wavelength, d is the distance between the planes and θ is the angle at which the diffracted beam is observed. Furthermore, once the distance between crystal planes is known, the Miller index of that particular crystal plane (for cubic structures) can be determined using the equation:

$$d = \frac{a}{\sqrt{h^2 + k^2 + l^2}} \quad (7)$$

Where a is the unit cell length and h , k , and l are the Miller indices associated with that particular crystal plane.

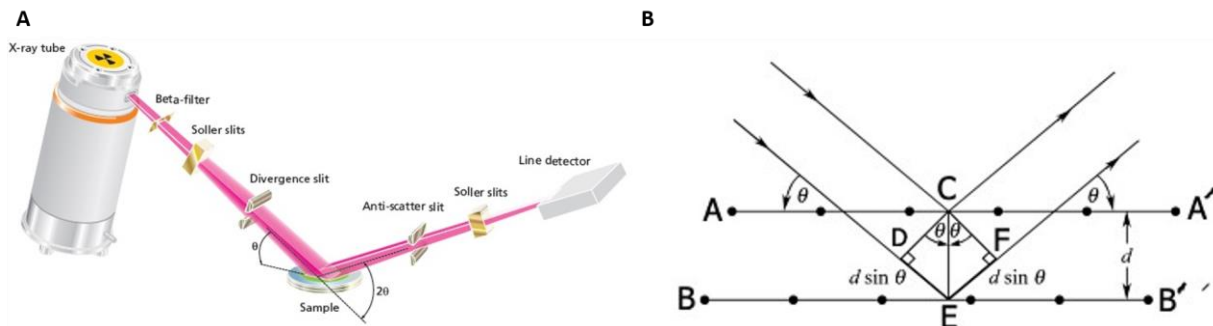


Figure 15: (A) Schematic of XRD instrument [55] (B) illustration of Bragg's diffraction, each horizontal line represents a crystal plane [56]

However, the X-ray diffraction signal from XRD is highly penetrating and hence not very useful for analyzing thin films (or sample surface), with a thickness in nm range [57]. Grazing incidence X-ray diffraction (GIXRD) is a technique used to acquire sample surface information and has been

widely used for the study of thin films. As opposed to XRD, the incidence x-ray beam is fixed at a low incidence angle. The difference between using high and low incidence angle is illustrated in the figure below. When a high incidence angle is used (Figure 16A), a significant portion of incident x-ray is absorbed by the substrate, and hence the diffracted beam will contain substrate information. However, when low incidence is used, the incident x-ray is directed more towards the sample surface, and the diffracted information from the diffracted x-ray will be more surface sensitive [58].

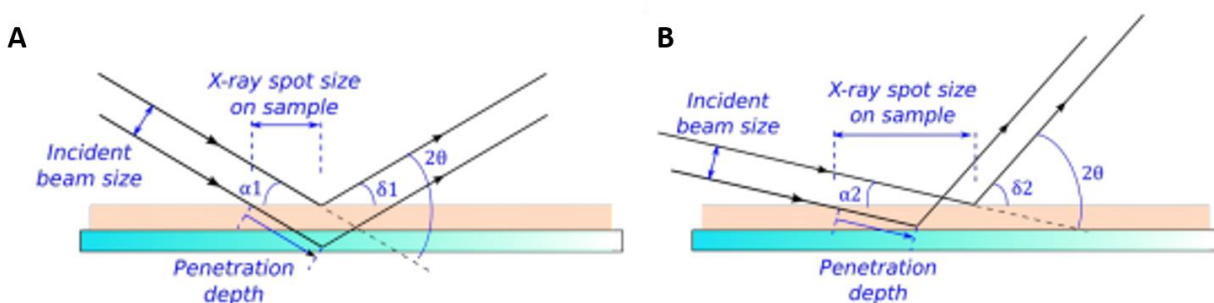


Figure 16: Illustration of x-ray diffraction conducted at (A) high and (B) low incidence angle [58]

In this work, XRD was used to determine the zinc crystal growth direction before and after chronoamperometry of planar and porous zinc anodes. Bruker D8 Discover X-ray diffractometer with Cu x-ray tube and a wavelength of 1.54 Å was used to carry all XRD experimentation in this work. GIXRD was used to study zinc crystal growth on the surface of RGO coated porous zinc anodes before and after 1 hour of chronoamperometry. PANalytical X'Pert Pro MRD diffractometer with Cu K α radiation of 1.54 Å and the incidence angle of 0.3° was used for GIXRD characterizations.

2.1.4 X-ray Photoelectron Spectroscopy

X-ray photoelectron spectroscopy (XPS) is a non-destructive surface characterization technique which provides elemental and chemical state information. The XPS instrument consists of the x-ray source, monochromator, and photoelectron detectors (Figure 17A). The analysis is carried out in ultra-high vacuum. When the incident x-ray strikes electron of the surface atom, the electron gains energy. This energy can be sufficient for the electron to overcome the binding energy of the nucleus and remaining energy is converted to kinetic energy (Figure 17B). The velocity of these moving electrons is detected by the detector. The binding energy experienced by the electron is given by:

$$E_k = h\nu - E_B - \phi \quad (8)$$

Where E_k is the kinetic energy of the electron, h is the Planck's constant, ν is the frequency of the incident x-ray, E_B is the binding energy experienced by the electron and ϕ is the energy cost for the electron to leave the sample surface and reach the detector.

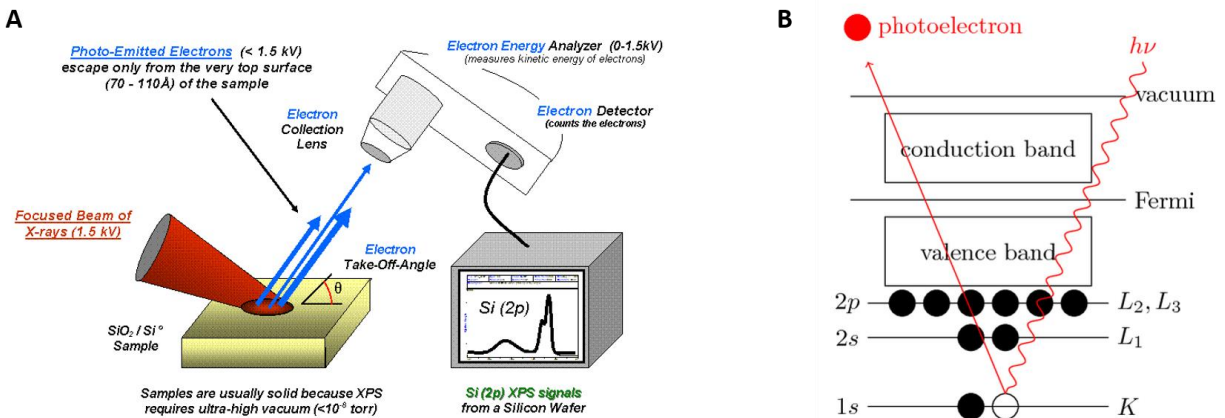


Figure 17: (A) Schematic of XPS instrument (B) principle of the emission of photoelectron [59]

Monochromatic x-rays incident on the sample can generate photoelectrons from different atomic levels, and hence photoelectrons of different velocities are detected. Elements and their chemical environment (e.g., chemical bonds) can be identified from the velocities of ejected photoelectrons.

In this work, XPS was used to find the extent of oxidation of the anode before and after chronoamperometry and battery testing. A Thermo-VG Scientific ESCALab 250 microprobe was used to record XPS spectra. The spectra were taken using a monochromatic aluminum source, at 1486.6 eV and 49.3 W, with a beam diameter of 200.0 μm . The samples were pressed on a piece of conductive carbon tape, and a double neutralization - a low energy electron beam and low energy Ar^+ beam - were used during spectrum acquisition. The binding energies were reported relative to C1s at 284.8 eV. The chamber analysis pressure was 2.0×10^{-9} Pa during acquisition. The take-off angle was 45 °C. For each sample, a high sensitivity mode spectrum was taken with a wide binding energy range of 0 to 1350 eV (survey) to determine the surface elemental composition of the samples. Then, a narrower binding energy window, with a pass energy of 23.50 eV, was used to get high energy resolution spectra of the elements present in the sample to determine its chemical environment and quantification.

2.1.5 Raman Spectroscopy

Raman is a non-destructive characterization technique primarily used for the identification of chemical species present in the sample. Modern Raman spectrophotometers consist of a laser light source, monochromators and Raman detectors (Figure 18A). In Raman spectroscopy, the monochromatic laser beam is illuminated on the sample surface. When the photon collides with the sample atom, two types of scattering are observed: elastic or Rayleigh scattering and inelastic or Raman scattering (Figure 18B). Majority of incident photons experience elastic scattering and will be filtered out by the spectrometer because these scatterings provide little or no useful

information about the sample. If the polarizability of the sample molecule varies with its orientation, Raman scattering is observed. Raman spectra for rotational and vibrational states can also be collected [60].

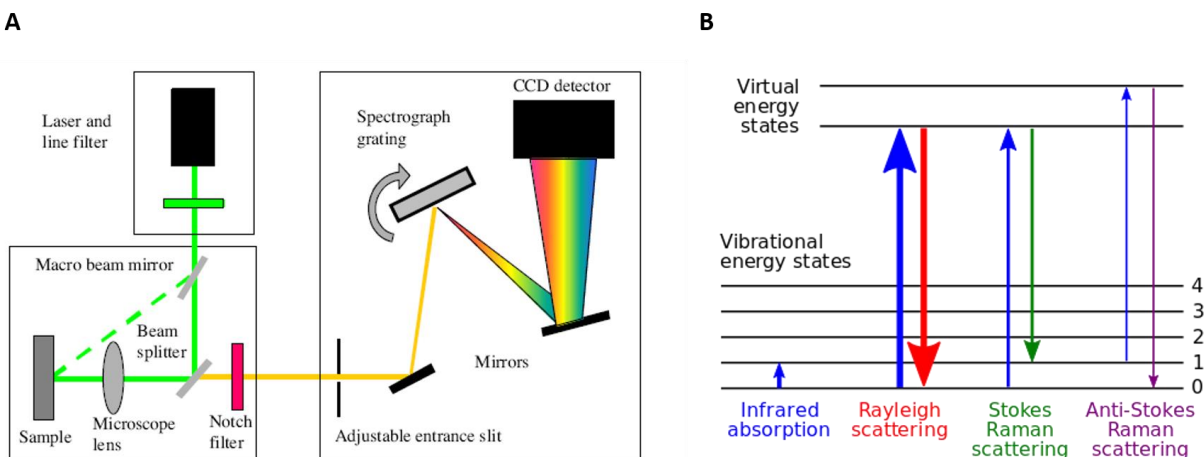


Figure 18: (A) Schematic of Raman instrument, and (B) vibrational energy levels [61]

In this work, Raman spectra for RGO coated anodes before and after 1 hour of chronoamperometry was collected. Raman spectra of graphene oxide and reduced graphene oxide synthesized from improved Hummer’s method exhibits G (at around 1560 cm^{-1}) and D (at around 1360 cm^{-1}) bands. The G band arises from the stretching of all pairs of sp^2 atoms in both the ring and chains. The D peak originates from the breathing modes of sp^2 atoms in rings [62]. All Raman characterizations were carried out by a Bruker Senterra Raman microscope with laser radiation of 785 nm, an integration of 20 seconds, an objective of x10 and a laser power of 20 mW.

2.1.6 Contact Angle Measurement

Contact angle measurements are widely used to measure the surface wettability in physics and chemistry. The commonly used apparatus for contact angle measurement is illustrated in Figure 19. The contact angle (θ) is defined as the angle formed by the liquid where the solid, liquid and

vapor intersect. The sample surface is said to be hydrophilic if the contact angle formed by water is less than 90° . The sample surface is hydrophobic if the contact angle formed by water is more than 90° . Basic instrument for static contact angle measurement includes a stationary platform for holding the sample, liquid droplet dispensing system, light source, and camera.

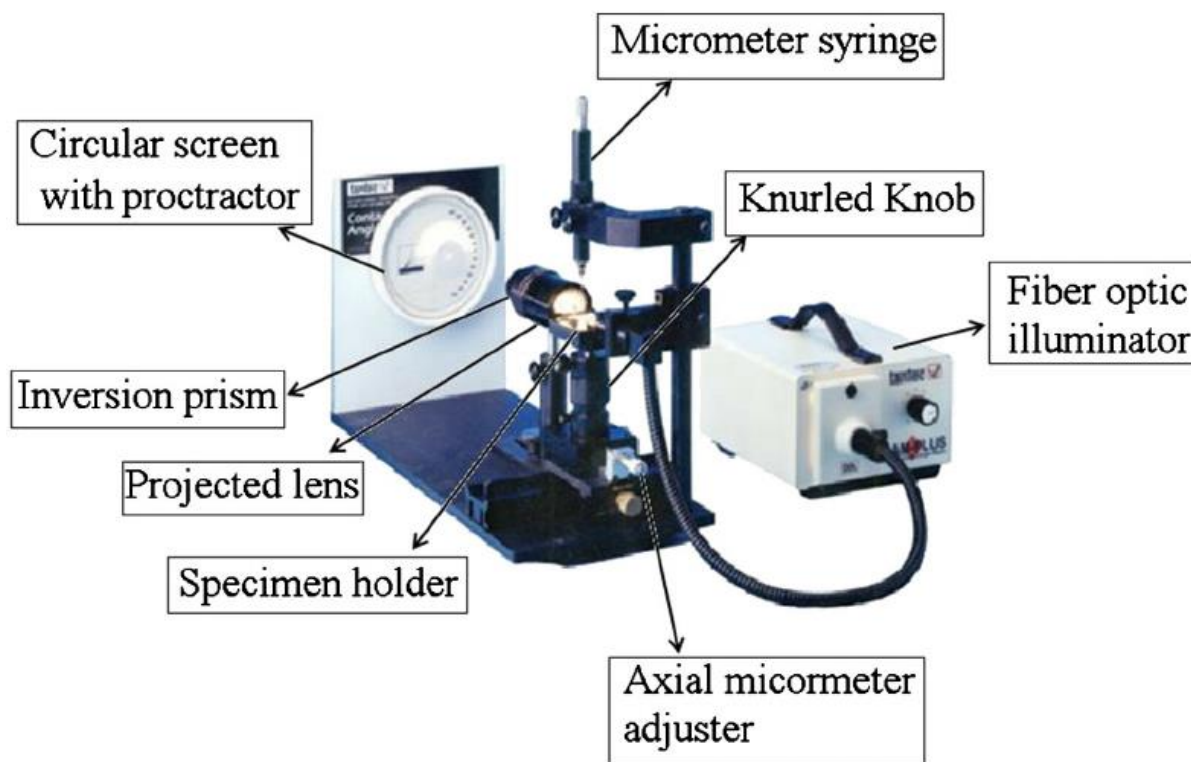


Figure 19: Apparatus for measuring the contact angle

In this work contact angle measurements was used to determine the wettability of planar and porous zinc anodes and as one of the techniques of proving RGO coating on the anode surface.

2.2 Electrochemical Characterization Techniques

2.2.1 Tafel Characterizations

Tafel extrapolation on the linear polarization curve can be used to measure, and compare corrosion rates. A typical experiment is conducted in a three-electrode setup. These electrodes include the

reference, working and counter electrodes. The sample being investigated is used as the working electrode. These electrodes are connected to a potentiostat. The potential at which the reference electrode is reduced is known, and hence, the reference electrode is used to measure and control the potential of the working electrode. The potential is varied in set potential intervals, and the resulting current is measured. The log of current is plotted against the potential. Extrapolation of cathodic and anodic Tafel slopes corresponds to the corrosion potential (E_{corr}), and corrosion current (i_{corr}), as shown in Figure 20 [63].

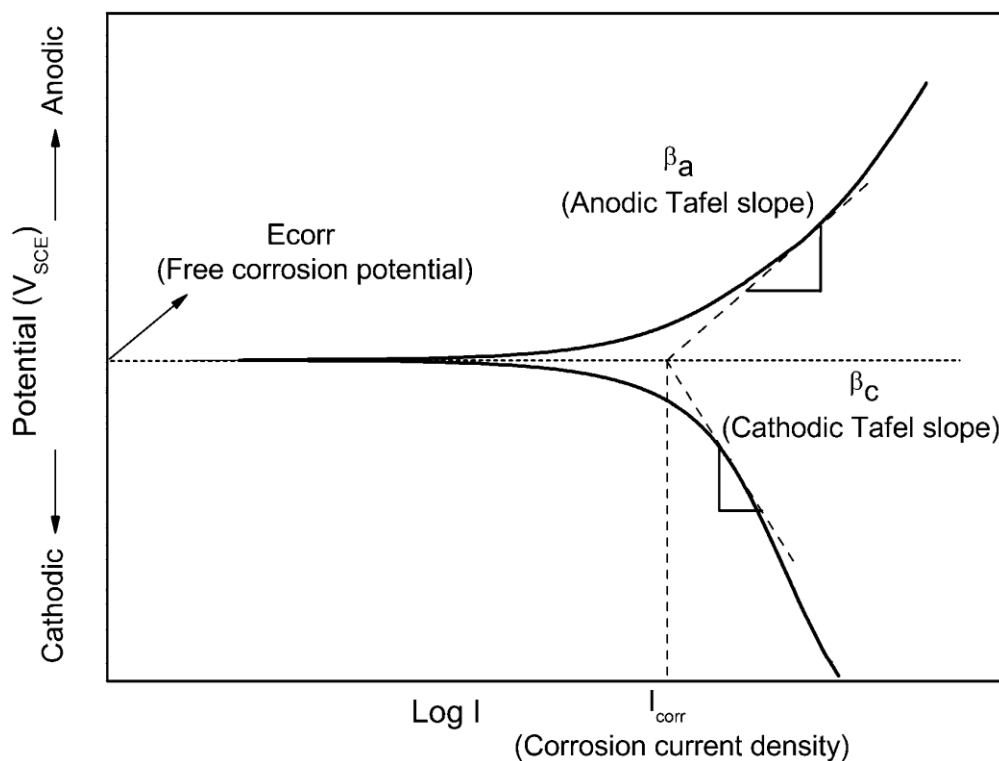


Figure 20: Illustration of Tafel extrapolation on linear polarization curve. The intersection of anodic and cathodic Tafel slope gives corrosion potential and corrosion current density [64]

In this work, Tafel plot was used to compare the corrosion rates of anodes when exposed to the electrolyte. Polished zinc foil and Ag/AgCl were used as a counter and a reference electrode, respectively. An aqueous electrolyte, adjusted to pH 4, containing 1 M of Li_2SO_4 and 2 M of

ZnSO₄ was used. CHI760D was used as the potentiostat, and the potential was scanned from -1.8 V to -2.1 V with a step interval of 0.01 V.

2.2.2 Chronoamperometry

Chronoamperometry (CA) technique can be used to study electrodeposition behavior of ions on an electrode surface. In a typical chronoamperometric setup, three-electrode system is used (see section 2.2.1). The potential between the working and counter electrode is controlled by the potentiostat to maintain the potential difference between the working and reference electrodes. An example of an applied potential waveform is shown in Figure 21A. The initial potential difference (E_1) is smaller than the reduction potential of the ions present near the surface of the electrode, and hence these ions will not be reduced. Once a more negative potential is applied (E_2), such that the reduction of ions can happen rapidly, the surface concentration of these ions on the electrode surface reaches almost zero. This event creates a concentration gradient of the ions between the electrode surface (ionic concentration of almost zero) and the bulk electrolyte (very high ionic concentration). Therefore, more ions flow from the bulk electrolyte to the electrode surface. Subsequently, these ions on the electrode surface get reduced, and current flows into the working electrode. This current in the working electrode is recorded (a large current drop is registered in the current-time profile in Figure 21C). With time, the continued flux of ions causes the depletion region around the electrode to thicken, resulting in the decline of the concentration profile's slope (Figure 21B). This decreases the increase of current and the current eventually stabilizes (current eventually stabilizes in current-time profile in Figure 21C) [65].

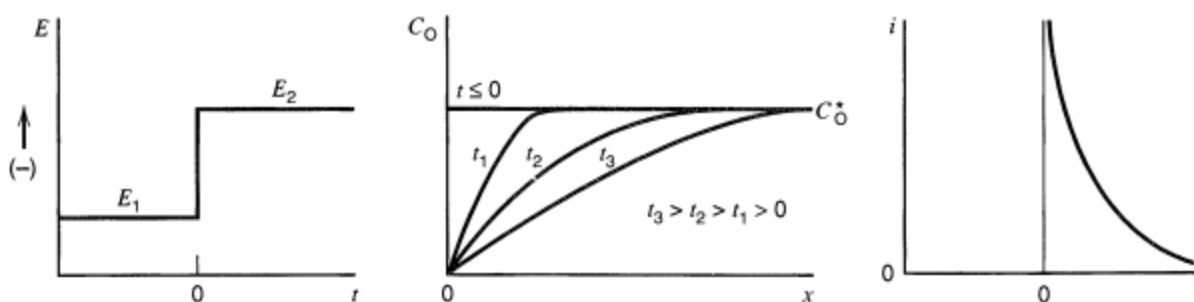


Figure 21: (A) Waveform where chemical species under investigation is inactive at E_1 but is reduced at E_2 , (B) concentration profiles at different times, and (C) current-time profile [65]

In this work, chronoamperometry was used as a test to characterize the evolution of dendrites in the anode surface. Polished zinc foil and Ag/AgCl were used as a counter and a reference electrode, respectively. An aqueous electrolyte, adjusted to pH 4, containing 1 M of Li_2SO_4 and 2 M of ZnSO_4 was used. Bio-Logic VMP3 potentiostat was used, and the current was recorded after every 0.1 seconds.

2.2.3 Electrochemical Impedance Spectroscopy

Electrochemical impedance spectroscopy (EIS) is a powerful electrochemical characterization technique to study the kinetics occurring at the electrodes. This technique is conducted typically in a three-electrode system (See section 2.2.1). When an electron is transferred across the electrode-electrolyte interface, this transfer is due to faradaic and non-faradaic components. The faradaic component involves polarization resistance (R_p) and solution resistance (R_s), while non-faradaic component involves double-layer capacitor charging. These components can be modeled by an electric equivalent circuit (EEC). The EIS technique allows the measurement of activation resistance, which is also represented by charge transfer resistance (R_{ct}) at the standard electrode potential [66]. In most EIS techniques, a fixed sinusoidal alternating voltage is applied on a three-

electrode system, and the resulting current in the system is recorded. This process is repeated over a set frequency range. The frequency dependent impedance can be defined as:

$$Z(\omega) = R_s + \frac{R_p}{1 + \omega^2 R_p^2 C_d^2} - j \frac{\omega R_p^2 C_d}{1 + \omega^2 R_p^2 C_d^2} = Z'(\omega) - jZ''(\omega) \quad (9)$$

Where R_p is the polarization resistance, ω is the frequency and C_d is the capacitance of double-layer charging. Equation 9 shows that a semicircle with a diameter of R_p and intercept of R_s on the $Z'(\omega)$ axis is obtained when $Z''(\omega)$ is plotted against $Z'(\omega)$ [67].

In this work, EIS was used to measure the charge-transfer resistance of RGO coated anodes. These tests were conducted in a three-electrode system with a platinum wire and Ag/AgCl as the counter and a reference electrode, respectively. An aqueous electrolyte, adjusted to pH 4, containing 1 M of Li_2SO_4 and 2 M of ZnSO_4 was used. Bio-Logic VMP3 potentiostat was used, and the frequency was varied from 1 MHz to 100 Hz.

2.2.4 Cyclic Voltammetry

Cyclic voltammetry (CV) is an electrochemical technique used to study the oxidation and reduction potentials of molecular species. This technique is carried using two- or three-electrode system.

A potential scan is applied, and the resulting current is recorded and plotted against applied potential (Figure 22). Potential of the working electrode is measured against the reference electrode and is varied from a higher potential (V_1) to a lower potential (V_2) (Figure 22A). Current at the working electrode is measured and recorded during the potential scan (Figure 22B). During this scan, the molecular species under investigation either gets reduced (or oxidized). At V_1 , the potential is too low for any reaction to happen and hence no current is measured. As the voltage is

initially swept, reaction started to happen and current start to flow in the system. This current starts to increase as the potential keeps on increasing. This current is due to the flow of ions from the bulk electrolyte to the electrode surface. At the electrode surface, the ions get reduced (or oxidized), and at these potentials, this reaction is limited by the diffusion of the ions to the electrode surface (diffusion-controlled). However, at the reduction (or oxidation) potential, the diffusion of the ions reaches it's maximum because now the reaction is limited by the reaction's activation energy (activation-controlled). At this point, the current in the working electrode also reaches its maximum (shown by the peak (or valley) in the CV plot in Figure 22B). As the potential scan continues, the current starts to drop. This drop is because at these potentials the ions accumulate on the electrode surface and do not reduced (or oxidized) fast enough. The reverse scan occurs from the lowest potential (V_2) in the first scan to the highest potential (V_1). Again the molecular species undergoes oxidation (or reduction) [68].

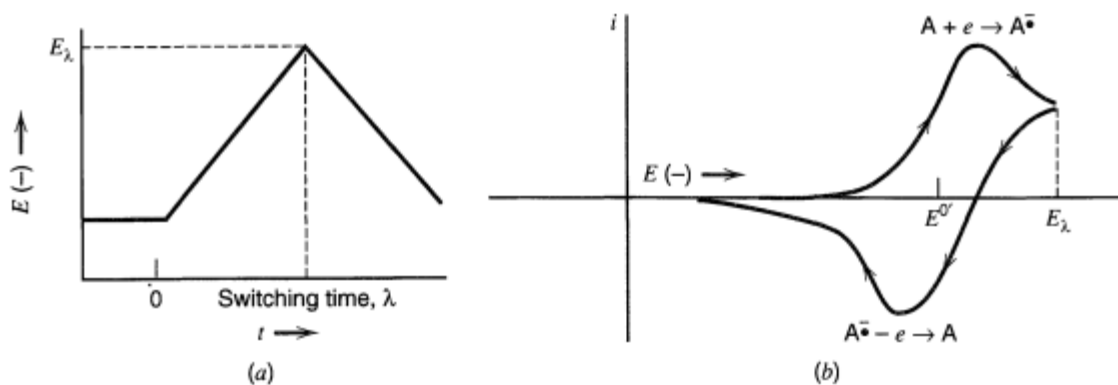


Figure 22: (A) Potential scan with time (B) Resulting CV plot [65]

In this work, CV was used to determine the oxidation, and reduction potentials of the ions in the battery, and three-electrode system. Polished zinc foil and Ag/AgCl were used as counter and a reference electrode, respectively. An aqueous electrolyte, adjusted to pH 4, containing 1 M of

Li₂SO₄ and 2 M of ZnSO₄ was used. Bio-Logic VMP3 potentiostat was used, and a scan rate of 0.1 mV s⁻¹ was used

2.2.5 Battery Testing

In this work, various anodes were implemented in ReHAB system and tested for various battery performances, including cycle life, rate performance, float charge current and capacity, and open circuit voltage (OCV). The batteries were assembled in coin cell configuration (unless stated otherwise) and were tested using Neware battery tester. All battery testing was conducted at room temperature.

Lithium manganese oxide (LMO) coated on polyethylene (PE) film substrate was used as the cathode. The LMO cathode was prepared by casting a slurry containing 86 wt. % LMO, 7 wt. % KS-6 (conductive carbon), and 7 wt. % polyvinylidene fluoride (PVDF) in N-methyl-2-pyrrolidone (NMP) solvent on the polyethylene (PE) film. This anode was vacuum dried at 60 °C for 24 hours to dry the slurry. Anodes were assembled with lithium manganese oxide as a cathode, absorbed glass mat (diameter: 1.15cm and thickness: 0.5mm) as separator and solution of 1 M Li₂SO₄ and 2 M ZnSO₄ in deionized water (pH 4) as the electrolyte.

Galvanostatic charge-discharge cycling was conducted at a current density of either 1C or 4C. In each cycling, batteries were charged to 2.1 V and then the voltage was maintained at 2.1 V for a set time (15 min or 1 hour for current densities of 1C and 4C, respectively). Then they were discharged to 1.4 V. The cycling retention after every cycle was calculated using the equation:

$$\text{Percent Retention} = \frac{\text{Capacity after } x \text{ cycles}}{\text{Capacity after 1}^{\text{st}} \text{ cycle}} * 100 \quad (10)$$

Rate capability test was performed at different C-rates. Batteries were subjected to five cycles at particular C-rate before changing the C-rate. OCV test was conducted for 72 hours. Batteries were charged to 2.1 V at 0.2C and then, they were held without any potential for 72 hours. The potential in the batteries was recorded during this time interval. Float charge capacity and the current were performed by charging the coin cells to 2.1 V at 0.2C and then maintaining a potential of 2.1 V for 24 hours. The capacity or current was monitored during this period. The capacity loss (C_{loss}) of float charge is calculated using:

$$C_{loss} = \frac{C_f}{C_{discharge}} * 100 \quad (11)$$

Where C_f and $C_{discharge}$ are the float charge capacity before and after 72 hours, respectively.

Chapter 3: Fabrication, Optimization, and Characterization of Porous Zinc Anode

3.1 Fabrication of Porous Zinc Anode

Porous zinc anode provides a greater surface area that is electrochemically active and makes more surface contact with the electrolyte. Hence, theoretically, batteries that utilize the porous anodes should deliver higher specific energy than the ones with the planar anodes. Porous zinc anodes have been used in various aqueous battery systems that use alkaline or neutral aqueous electrolytes [69][70]. However, the increased surface area of the porous anodes leads to more zinc passivation during battery charging [71]. The use of the metal oxide additives, including lead oxide (PbO) and bismuth oxide (Bi_2O_3), to prevent zinc passivation in other battery systems during cycling have been studied and reported [72] [73]. Furthermore, PbO and Bi_2O_3 additives in the porous zinc anodes have shown to suppress hydrogen formation on the anode surface, reduce zinc solubility in an aqueous electrolyte, enhance anode conductivity, and homogenize current density distribution during battery operations [74]–[76].

Gel binder was prepared by mixing 2.5 weight percent (wt. %) of hydroxyl-propyl methylcellulose (HPMC), 1.25 wt. % of poly (acrylic acid) (PAA), and 1.25 wt. % of polyvinyl alcohol (PVA) in DI water. To ensure that these polymers were thoroughly mixed in the solution, the solution was stirred in a hot plate at 135-140 °C for 72 hours. The solution appeared clear after polymers were fully dissolved. It was left to cool at room temperature for at least 24 hours before use.

A slurry containing 96 wt. % pure zinc powder, 2 wt. % binder, and 2 wt. % additives (1 wt. % PbO and 1 wt. % Bi_2O_3) was prepared. First, zinc pure powder and additives were weighed, thoroughly mixed, and ground using mortar and pestle for at least 10 minutes. Binder was weighed

and added to this mixture. The resulting mixture was thoroughly mixed for 5 minutes and then defoamed for 30 seconds using a mechanical mixer. Seven metal balls were used during the mixing and defoaming process.

The resulting slurry was coated onto a brass substrate using a doctor blade set to a thickness of around 0.25 mm. The thickness of the brass substrate used was approximately 0.23 mm. The slurry coated substrate was dried in an oven at 60 °C for 24 hours to ensure that the slurry was completely dry. The resulting anode was pressed using a roller presser to ensure that its surface was flat.

3.2 Optimization of Porous Zinc Anode

Different parameters of fabricating porous zinc anodes were tried and tested for cycling performance. These fabrication parameters include zinc powders from different sources, different binder concentrations, and different zinc powder particle sizes. The cycle life of these tried parameters under a current density of 4C is presented in Figure 23. First, anodes were fabricated with most common commercially available zinc powder types, and these fabricated anodes were tested for cycle life (Figure 23A). The weight percent of the zinc powder and binder were fixed to be 96 wt. % and 2 wt. %, respectively. Anode with the purum zinc powder displayed the highest discharge capacity for all cycles leading up to 100 cycles, and hence this powder was chosen for subsequent experiments.

Next, anodes with two different zinc and binder compositions (zinc: binder weight ratio of 96 %: 2 %, and 95.8 %: 2.2 %) were fabricated and tested (Figure 23B). A binder concentration of at least 2 wt. % was necessary for a stable anode and hence any concentration lower than 2 wt. % could not be tested. An increase in the binder concentration of 2 wt. % significantly decreased the

discharge capacity and cycling stability of the batteries. Therefore, porous anode composition of zinc: binder: additives weight ratio of 96 %: 2 %: 2 % was used for subsequent experiments.

Third, anodes with different particle sizes of purum zinc powder were fabricated and tested (Figure 23C). The purum zinc powder was ball-milled at different times to decrease its particle size. The weight percent of zinc and binder were fixed to be 96 wt. % and 2 wt. %, respectively. There was no significant improvement in capacity or cycling retention by ball-milling, and hence original zinc purum powder (i.e., without any ball milling) was used for subsequent experiments.

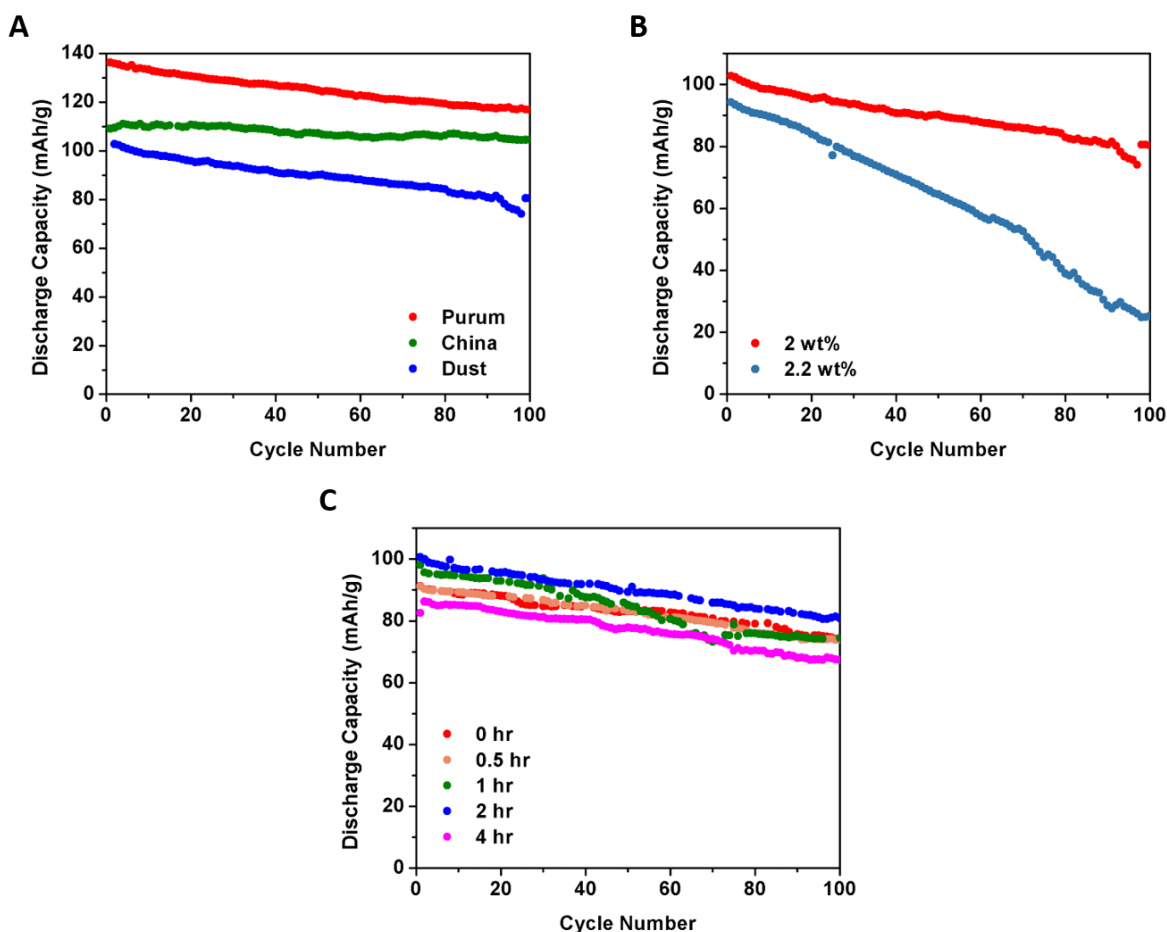


Figure 23: Cycle life of anodes consisting of (A) different zinc powder types at 1C (B) different binder concentrations at 1C (C) different purum zinc powder sizes at 4C

3.3 Characterization of Planar and Porous Zinc Anodes

3.3.1 Basic Characterizations

Scanning electron microscopy (SEM) was used to observe the surface of zinc foil and porous anodes, as shown in Figure 24. For the foil anode, a smooth flat surface is observed, with minor cracks of nano-meter dimensions (possibly from polishing of the anode during sample preparation). For the porous anode, agglomerates of zinc particles are observed along with the well-dispersed particles of lead and bismuth oxide additives. These zinc agglomerates range in size from a few microns to 20 μm .

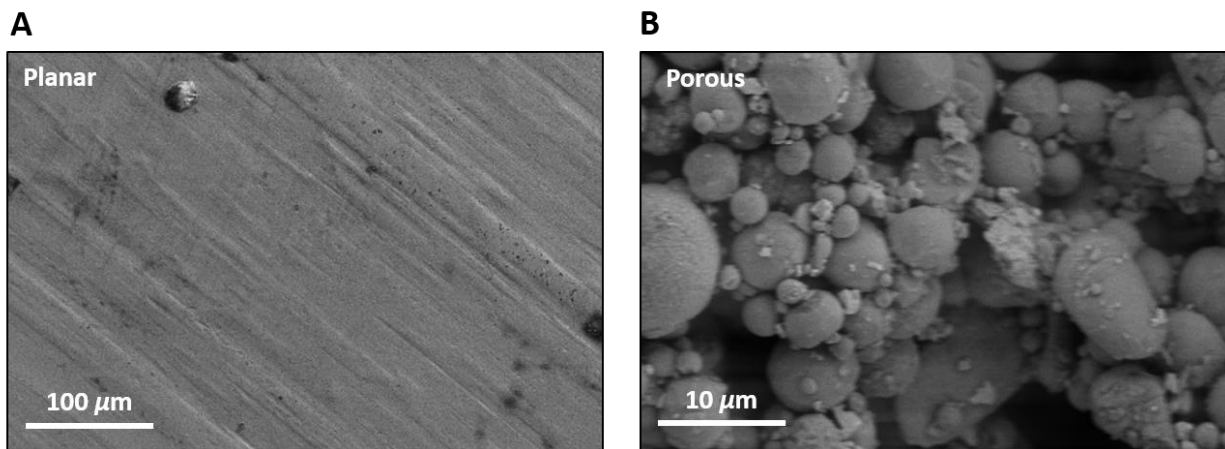


Figure 24: SEM images of (A) planar and (B) porous zinc anodes

Atomic force microscopy (AFM) was used to image and determine the height profiles of the planar and porous zinc anodes. These AFM images, with their corresponding height profile scales, are shown in Figure 25. The scan area of these images is 15 μm by 15 μm . The planar anode is relatively smooth, with its maximum surface feature extending to 240.3 nm, while that of porous anode extends to 7.6 μm . Furthermore, the zinc particle agglomerates observed in the SEM images are also observed in these AFM images.

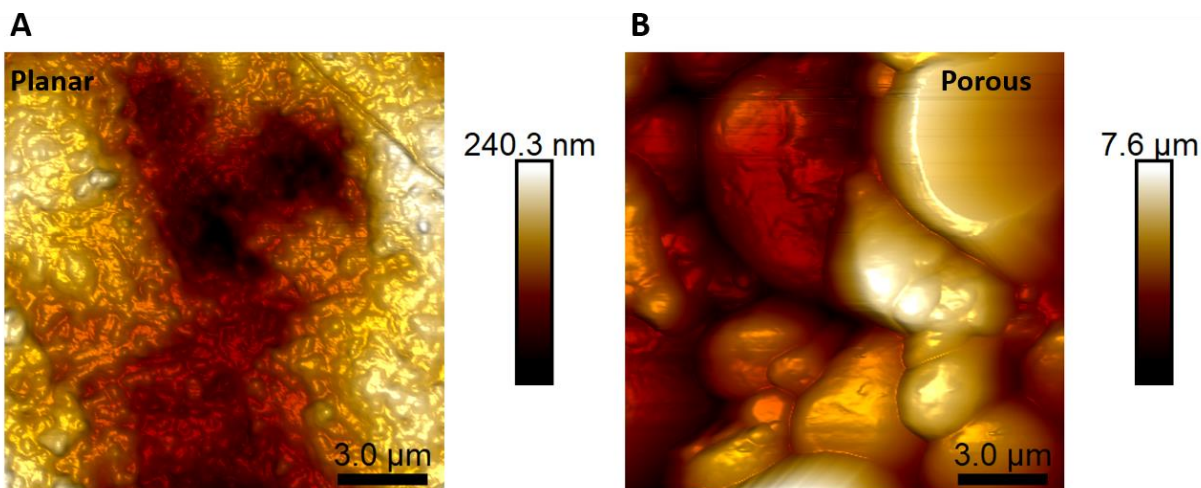


Figure 25: AFM images of (A) planar and (B) porous zinc anodes

These AFM images were used to measure the sample surface average roughness (R_a), root mean square roughness (R_q) and surface area, the results of which are tabulated below (Table 1). The image surface area was measured on the sample area of $225 \mu\text{m}^2$ (i.e. the area of the sample in x and y plane is $225 \mu\text{m}^2$). For the planar anode, the surface area was $225 \mu\text{m}^2$, which is equal to the area it was measured on, emphasizing the flatness of its sample surface. Meanwhile, the measured surface area ($400 \mu\text{m}^2$) of the porous anode is much higher than that of the planar sample. Moreover, the average and root mean square roughness of the porous anode's surface (R_a and R_q is 883 nm and 1078 nm, respectively) is significantly higher than that of the planar anode's surface (R_a and R_q are 31.3 nm and 37.6 nm respectively).

Table 1: Image surface area, average roughness (R_a) and root mean square roughness (R_q) of planar and porous zinc anodes

	Sample Name	
	Planar	Porous
Image Surface Area (μm^2)	225	400
Average Roughness, R_a (nm)	31.3	883
Root Mean Square Roughness, R_q (nm)	37.6	1078

Contact angle measurement was conducted on the planar and porous zinc anodes, the results of which are shown in Figure 26. The Porous anode surface shows higher hydrophilicity (contact angle of $65^\circ \pm 5.8^\circ$), and hence better wettability than the to planar anode surface (contact angle of $94^\circ \pm 4.3^\circ$). This hydrophilic property of the porous anode allows for a more intimate contact with aqueous electrolytes and hence is desirable for its application in aqueous batteries.

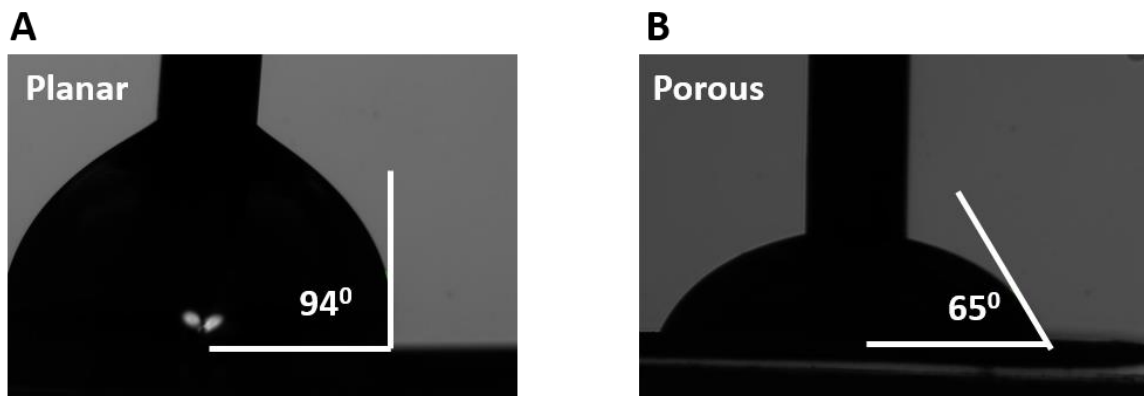


Figure 26: Contact angle measurement of (A) planar and (B) porous zinc anodes

3.3.2 Battery Performance

The anodes were assembled in a coin cell configuration and tested for cycle life. The batteries were run at a current density of 1C under CC-CV mode for time cut-off of 1 hour (i.e., each cycle consists of 1 hour of charge followed by maintaining the voltage at 2.1 V for 1 hour and followed by 1 hour of discharge). The batteries were charged from 1.4 V to 2.1 V. The discharge capacity obtained after every cycle is plotted and is presented in Figure 27. Furthermore, the discharge capacities and discharge retentions after every 100 cycles are tabulated below (Table 2).

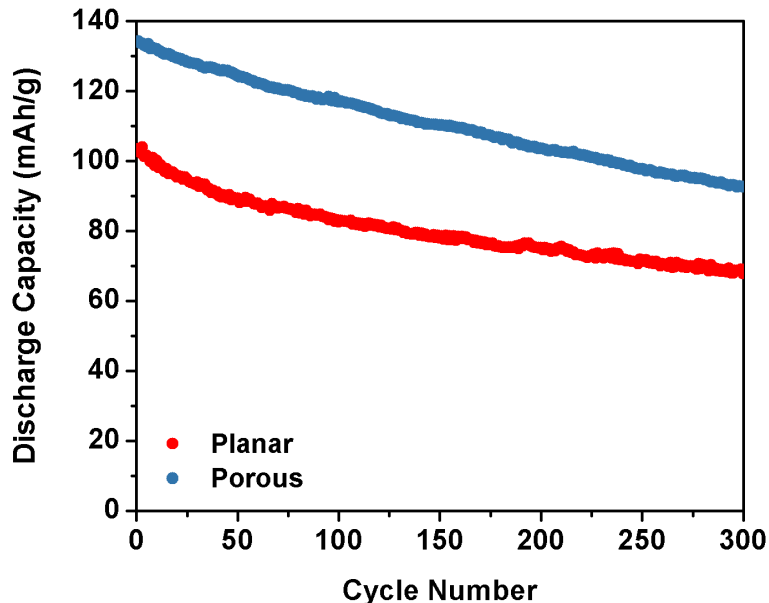


Figure 27: Cycle life of planar and porous zinc anode under a current density of 1C

Porous anode shows significantly higher discharge capacity ($136.28 \text{ mA h g}^{-1}$) than that of the planar anode ($103.42 \text{ mA h g}^{-1}$). Although the porous zinc anode showed faster decay rate in its discharge capacity, the porous anode actually has better overall performance for the duration of the test owing to its higher starting point (e.g. after 300 cycles the discharge retention of the porous anode is 69 % compared to 65 % retention of the planar anode).

Table 2: Summary of discharge capacity (mA h g⁻¹) and retention (%) of planar and porous zinc anode after every 100 cycles

	Sample Name	
	Planar	Porous
Initial Discharge Capacity (mA h g⁻¹)	103.42	136.28
Discharge Capacity after 100 cycles (mA h g⁻¹)	82.62 (80 % retention)	117.00 (87 % retention)
Discharge Capacity after 200 cycles (mA h g⁻¹)	75.28 (73 % retention)	103.67 (77 % retention)
Discharge Capacity after 300 cycles (mA h g⁻¹)	67.92 (65 % retention)	92.69 (69 % retention)

The rate performance of the planar and porous anodes at different current densities (0.2C, 0.5C, 1C, 2C and back to 0.2C) was performed and is presented below (Figure 28). This test was performed in coin cell configuration and the cells were charged from 1.4 V to 2.1 V. The porous anode shows a higher discharge capacity at all C-rates (average discharge capacity at 0.2C, 0.5C, 1C, and 2C were measured to be 135.4 mA h g⁻¹, 129.5 mA h g⁻¹, 118.5 mA h g⁻¹, and 97.7 mA h g⁻¹, respectively) compared to that of the planar anodes (average discharge capacity at 0.2C, 0.5C, 1C, and 2C were measured to be 116.7 mA h g⁻¹, 112.0 mA h g⁻¹, 103.8 mA h g⁻¹, and 89.0 mA h g⁻¹, respectively). Furthermore, both the anodes exhibit excellent reversibility in discharge capacity when they were cycled back to 0.2 C (the planar and porous anode displayed 96.0% and 97.9% retention, respectively). To demonstrate the performance of the porous anode in a large-scale battery application, the rate performance of the planar and porous anodes was

performed and compared in 7 mA h batteries (See Appendix B for a schematic of 7 mA h batteries and rate performance results). An improvement in the rate performance of the porous anode was observed in these big batteries.

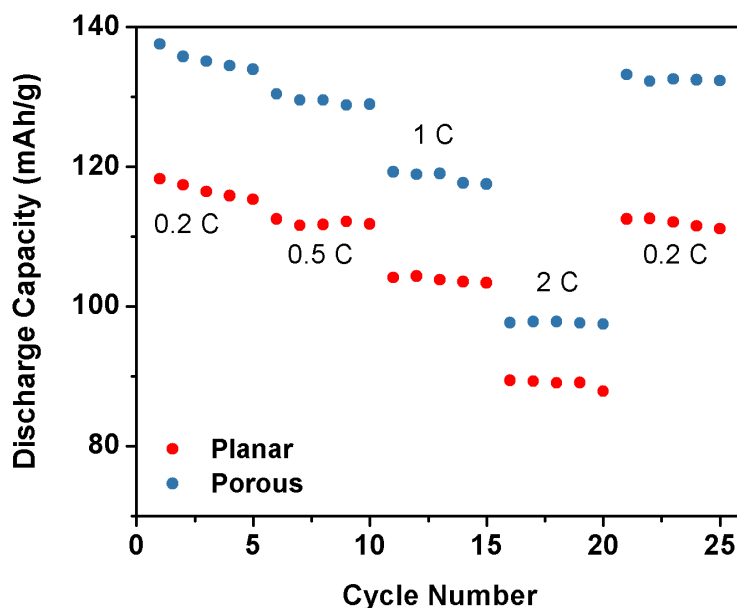


Figure 28: Discharge capacity at different C-rates of planar and porous zinc anodes

The float charge current test was performed by charging the coin cell from 1.4 V to 2.1 V and once charged, the cells were maintained at a potential of 2.1 V for 72 hours. The current drop after 72 hours was recorded and is presented in Figure 29. Porous zinc anode shows a lower float charge current ($0.15 \mu\text{A}$) compared to that of the planar anode ($1.6 \mu\text{A}$). This lower float current indicates that batteries with a porous anode undergo less detrimental irreversible side reactions that are responsible for float charge current [77]. These side reactions usually involve the evolution of gases, for example, oxygen and hydrogen [78]. To measure the evolution of gas during float charge, the planar and porous anodes were implemented in big batteries (7 mA h) and cycled using the float charge test. The amount of gas evolved during the float charge was measured (see

Appendix C for gas evolution test apparatus images). Battery with porous anode shows a lower gas evolution volume (43 ml) than the battery with the planar anode (53.5 ml). Hence, it is concluded that batteries with a porous anode produce less gas than the planar anode, mainly due to the presence of additives (lead oxide and bismuth oxide) in the porous anode.

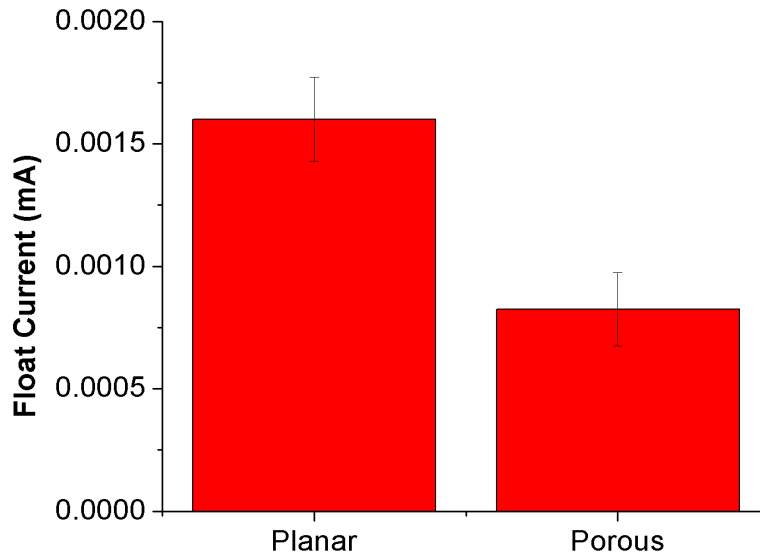


Figure 29: Float charge current profile for planar and porous anode after 72 hours

3.3.3 Advanced Characterizations

Linear polarization characterization was conducted in a three-electrode system with zinc foil and Ag/AgCl as the counter and a reference electrode, respectively. The potential was scanned from -1.2 V to -0.8 V. Linear polarization curves of porous and planar zinc anodes are presented in Figure 30.

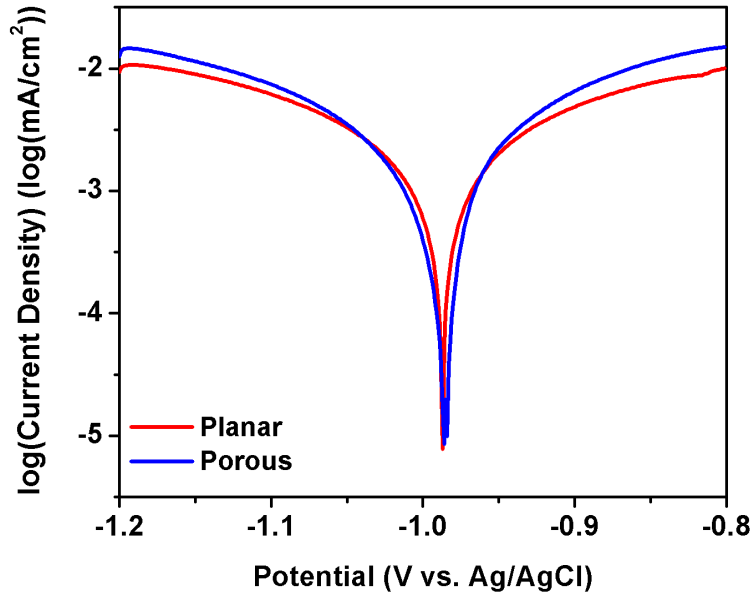


Figure 30: Tafel plot of planar and porous zinc anodes

The corrosion current density (i_{corr}) and corrosion potential (E_{corr}) were obtained by fitting the plot with Tafel extrapolation, the results of which are tabulated below (Table 3). The porous anode displays slightly lower corrosion potential (improvement of 1.25 mV) and corrosion current density (improvement of $111 \mu\text{A cm}^{-2}$). This improvement in the corrosion properties of the porous anode is mainly due to the presence of additives (PbO and Bi_2O_3) in the porous anode. Since there are many other possible additives choices and composition that can add to the anode to further improve its corrosion properties, the porous anode can be configured to one's needs.

Table 3: Summary of corrosion potential and current density extrapolated from Tafel fit

Sample	E_{corr} (V vs Ag/AgCl)	I_{corr} (mA/cm²)
Planar	-0.9865	1.051
Porous	-0.9853	0.940

Chronoamperometry (CA) was performed to study the dendrite formation and growth on planar and porous zinc anodes during charging of batteries. These tests were performed on a three-electrode system with zinc foil and Ag/AgCl as a counter and working electrodes, respectively, with over-potential of 135 mV. The current –time profile for a span of 10 seconds is shown in Figure 31. Planar anode shows a significant drop in current density (current density drop to 6 mA cm^{-2} approximately) initially which suggests fast nucleation of the zinc dendrites [79]. Furthermore, after the initial current drop, the current density rises a little and then continues to decrease after 2 seconds. This decrease in current density is caused by an increase in surface area of the planar anode. Meanwhile, the initial current density drop in the porous anode is significantly less (current density drop of 1.25 mA cm^{-2}). This increase in surface area is due to the dendritic zinc growth [80]. After the initial current density drop, the current density profile of the porous anode is relatively flat, which indicates little or no increase in its surface area. Hence dendritic growth is effectively suppressed after dendritic nucleation.

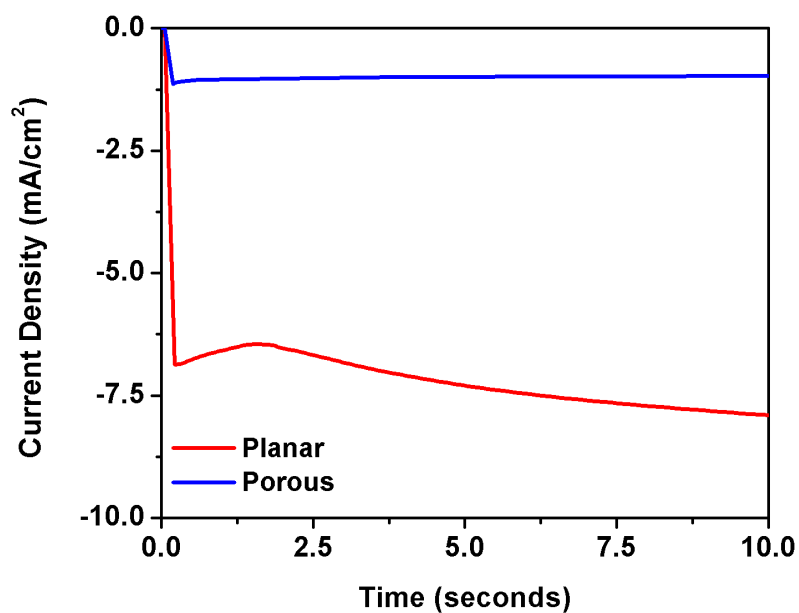


Figure 31: Current-time profile of planar and porous zinc anodes for 10 seconds

The current-time profile for the sample over the span of 1 hour is presented in Figure 32. After the initial current density drop, the absolute current density of porous anode remains significantly lower than that of the planar anode.

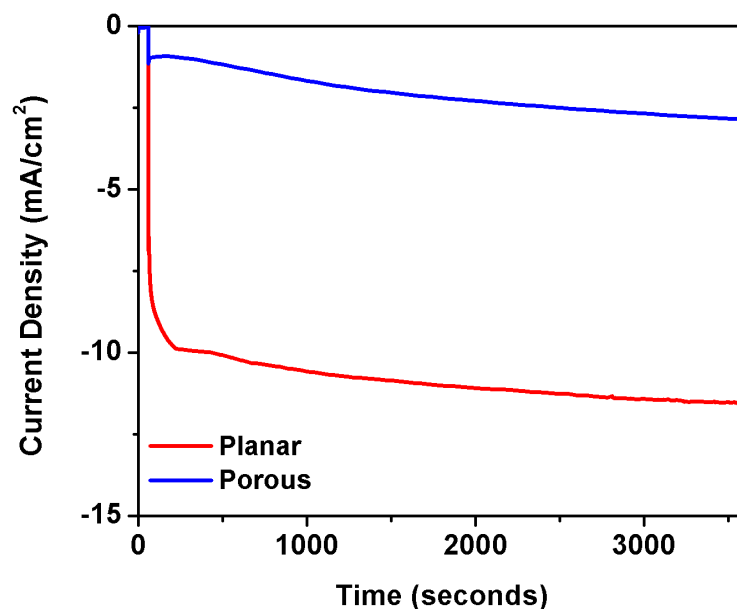


Figure 32: Current-time profile of planar and porous zinc anodes for 1 hour

SEM images of planar and porous anodes after 1 hour of CA is presented in Figure 33. The dense and irregular growth of metallic zinc with different morphologies is observed. The planar anode exhibits dendrites with stacked flat plane structures, while the porous anode exhibits plane-like dendrites.

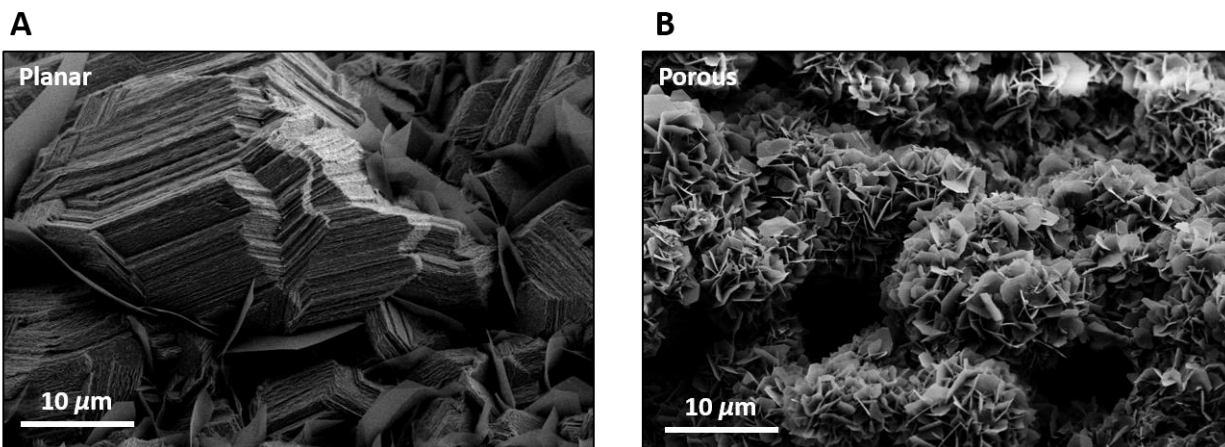


Figure 33: SEM images of (A) planar and (B) porous zinc anodes after 1 hour of CA

Cyclic Voltammetry (CV) was performed in three electrode system inside a Swagelok cell configuration. Zinc foil and Ag/AgCl were used as the counter and reference electrodes, respectively. The CV plot is presented in the figure below (Figure 34). The areas under the curves were measured, and the porous anode shows the significantly higher area under the reduction region compared to that of the planar anode. Hence, the porous anode surface exhibits a higher electrochemically active surface area compared to the surface of the planar anode. Furthermore, the increased surface area of the porous anode surface leads to more zinc ion diffusion, which results in higher current density in oxidation and reduction peak positions [81].

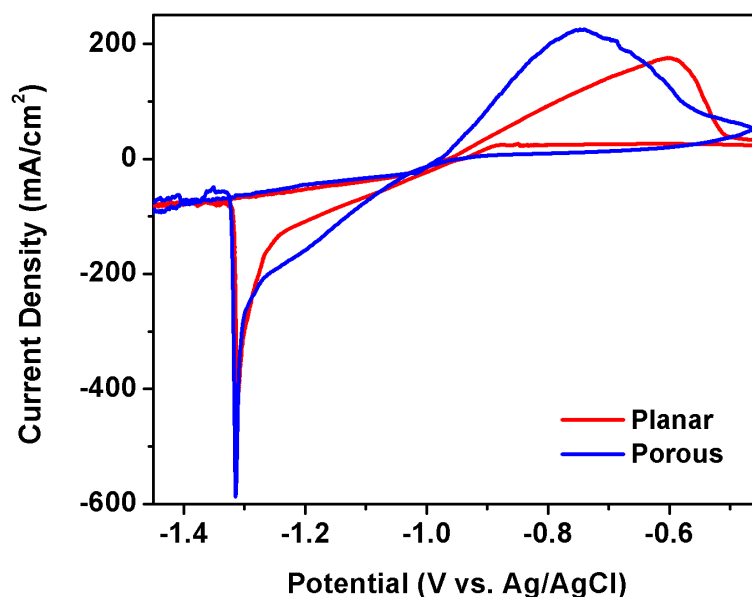


Figure 34: CV plot of planar and porous zinc anodes

XRD was performed on the planar and porous zinc anodes before and after 1 hour of chronoamperometry to study the zinc crystal growth in different orientations. The XRD plot is presented in the figure below. Different planes, which corresponds to zinc, including (002), (100), (101), (102), (103), and (110) were observed for all samples. These peaks have been reported in

the literature [82]. The peak intensities of all the samples in the figure below have been normalized with the (101) peak. The peak, corresponding to (101) direction, is dominant in all of the samples. Moreover, an increase in the relative intensity of (103) peak is observed for a porous anode after chronoamperometry (before and after chronoamperometry I_{103}/I_{101} is 0.14 and 0.21, respectively). It is relevant to mention that the zinc crystal growth in (103) direction is nearly parallel to anode surface ($0-30^\circ$ relative to anode surface), while the growth in (101) direction is almost perpendicular to the anode surface ($70-90^\circ$ relative to anode surface) [83]. For the planar anode, there is a decrease in the relative intensity of (103) peak (I_{103}/I_{101} before and after chronoamperometry is 0.39 and 0.33, respectively). Since the crystal growth in (101) direction is perpendicular to the surface, this plane direction is associated with dendritic growth. This situation suggests that in the porous zinc anode, there is more zinc crystal growth in the preferred direction (103) than there is with a planar one.

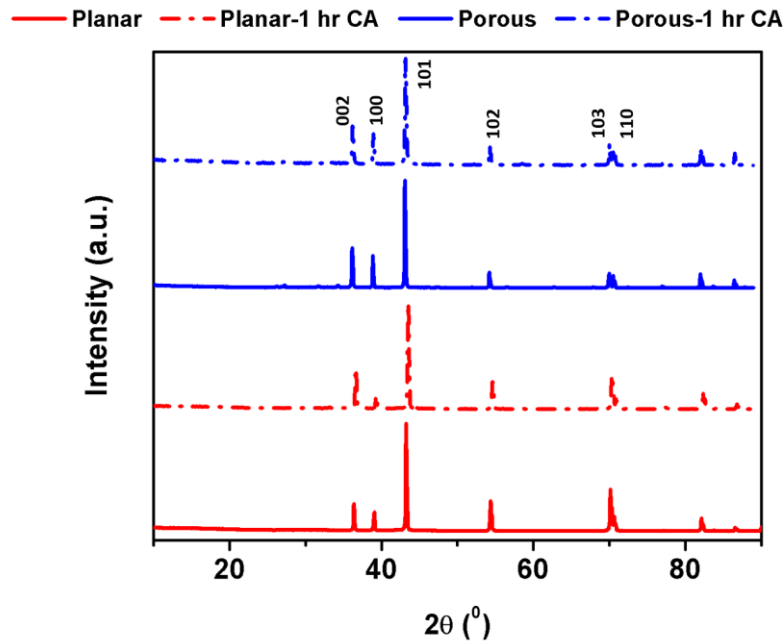


Figure 35: XRD of planar and porous zinc anodes before and after 1 hour of CA

3.4 Conclusions

A porous zinc anode was successfully fabricated and implemented in aqueous lithium batteries. The anode was fabricated using a slurry method. The fabrication parameters, including the zinc powder type, anode composition, and zinc powder particle sizes, were optimized based on their respective effect on cycling performance.

The material and electrochemical surface properties of the porous anode was compared with those of the commonly used planar zinc anode. SEM and AFM confirm that the surface area of the porous anode is significantly higher than that of the planar anode (surface area of 15 μm by 15 μm plane of porous anode and the planar anode is 400 μm^2 and 225 μm^2 , respectively). Furthermore, the porous anode displays better wettability to water, as shown by the contact angle measurements.

Coin cells with the porous anode display a 32% improvement in initial discharge capacity (136.28 mA h g^{-1} for the porous anode vs 103.42 mA h g^{-1} for the planar one) and higher cycling retention. Furthermore, batteries with the porous anode displayed a significantly higher discharge capacity at various C-rates ranging from 0.2C to 2C, in coin cells and big batteries (7mA h). These batteries also exhibit lower float charge current after 72 hours (0.15 μA for batteries with a porous anode compared to 1.6 μA for ones with a planar anode). This reduction in float charge current is associated with a reduction in the side reactions and hydrogen evolution on the anode surface. This finding is confirmed by gas evolution measurement during 72 hours of float charge in big batteries (7 mA h), where batteries with the porous anode showed a 24 % reduction in gas volume evolved compared to ones with the planar anode.

Tafel extrapolation on linear polarization curves showed that the porous anode had slightly lower corrosion current density (1.051 mA cm^{-2}) than to the planar anode (0.940 mA cm^{-2}). The current-

time profile revealed that the porous anode demonstrated significantly lower dendritic nucleation and growth. Cyclic voltammetry characterization demonstrated that the porous anode has a higher electrochemically active surface area than the planar anode. SEM images reveal a difference in the structure morphologies of zinc metal deposition on the planar (stacked planes) and porous (planes) zinc anodes. Based on the planes of zinc crystal growth observed on XRD after 1 hour of chronoamperometry, it is suggested that the porous anode promotes more zinc deposition parallel to the anode surface than the planar anode does.

Chapter 4: Graphene as Artificial Solid Electrolyte Interphase on Anode

4.1 Fabrication of Graphene coated Porous Zinc Anodes

4.1.1 Synthesis of Graphene Oxide

Graphene oxide (GO) synthesis was based on an improved Hummer's method with a slight modification to its procedure [34]. First, 3 g of graphite flakes were dissolved in 360 ml of concentrated H_2SO_4 via magnetic stirring for approximately 1 hour. Then, 40 ml of H_3PO_4 was then added to this mixture, and the resulting mixture was stirred for 15 minutes. Next, 18 g of KMnO_4 was added slowly, and the resulting mixture was stirred for another 1 hour at room temperature, then is stirred at 50 °C for 12 hours in a water bath. The resulting mixture was dark-brown in after this step, indicating that the graphite flakes were oxidized. To stop its oxidation, the mixture was poured onto 400 ml of a cold solution of 30 % H_2O_2 in distilled water. The solution is then centrifuged at 4000 rpm for 4 hours, followed by disposal of the supernatant. The solid obtained was purified GO, which was dried in air under a fume hood. Approximately 3 g of purified GO was obtained as the final product.

4.1.2 Fabrication of Porous Zinc Anodes

Binder was prepared by mixing 2.5 weight percent (wt. %) of hydroxyl-propyl methylcellulose (HPMC), 1.25 wt. % of poly (acrylic acid) (PAA), and 1.25 wt. % of polyvinyl alcohol (PVA) in DI water. A slurry containing purum zinc powder, binder, and additives was prepared. A slurry containing 96 weight percent (wt. %) purum zinc powder, 2 wt. % gel binder, and 2 wt. % additives were prepared and coated on the brass substrate. The anode surface was dried and flattened before use (See section 3.1). This prepared anode was used for subsequent GO coatings and experiments.

4.1.3 Coating of GO onto Porous Zinc Anode Surface

An illustration of the Langmuir trough used to coat the GO onto the porous anode is shown in Figure 36. The instrument consists of the trough, barriers, balance with Wilhelmy plate, and an interface device to control the devices and communicate with the computer. The trough is made with a hydrophobic plastic (Polytetrafluoroethylene (PTFE)), has a surface area of 273 cm², subphase volume of 283 ml, and a well in the middle. The barrier, whose position can be controlled, can adjust the surface pressure by changing the area available to the substrate. The balance consists of a clean paper plate attached to very sensitive electro-balance, which measures the force acting on the plate [84].

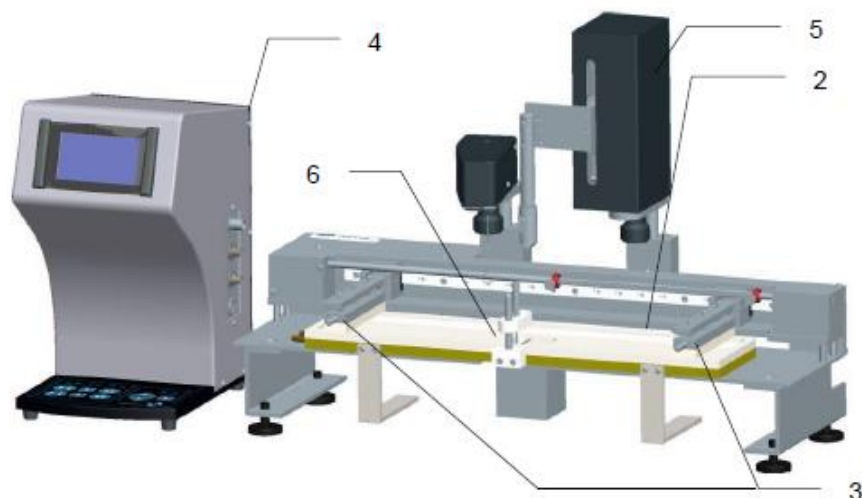


Figure 36: Illustration of Langmuir trough instrument with a (1) balance, (2) trough, (3) barriers, (4) layer-builder, (5) dipper and (6) well

First, GO was dissolved in a solution containing dichloromethane (DCE) and ethanol to give a final GO concentration of 0.25 mg ml⁻¹. The solution was centrifuged to ensure uniform dispersion of GO suspensions. Before using the trough, it was cleaned thoroughly in ethanol and then rinsed with DI water. Then it was filled with approximately 275 ml of DI water. Water is the sub-phase in this coating procedure. Then anode, with the zinc surface facing up, was carefully inserted

underneath the water surface in the trough. Different volumes of GO solution in was gently added dropwise on top of the water surface at a drop rate of 0.1 ml s^{-1} . After the desired quantity of GO solution was dropped onto the water surface, it was left for about 20 minutes to ensure DCE and ethanol were evaporated completely. Hence, only GO suspensions were left floating on top of the water surface. The barriers were compressed which, in turn, compressed the GO suspensions and the surface pressure with respect to barrier surface area were recorded (Figure 37). After the barriers were at its desired position, the water sub-phase was sucked out using as an aspirator tip connected to a vacuum pump. When the water level dropped to the level of the anode surface, GO was coated onto the surface of the anode.

Furthermore, Figure 37 shows the surface pressure change (mN m^{-1}) with the GO film area during barrier compression. Upon compression, GO nanosheets come close to each other, and the surface pressure increases with compression (which decreases the GO film area) as a result. The steady increase in surface pressure with GO film area comes under phase II region. Further compression causes the conversion of 2D structure to 3D structure (phase III). The anodes were coated at the

surface pressure very close to the end of phase II, right before the start of phase III, to make sure maximum GO surface coverage is achieved without damaging the 2D structure.

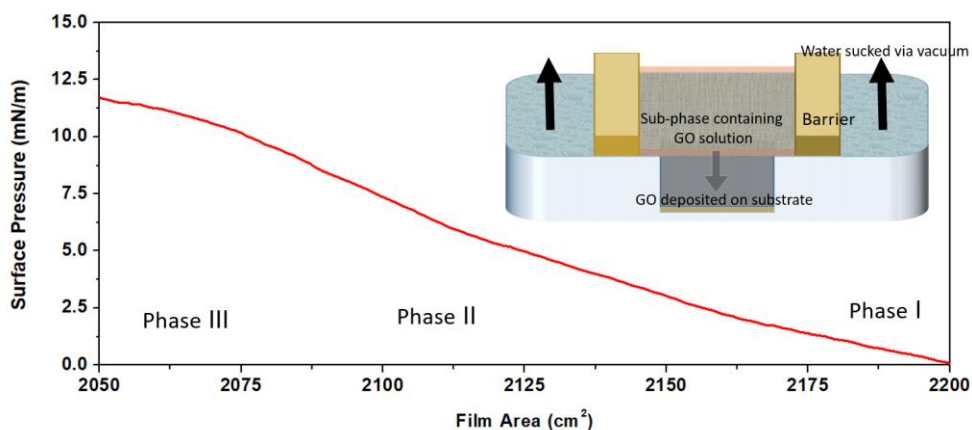


Figure 37: Surface pressure as a function of the trough area in the Langmuir trough method. Inset: Schematic of the Langmuir trough coating technique used in this work

GO on the porous anode surface was then reduced to reduced graphene oxide (RGO) by exposing the porous anode surface to water vapor at 60 °C for 5 hours. This RGO coated porous zinc anode was used for subsequent experiments. To see the effect of water vapor exposure on the oxidation of porous zinc anode, XRD on the porous zinc anode before and after water vapor exposure was conducted. No significant zinc oxide peaks were observed after water vapor exposure (see Appendix C), which shows this reduction technique did not oxidize the porous zinc anode.

In this work 1, 10, 50 and 100 layered RGO coated anodes (named 1RGO, 10RGO, 50RGO, and 100RGO, respectively) were prepared. RGO of different layers were coated by changing the volumes of GO solution (0.25 mg ml⁻¹ GO in ethanol and DCE) used during Langmuir trough coating procedure.

4.2 Basic Characterizations of RGO coating on Porous Zinc Anodes

Scanning electron microscopy (SEM) was used to observe the blank, 10RGO and 100RGO coatings on the porous zinc anode (Figure 38). For the blank sample, zinc particle agglomerates of varying sizes and shapes are observed. The sizes of these agglomerates range from a few microns to 25 μm . RGO coating on the porous zinc anode is easily observable in the 10RGO and 100RGO samples, in which the characteristic wrinkles of graphene sheets are observed. Furthermore, bright regions on the SEM images of RGO sheets are observed and are due to negative charge accumulation during imaging. Reduced graphene oxide is not very conductive, and hence it accumulates negatively charged electrons on its surface during SEM imaging. These accumulated charges repel the electrons subsequently striking the surface and, hence, the secondary electron detector becomes saturated with these repelled electrons. As a result, these particular regions containing thick RGO coatings appear as bright or white spots in the images.

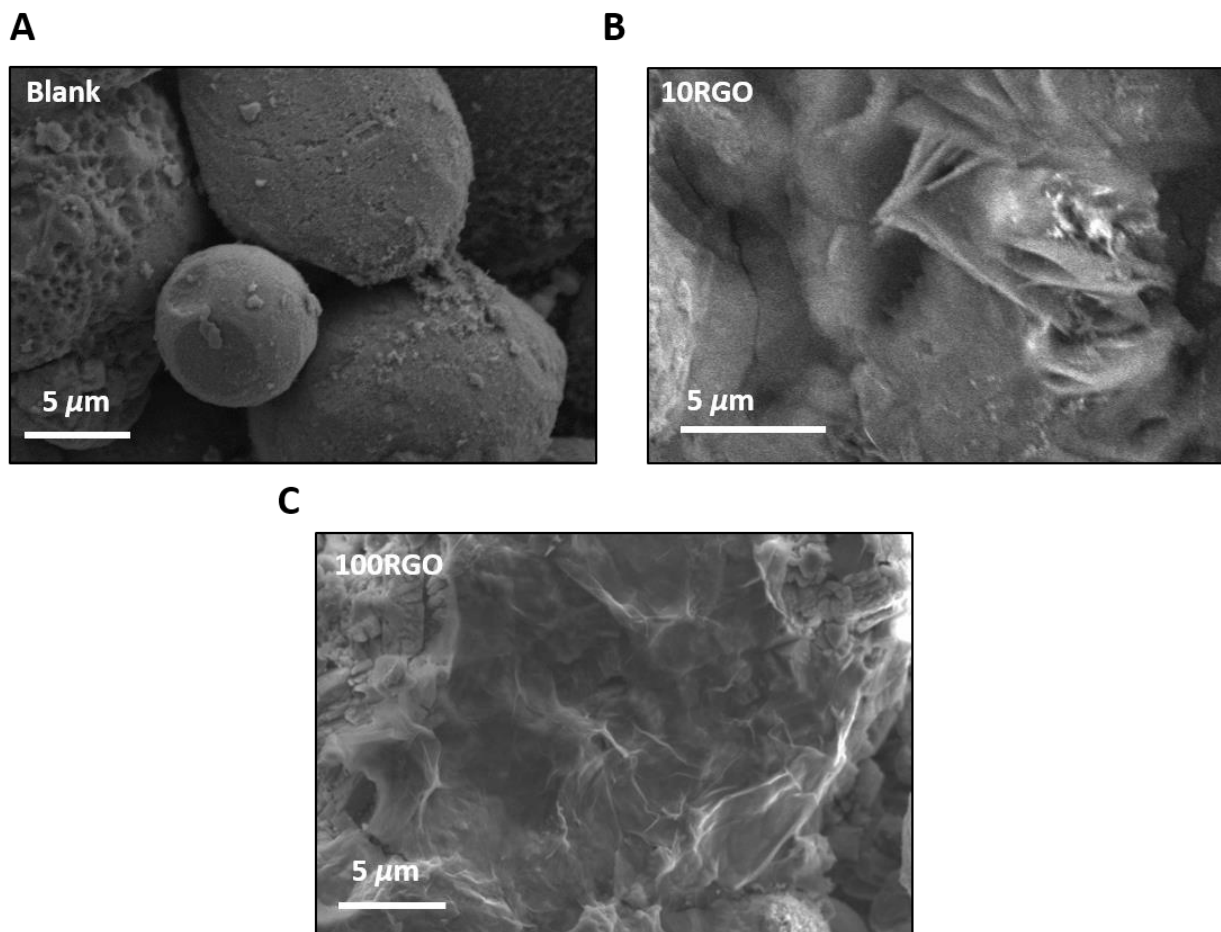


Figure 38: SEM images of (A) blank (B) 10RGO and (C) 100RGO

Energy dispersive x-ray (EDX) analysis was also carried out on the SEM images (Figure 39). For the blank sample, a very intense zinc peak is observed. 10RGO shows additional peaks associated with carbon and oxygen; however, these peaks have very low relative intensity. For 100RGO, intense carbon, oxygen, and zinc peaks are observed. Compared to 10RGO, 100RGO shows a carbon peak with higher relative intensity, signifying that 100RGO has a thicker graphene coating than that of 10RGO.

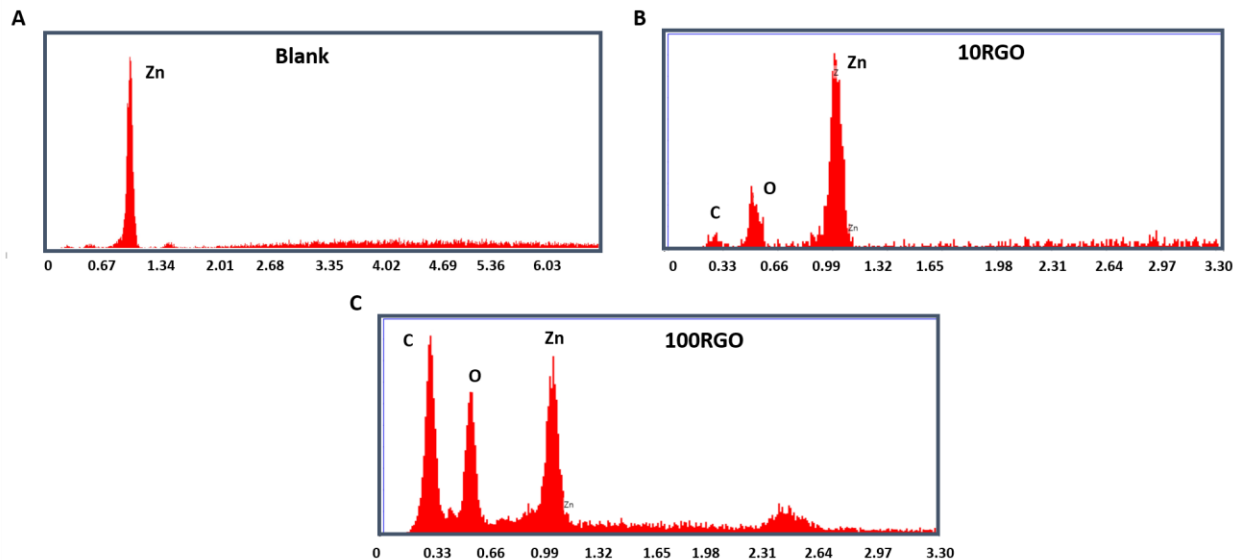


Figure 39: Figure 12: EDX results of (A) blank (B) 10RGO and (C) 100RGO

To complement the SEM images, AFM was done on the blank and 100RGO samples. Figure 40 shows the height profiles of these samples. For both samples, a height variation of $9\ \mu\text{m}$ was observed. For the blank sample, sharp boundaries of zinc particle agglomerates are observed. However, after the RGO coating, these boundaries disappear, and the surface appears smoother than the surface of the blank. This smoothness of the porous anode is due to the RGO surface coating.

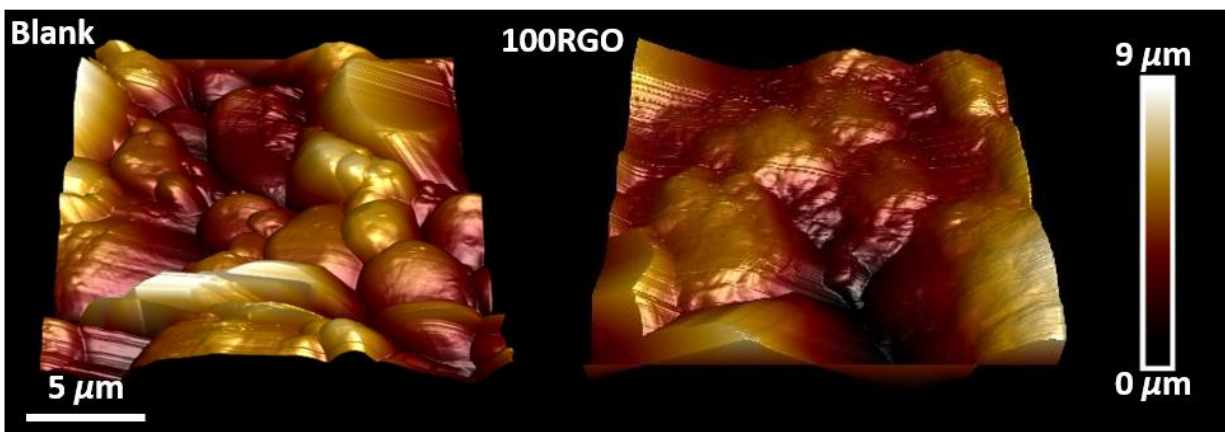


Figure 40: AFM images of blank (left) and 100RGO (right)

Contact angle measurements were also carried out on the blank, 10RGO, and 100RGO samples (Figure 41). The blank sample shows a contact angle of 65° with the water droplet. However, after coating with GO, the surface contact angle decreases to 6° , for two reasons; first, GO has hydrophilic oxygen functionalities on its basal plane and second, GO coating has a smoother surface profile compared to that of the blank (Figure 40). After reduction to RGO, the contact angle increases to 26° because of the loss of oxygen functionalities. However, the contact angle RGO-coated porous anode is less than that of the blank, because the former's surface is smoother than that of the blank.

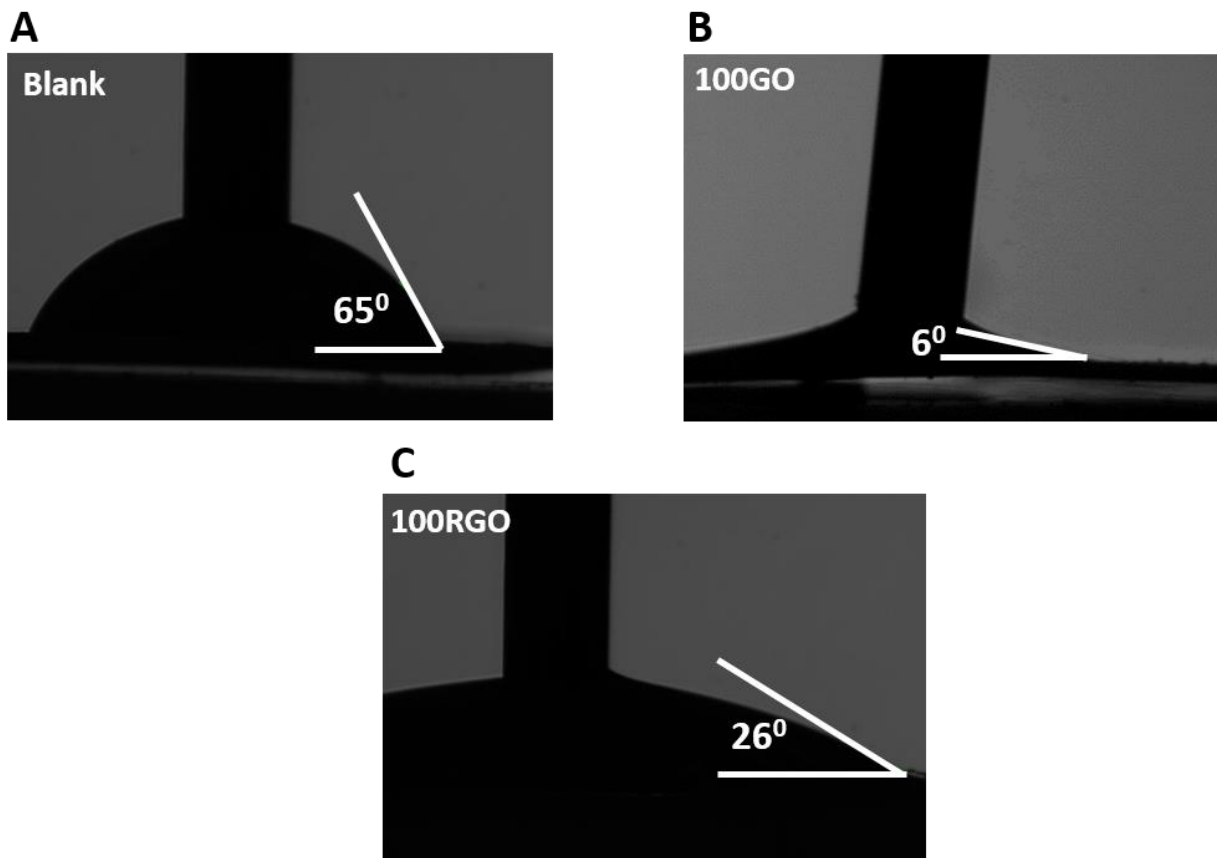


Figure 41: Contact angle measurements of (A) blank (B) 100GO and (C) 100RGO

4.3 Basic Electrochemical Characterizations

4.3.1 Linear Polarization Plot

The linear polarization curves of the blank, 1RGO, 10RGO, 50RGO, and 100RGO are shown in Figure 42. The corrosion current density (i_{corr}) and corrosion potential (E_{corr}) were obtained by fitting the plot with Tafel extrapolation (Table 4). All graphene-coated anodes show a lower corrosion current density than does the blank, with 10RGO showing the lowest corrosion current density. 1RGO and 10RGO show a more positive corrosion potential than the blank. When a single layer of RGO is coated on to the anode surface, the corrosion current and corrosion potential improve significantly compared to that of the blank sample. Moreover, compared with 1RGO, 10RGO shows better corrosion properties because 10RGO has a thicker graphene coating with better RGO surface coverage of its porous anode surface. Improving corrosion properties by increasing the number of graphene layers have been reported in the literature [85]. However, a thicker graphene coating (50RGO and 100RGO) leads to increased corrosion current density compared to that of 1RGO and 10RGO. Even then, 50RGO and 100RGO have lower corrosion current density compared to that of the blank sample. From overall Tafel results, it can be concluded that graphene coatings act as strong passivation layers against corrosion in porous zinc anodes.

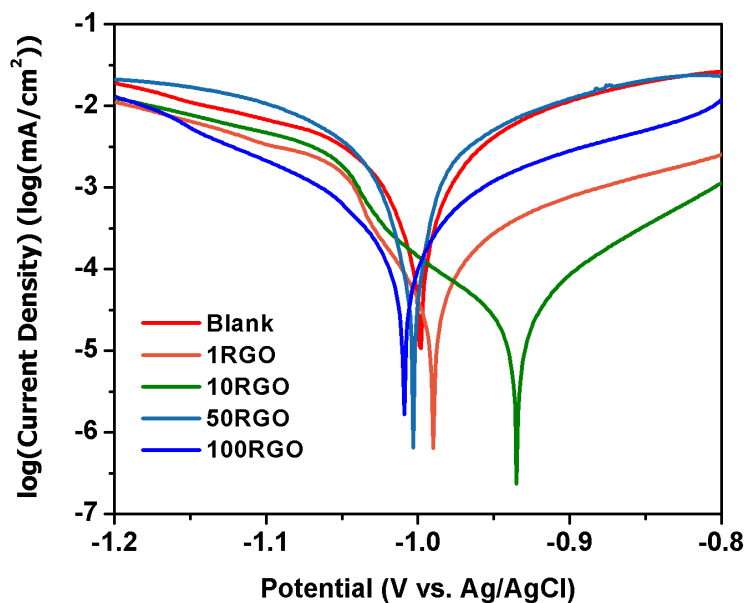


Figure 42: Tafel plot of blank and RGO coated porous zinc anodes

Table 4: Summary of corrosion potential and current density extrapolated from fitting Tafel extrapolation

Sample	E_{corr} (V vs Ag/AgCl)	I_{corr} (mA cm ⁻²)
Blank	-0.998	1.0455
1RGO	-0.997	0.1067
10RGO	-0.935	0.0333
50RGO	-1.003	0.6280
100RGO	-1.009	0.2704

4.3.2 Chronoamperometry

A profile of current density with respect to time for the blank, 1RGO, 10RGO, 50RGO, and 100RGO samples for a time span of 30 seconds is presented in Figure 43. These tests were performed in a three electrode system, with zinc foil and Ag/AgCl as the counter and reference

electrodes, respectively. An over-potential of 200 mV was used. For the blank sample (no graphene coating), the current density dropped to 7 mA cm⁻² after 10 seconds suggesting fast nucleation on the zinc anode. However, the RGO-coated porous zinc anodes (except for 50RGO) show a much less severe drop in the current density (for example, 10RGO shows the current density dropped to 5mA cm⁻²), and over a longer period (for example, for 10RGO, the drop occurred over approximately 7 seconds compared with that of the blank which occurred in 12 seconds). A more gradual drop in the current density can be translated to a longer zinc ion adsorption process and more-uniform deposition of the zinc atoms.

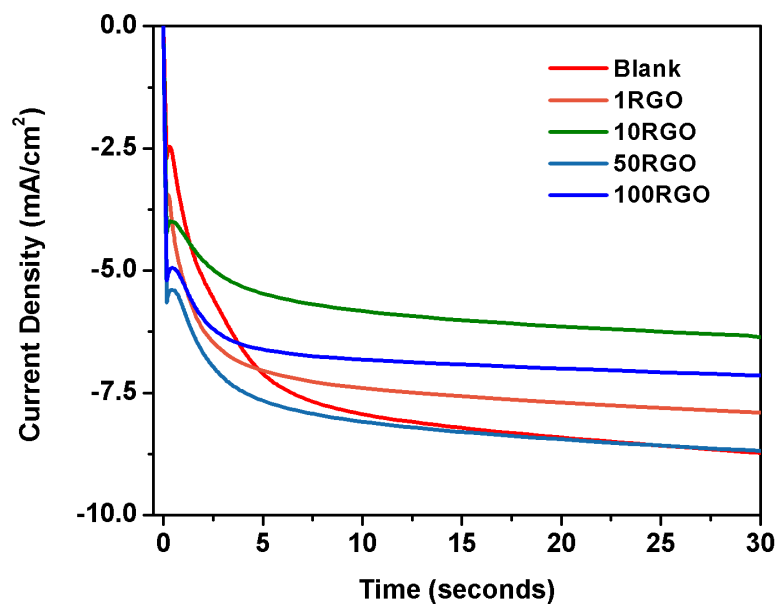


Figure 43: Current-time profile of blank and RGO coated porous zinc anodes for 30 seconds

Figure 44 shows the current-time profile for the same samples over a time span of 1 hour. The current density drop for all RGO coated samples is less than that for the blank. 10RGO shows the lowest current drop after 1 hour (-11.6 mA cm⁻²), followed by 100RGO (-12.6 mA cm⁻²), 50RGO (-16.3 mA cm⁻²), 1RGO (-18.0 mA cm⁻²), and blank (-18.6 mA cm⁻²). Moreover, for 10RGO,

50RGO, and 100RGO sample, the change in current density after 1000 seconds is much more gradual than that of the blank and 1RGO. This increase in current density (of blank and 1RGO) relates to an increase in the surface area of the electrode surface due to dendritic nucleation and growth. Hence this suggests that 10RGO, 50RGO, and 100RGO coated porous anodes have lower dendritic nucleation and growth.

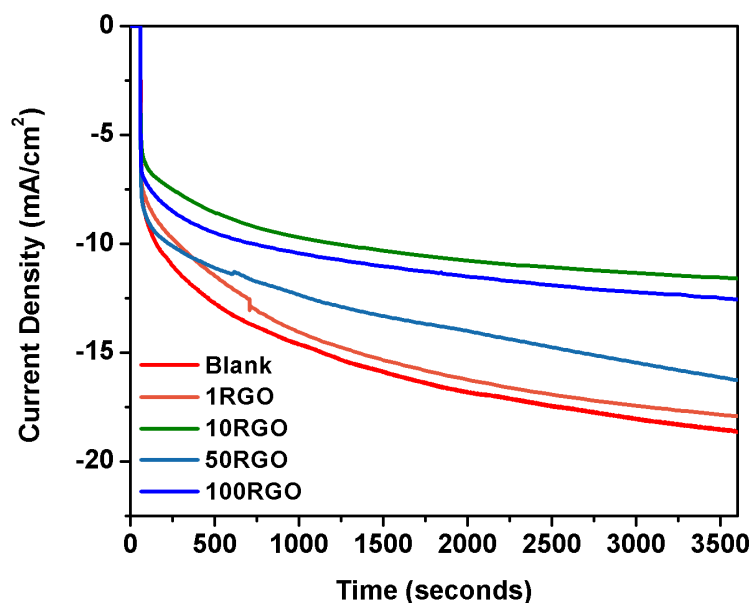


Figure 44: Current-time profile of blank and RGO coated porous zinc anodes for 1 hour

4.4 Battery Testing

Cyclic voltammetry, cycle life, rate capability, float current, and capacity were tested in coin cell configuration. The cathode was prepared by casting a slurry containing lithium manganese oxide (LMO), conductive carbon and PVDF binder onto polyethylene (PE) film. AGM glass fiber was used as the separator. An aqueous electrolyte (pH 4) containing 1 M LiSO_4 and 2 M ZnSO_4 was used.

4.4.1 Cyclic Voltammetry

Cyclic voltammetry (CV) was performed on all RGO coated porous anodes and compared with the blank at a scan rate of 1 mV s^{-1} , as shown in Figure 45. This set of experiments was performed to determine the effect of RGO coating on the redox reactions of this aqueous battery system. Two redox couples, located at $1.88 \text{ V} / 1.7 \text{ V}$ and $2.00 \text{ V} / 1.85 \text{ V}$ vs Zn^{2+}/Zn , were observed. These two redox couples correspond to the extraction and insertion of Li^+ from and into the host spinal structure of lithium manganese oxide in the aqueous electrolyte, respectively [7]. The symmetry of the peaks shows that these reactions are highly reversible. Overall, RGO coatings have no observable effect on the Li^+ insertion and extraction into/from the cathode.

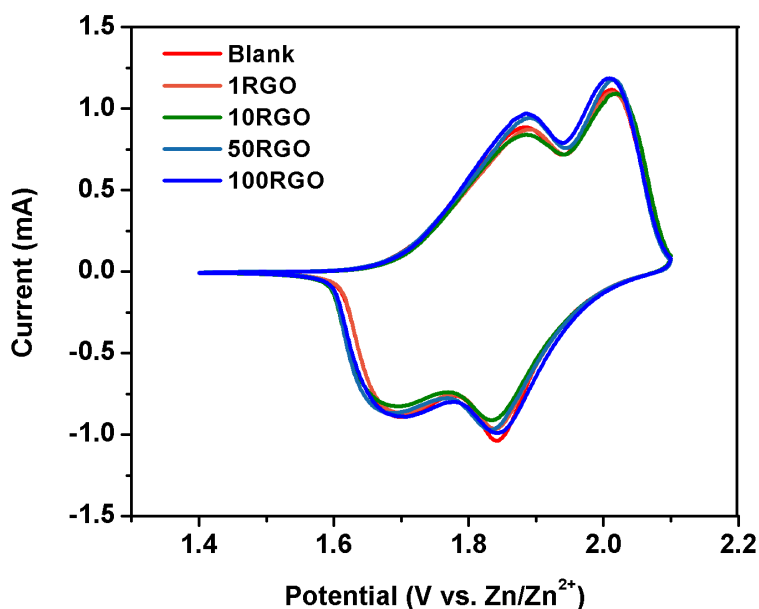


Figure 45: CV profile of Blank and RGO coated porous zinc anodes at a scan rate of 1 mV s^{-1}

4.4.2 Cycle Life

The anode samples were assembled in a coin cell configuration and tested for cycle life. The batteries were run at the current density of 4C under CC-CV mode, with a time cut-off of

15 minutes. These batteries were charged from 1.4 V to 2.1 V. The discharge capacity was recorded after every charge-discharge cycle and plotted as a function of cycle number (Figure 46A).

The initial discharge capacity and cycling retention after 300 cycles is presented in Figure 46, with 100RGO shows the highest discharge capacity ($102.72 \text{ mA h g}^{-1}$), followed by 10RGO ($95.36 \text{ mA h g}^{-1}$), blank ($91.15 \text{ mA h g}^{-1}$), 50RGO ($88.75 \text{ mA h g}^{-1}$) and 1RGO ($86.14 \text{ mA h g}^{-1}$). All the RGO coated anodes samples show significantly better cycling retention for all cycles leading up to 300 cycles. As shown in Table 5, 100RGO shows the highest cycling retention, followed by 10RGO, 50RGO, 1RGO and blank.

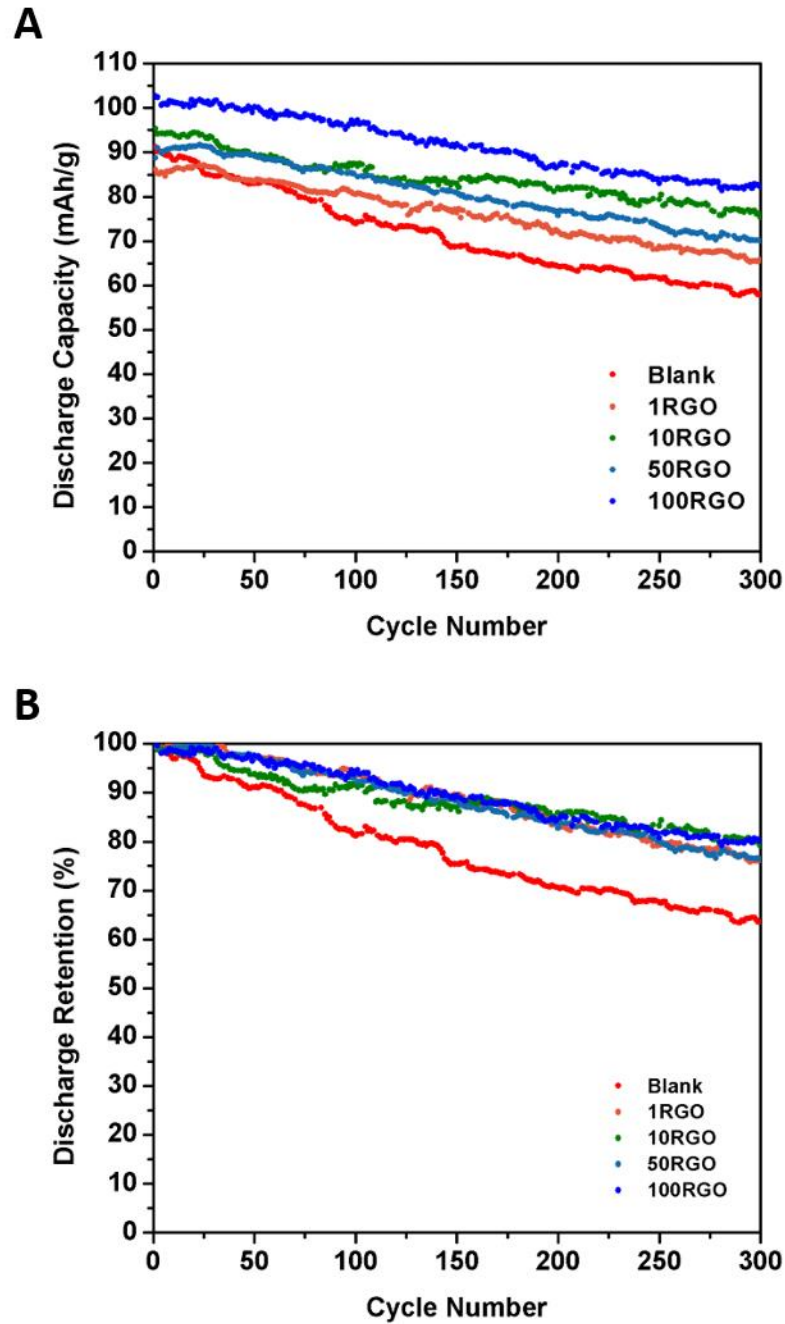


Figure 46: (A) Cycle life and (B) retention in discharge capacity of blank and RGO coated porous zinc anodes

Table 5: Summary of initial discharge capacity and percent retention in discharge capacity after 300 cycles at the current density of 4C

Sample	Initial Discharge Capacity (mA h g⁻¹)	% retention in discharge capacity after 300 cycles
Blank	91.15	64.74
1RGO	86.14	76.79
10RGO	95.36	80.94
50RGO	88.75	77.78
100RGO	102.72	82.88

Galvanostatic charge-discharge curves for blank and 100RGO after 1st and 300th cycles are presented in Figure 47. The two plateaus observed in the charge-discharge profile correspond to the CV profile and are related to two stages of the Li⁺ extraction/insertion behavior in the cathode. 100RGO shows higher charge and discharge capacity after the 1st and 300th cycle compared to that of the blank.

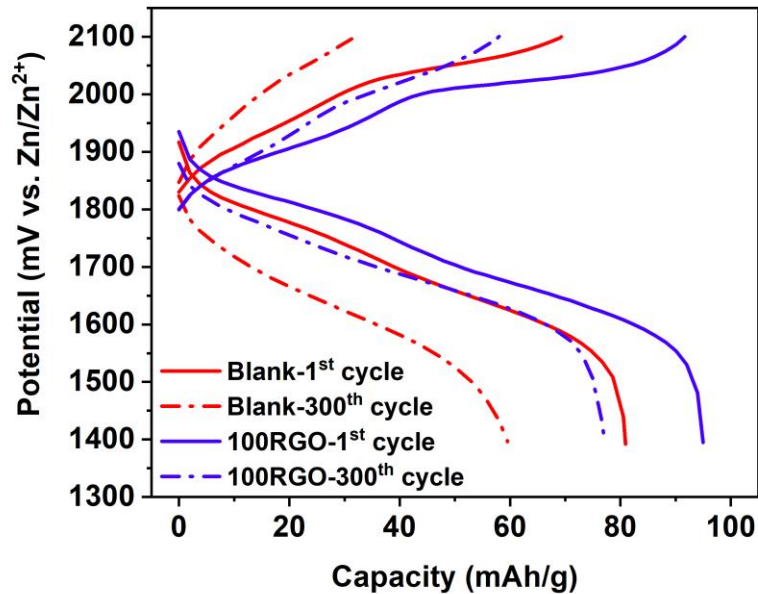


Figure 47: Charge-Discharge curves of blank and 100RGO after 1st and 300th cycle

4.4.3 Rate Capability

The rate performance of RGO coated anodes under different C-rates (0.2C, 0.5C, 1C, 2C, 4C and back to 0.2C) is shown in Figure 48. In general, RGO coated anodes show higher discharge capacity compared to that of the blank. Especially at higher C rate, such as 4C, the discharge capacity of 1RGO, 10RGO and 100RGO (around 75 mA h g⁻¹) is significantly higher than that of the blank (60 mA h g⁻¹). When cycling at 0.2C towards the end of the experiment, all batteries exhibited good rate reversibility.

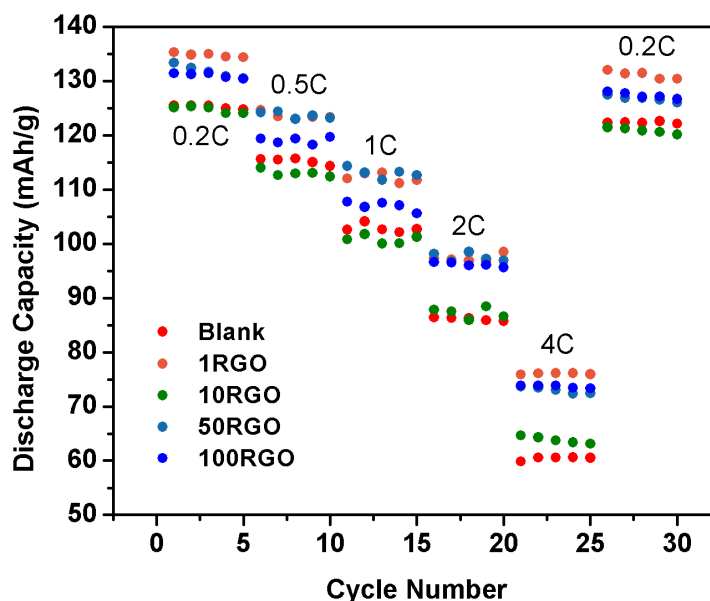


Figure 48: Discharge capacity at different C-rates of blank and RGO coated porous zinc anodes

4.4.4 Open Circuit Voltage

Open circuit voltage (OCV) was carried out in all the samples, the result of which is shown in Figure 49. The batteries were first charged to 2.1 V and then left standing without any potential for 72 hours. The potential in the batteries was recorded during this period. Slightly greater potentials of all RGO-coated anodes were observed than that of the blank. The potential of the blank, 1RGO, 10RGO, 50RGO, and 100RGO samples after 72 hours was 1963.9 mV, 1967.0 mV, 1968.6 mV, 1968.3 mV and 1965.8 mV, respectively. From OCV results, we conclude that RGO coating does not interfere with the potential drop in the batteries if they are left standing.

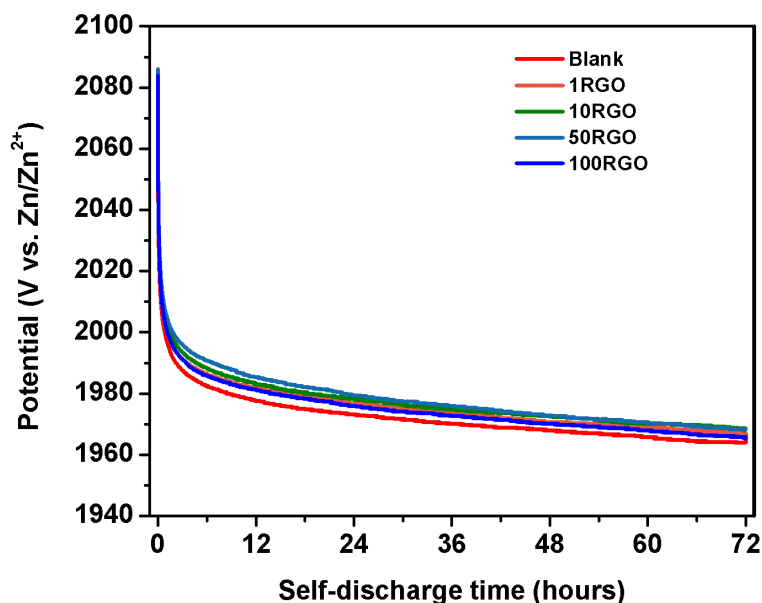


Figure 49: Self-discharge curves of blank and RGO coated porous zinc anodes for 72 hours

4.5 Advanced Characterizations

4.5.1 Electrochemical Impedance Spectroscopy

Electrochemical impedance spectroscopy (EIS) was conducted on the blank, 10RGO and 100RGO samples before and after battery cycling in a three-electrode system, the Nyquist plot of which is shown in Figure 50. The diameter of the semicircle in the Nyquist plot equals to the charge transfer resistance (R_{ct}) at the electrode-electrolyte interface. EIS data was fitted using an equivalent circuit. R_{ct} of the blank, 10RGO, and 100RGO before battery cycling were calculated to be around 563 Ω , 243 Ω and 222 Ω , respectively. Lower R_{ct} of the RGO-coated anodes correspond to an improvement in zinc ion transport behavior in the electrolyte-anode interface, due to the graphene film. After battery cycling, R_{ct} of the blank, 10RGO and 100RGO were calculated to be 568 Ω , 331 Ω , and 230 Ω respectively. R_{ct} of the blank and 100RGO seem to be stable after cycling when comparing to their own R_{ct} before cycling. However, R_{ct} of 10RGO has increased significantly

after cycling which suggests that the RGO coating in the interface between the electrolyte and anode surface has changed during cycling. We have observed that 10RGO coating cracks and eventually break apart when dendrites are big enough to pierce through it (figure 52D). Hence after dendrite breaks the 10RGO coating, the anode surface underneath is exposed to the electrolyte. Hence the R_{ct} of 10RGO at that stage will resemble that of the blank sample.

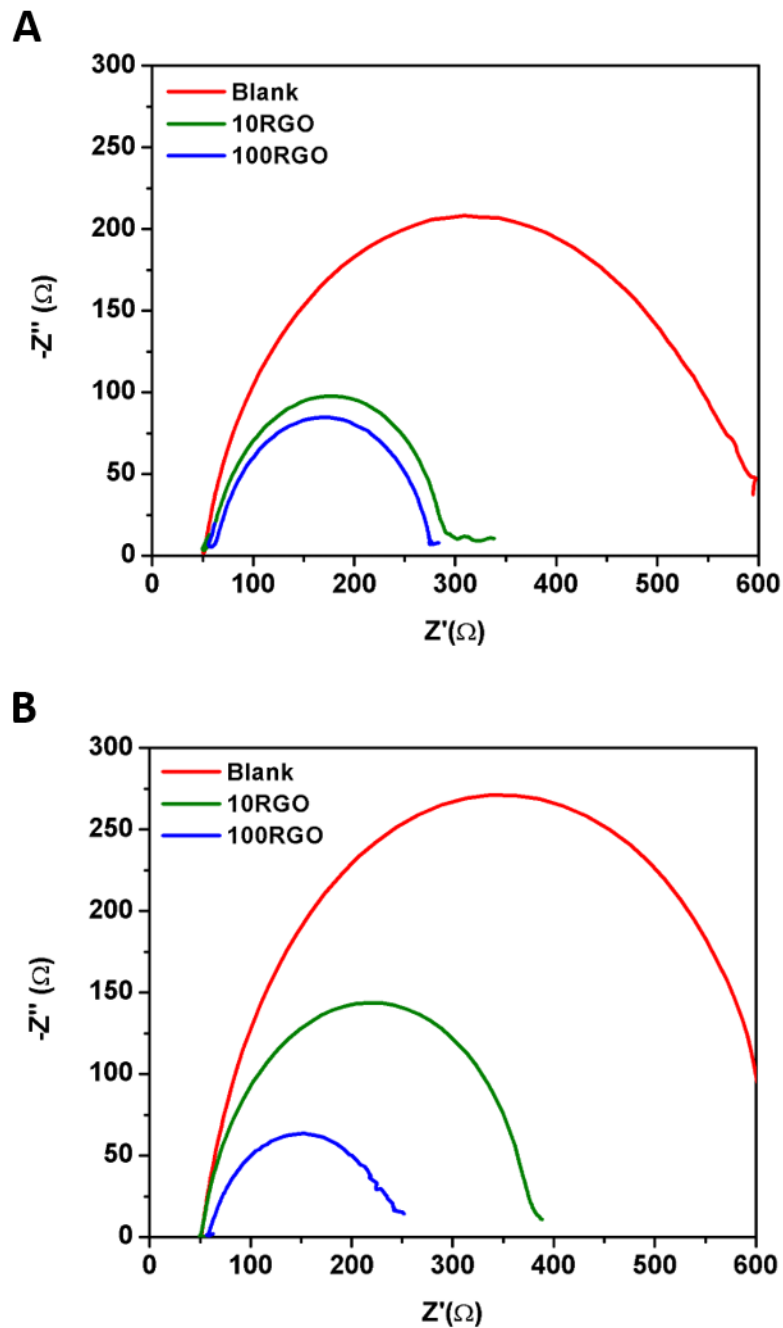


Figure 50: Nyquist plots of blank and RGO coated porous zinc anodes after (A) first cycle and (B) 300 cycles

4.5.2 Scanning Electron Microscope

SEM images of the blank, 10RGO and 100RGO samples were taken to see the difference in dendritic nucleation and growth. Chronoamperometry (CA) in a three-electrode system was

performed to grow the dendrites. First, the nucleation sites of dendrites were grown by performing CA at a time scale (approximately 170 milliseconds) when the samples show the initial current drop in their respective current-time profile (Figure 43). SEM images after dendrite nucleation formation for the blank, 10RGO, and 100RGO samples are shown in Figure 51.

Flake-like dendritic structures are observed on the blank sample. Similar structures are observed on the 10RGO and 100RGO samples in the regions without RGO surface coverage. However, on the areas with RGO surface coverage, dendrites seem to be suppressed in the 10RGO sample. This suppression is more evident in the 100RGO sample, as dendrites are suppressed the underneath the RGO coating.

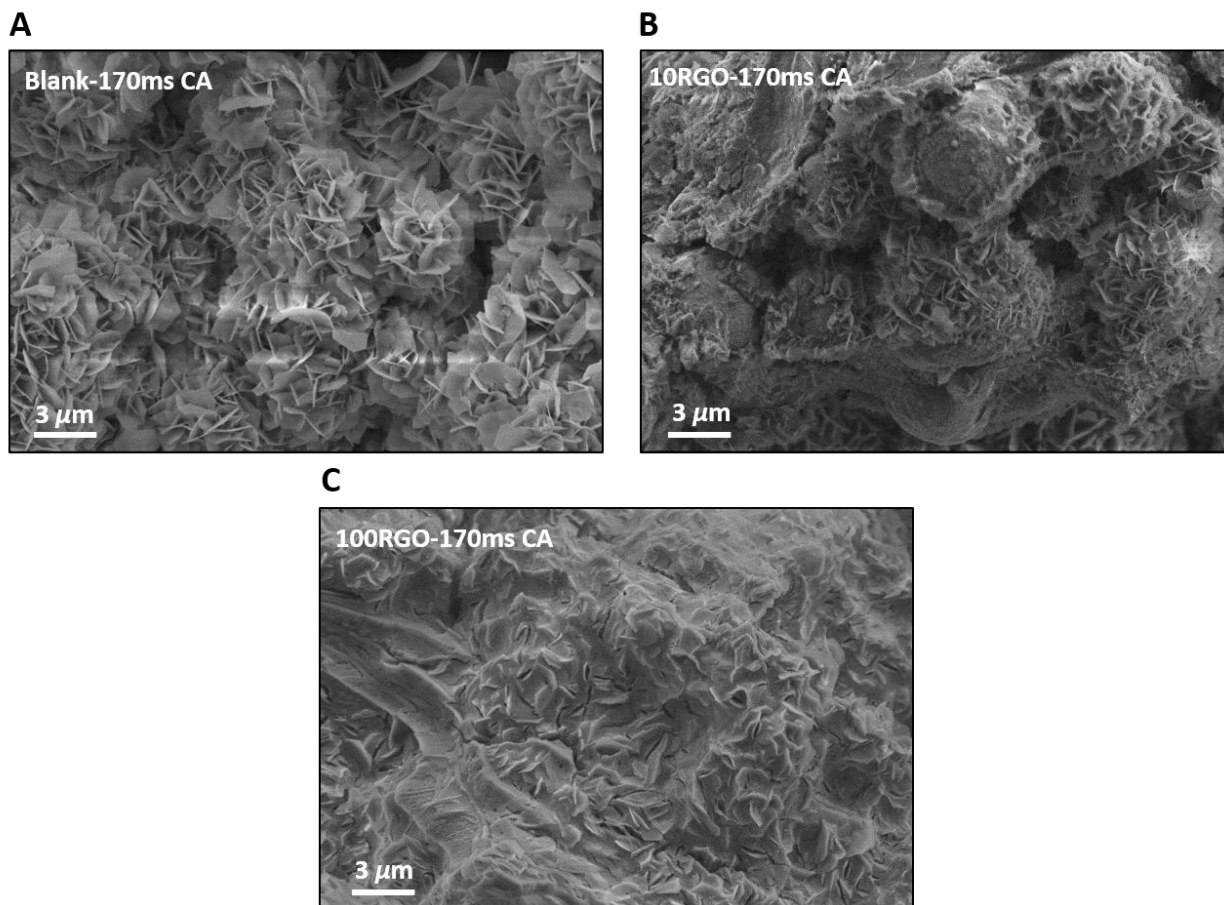


Figure 51: SEM images of (A) blank (B) 10RGO and (C) 100RGO after 170 milliseconds of CA

Next, the CA was performed for 1 hour, and SEM images were taken (Figure 52). For the blank sample, the dendrites seem to have grown into flower-like morphology. Dendritic suppression is observed for the 10RGO and 100RGO samples. However, for 10RGO, cracks are observed in the RGO coating as dendrites pierce through this coating. Cracks and signs of rupture are observed in the de-magnified SEM image of the 10RGO sample after 1 hour of chronoamperometry (Figure 53D). However, the RGO coating in the 100RGO sample seems to be physically intact with no signs of cracks or rupture.

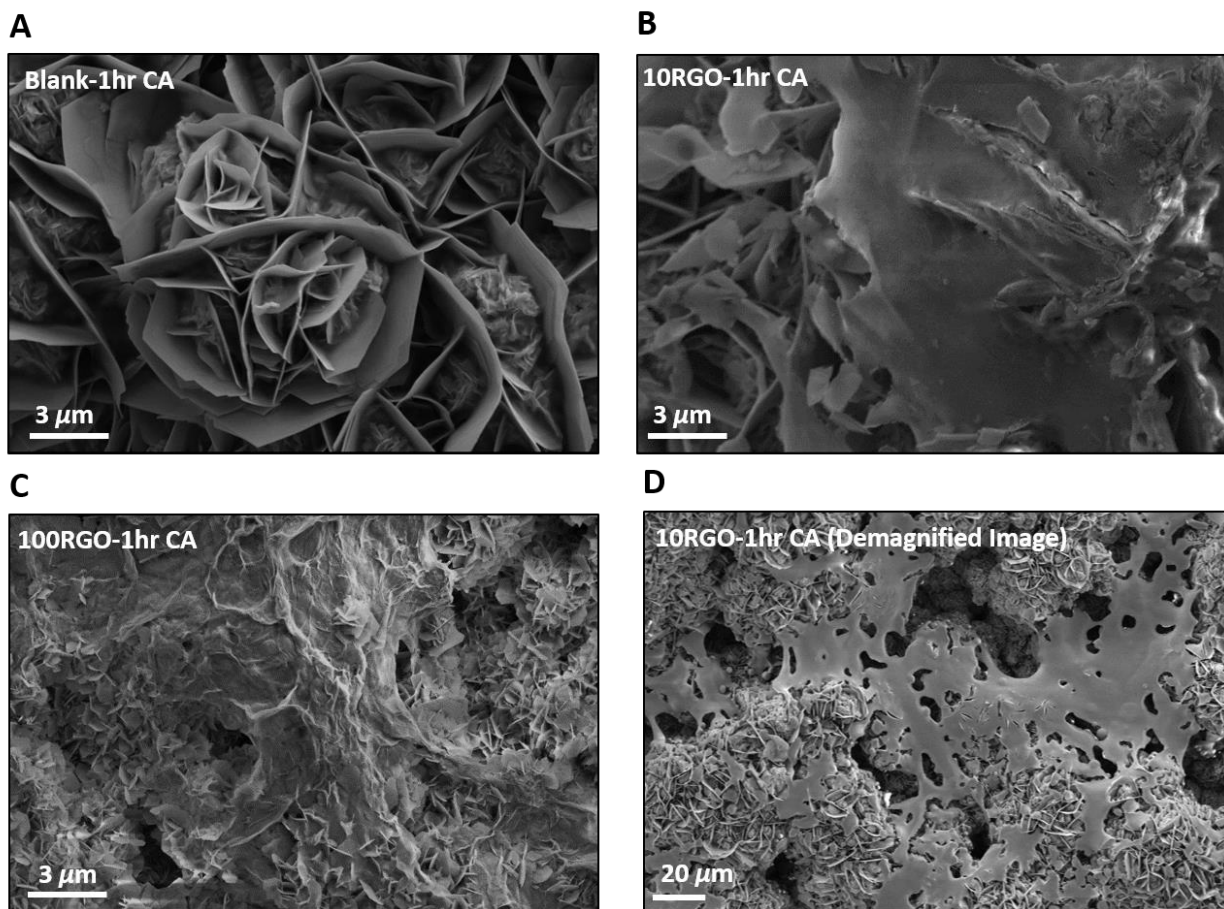


Figure 52: SEM images of (A) blank (B) 10RGO and (C) 100RGO. (D) 10RGO (demagnified) after 1 hr of CA

SEM images of blank and 100RGO after 300 battery cycling were also taken and shown in Figure 53. Again, dendrite suppression is observable on the 100RGO sample. Moreover, there are hexagonal zinc depositions that are relatively parallel to the anode surface. Hence, it is concluded that the RGO coating does not only suppress dendrites but also promote zinc deposition parallel to the anode surface.

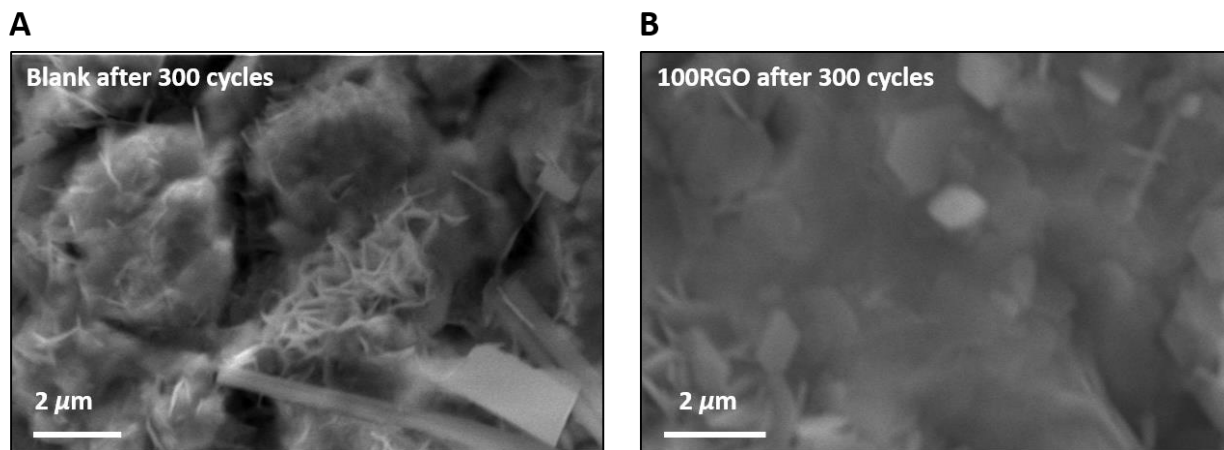


Figure 53: SEM images of (A) blank and (B) 100RGO after 300 battery cycles

Angled SEM was performed on the 100RGO sample before and after 1 hour of CA to observe any changes in RGO coating thickness (Figure 54). A clear thickness increase of RGO coating before (100 nm) and after (500 nm) CA is observed. A close inspection of the SEM image in Figure 54B also reveal that zinc deposition also occurs between the RGO sheets. This hexagonal zinc deposition is parallel to the anode surface.

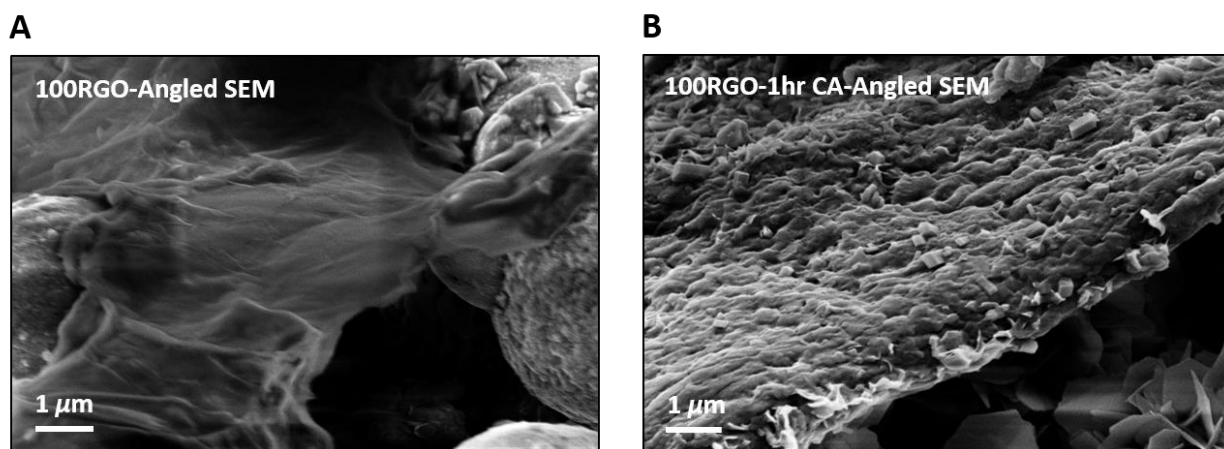


Figure 54: Angled SEM image of 100RGO (A) before and (B) after 1 hour of CA

4.5.3 Raman Spectroscopy

Raman characterization was conducted on the blank, 10RGO, and 100RGO anodes before and after 1 hour of CA (Figure 55). The blank sample does not show the presence of any peaks before and after CA. Moreover, characteristic D and G peaks of graphene were also not observed for 10RGO before CA possibly because of the relatively low thickness of RGO coating. However, after CA, D and G peaks were observed, possibly due to a stronger Raman signal from a thickness increase of RGO coating during CA. This increased D and G signal can also be from surface Plasmon effect of metal (zinc in our case) clusters near the graphene sheets [86]. Hence the presence of deposited zinc clusters on top and between RGO sheets can increase its Raman intensity. An intense D and G peaks were observed for 100RGO before CA. It has been reported in the literature that the intensities of the D and G peaks increase with increasing number of graphene oxide layers [87]. Raman peaks with of G and D peaks of higher intensity were also observed for the 100RGO sample after CA.

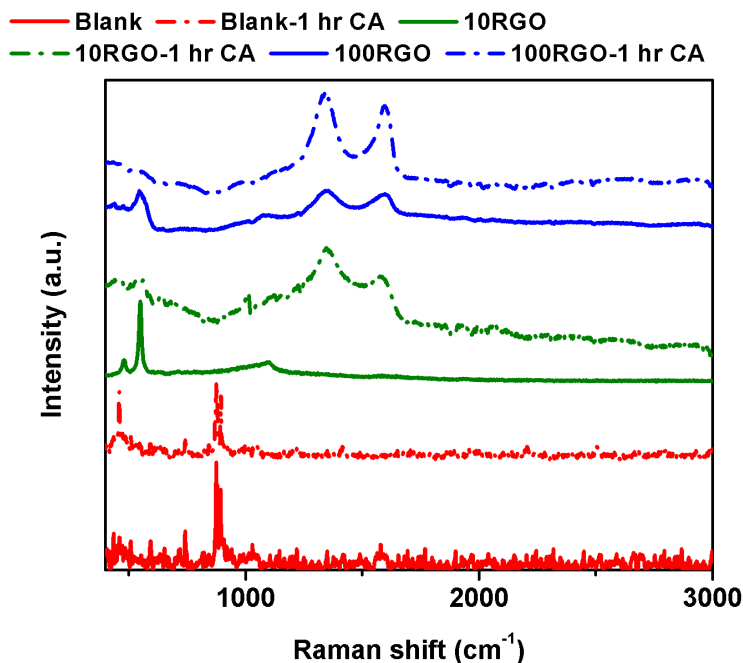


Figure 55: Raman of blank, 10RGO, and 100RGO before and after 1 hour of CA

4.5.4 X-ray Photoelectron Spectroscopy

X-ray photoelectron spectroscopy (XPS) was performed on the blank, and 100RGO samples before and after 1 hour of CA, and 300 battery cycles. A sample XPS spectrum after a quick scan is shown below (Figure 56). Zinc and traces of bismuth and lead (from bismuth oxide and lead oxide respectively) were observed. Detected traces of carbon originates from the polymer binder used to fabricate porous zinc anode and RGO coatings. Oxygen comes from RGO coatings, zinc oxide, bismuth oxide and lead oxide. A summary of the elemental composition of main elements found in these samples is presented in Table 6. Higher zinc composition is evident for the 100RGO sample after CA (20.8 %) and battery cycling (6.6 %) compared to that of blank (9.9 % after CA and 2.9 % after battery cycling). This higher zinc content for the 100RGO sample after CA and battery cycling show that the graphene coating effectively prevents the corrosion of the zinc anode during these respective processes. As previously mentioned, in RGO coated anodes zinc deposition

is observed between the graphene layers. Due to this intercalation of zinc between graphene layers, the deposited zinc is not as exposed to acidic aqueous electrolyte as it is in the blank samples, also explaining higher zinc content.

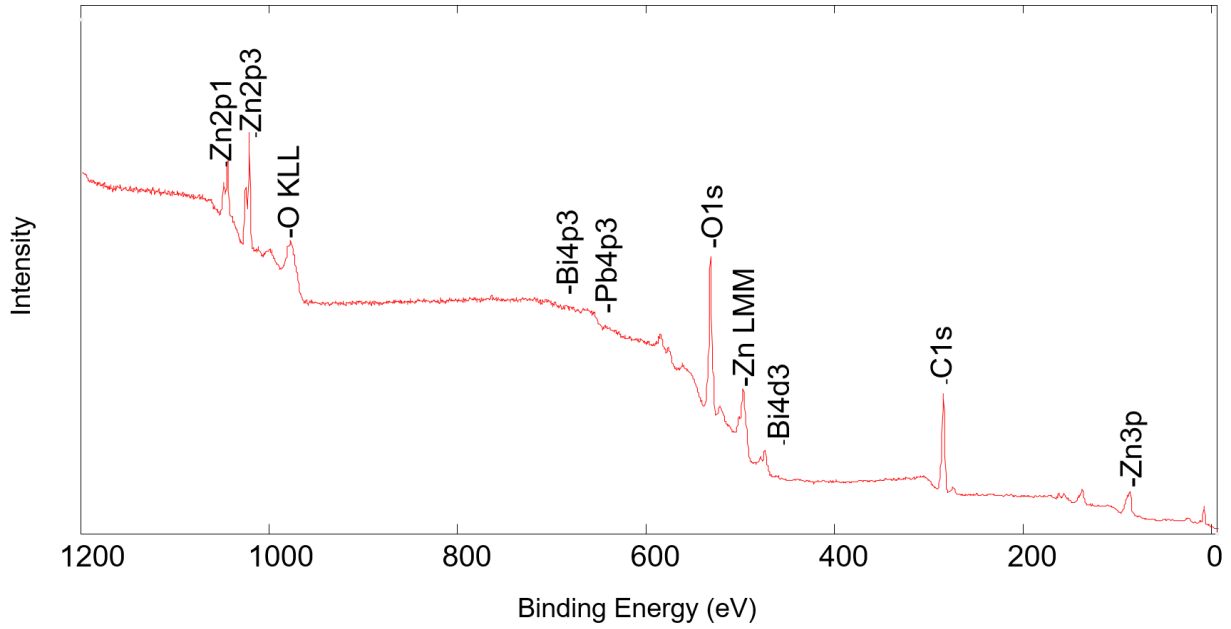


Figure 56: Sample XPS survey

Table 6: Summary of the elemental composition obtained from XPS

Sample	Atomic %		
	Zn 2p3	O 1s	C 1s
Blank	10.8	37.6	51.2
Blank-1hr CA	9.9	42.3	47.6
Blank-300 cycles	2.9	42.7	54.3
100RGO	19.1	37.1	42.6
100RGO-1hr CA	20.8	47.9	30.9
100RGO-300 cycles	6.6	39.7	53.2

A high-resolution XPS spectrum scan of zinc peaks (Zn 2p(3/2)) was also conducted. Deconvolution of Zn 2p (3/2) peaks was done based on a Lorentz-Gauss algorithm, and the result is shown in Figure 57. The deconvolution of Zn 2p (3/2) peaks, based on a Lorentz-Gauss algorithm, show that the blank sample has predominately pure zinc (62.7 % at 1020.1 eV) followed by zinc hydroxide (24.8 % at 1024.3 eV) and zinc oxide (12.5 % at 1022.7 eV). After CA, there is a drastic decrease in pure zinc (8.9 % at 1019.9 eV), while an increase in zinc hydroxide content (50.8 % at 1023 eV), and zinc oxide (40.3 % at 1021.8 eV) content. In the 100RGO sample, deconvolution of Zn 2p (3/2) shows a lower pure zinc content (27.7 % at 1021 eV) and a higher zinc oxide (45.8 % at 1022 eV) and zinc hydroxide (26.5 % at 1023 eV) content than the ones in the blank sample. This composition in the 100RGO sample might be due to Zn(II) binding with oxygen functional groups of RGO ($-\text{COOH} + \text{Zn}^{2+} \rightarrow -\text{COOZn}^{2+} + \text{H}^+$ and $-2\text{OH} + \text{Zn}^{2+} \rightarrow -\text{OZn} + \text{H}^+$) [88]. However, the decrease in pure zinc content (16.3 % at 1019 eV) of the 100RGO sample after

CA is not as severe as that of the blank sample after CA. This situation confirms a more efficient deposition/dissolution of Zn ions/atoms in the presence of graphene coatings.

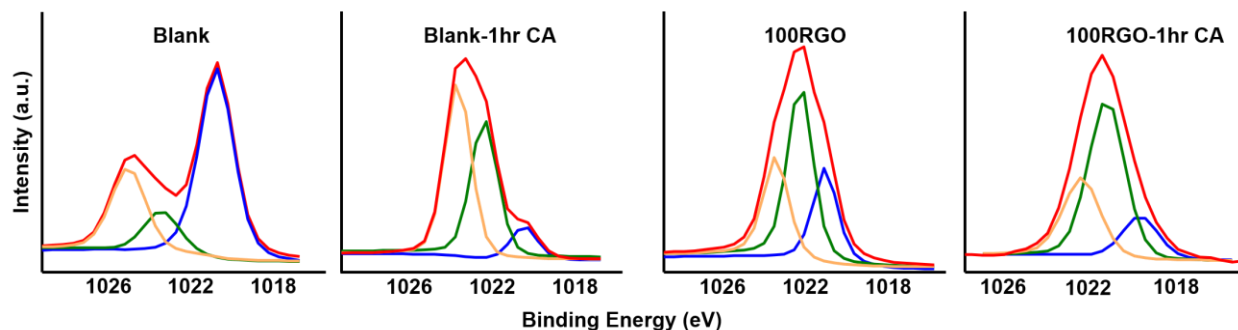


Figure 57: High-resolution XPS of Zn 2p (3/2) of blank and 100RGO before and after 1 hour of CA

4.5.5 Grazing Incidence X-ray Diffraction

GIXRD was performed on the blank, and 100RGO sample to study the zinc crystal growth in different orientations before and after 1 hour of CA. The GIXRD plot is shown in Figure 58. Different planes corresponding to zinc, including (002), (100), (101), (102), (103), and (110) planes, were observed for all samples. These peaks have been reported in the literature [82][89][90]. The peak intensities of all the samples in the figure have been normalized with the (101) peak. The peak corresponding to (101) direction, is dominant in all of the samples. It is relevant to mention that the zinc crystal growth in (002) direction is nearly parallel to the anode surface ($0-30^\circ$ relative to anode surface), while the growth in (101) direction is almost perpendicular to the anode surface ($70-90^\circ$ relative to anode surface) [83]. Since the crystal growth in the (101) direction is perpendicular to the surface, it is associated with dendritic growth. Meanwhile, the crystal growth in (002) direction is preferred since it represents a more-uniform zinc deposition that is parallel to the anode surface. The intensity of (002) plane relative to (101) plane for the 100RGO sample after CA ($I_{002}/I_{101} \sim 0.26$) is higher than that of the blank

($I_{002}/I_{101} \sim 0.20$). Hence, GIXRD suggests that RGO coated anodes promote a more zinc deposition that is parallel to the anode surface than the blank sample does.

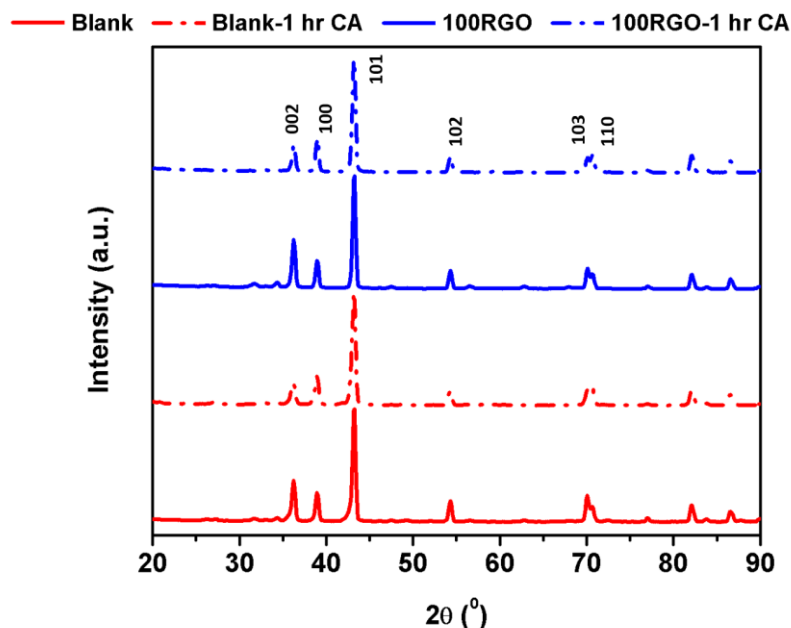


Figure 58: GIXRD characterizations on blank and 100RGO anodes before and after 1 hour of CA

4.6 Conclusions

An artificial (SEI) based on graphene films was successfully introduced on the anode surface in an aqueous lithium battery system with a thickness and area of 1 – 100 nm and 1 – 10 cm², respectively. Porous zinc anode was fabricated using the slurry method. GO was synthesized using improved Hummer's method. Coating technique based on Langmuir trough was used to transfer GO on the porous zinc anode surface. This scalable coating technique allows precise control on the layers of GO that can deposit on the anode surface. The deposited GO films were then reduced to RGO using water vapor. SEM, AFM and contact measurement confirmed the successful coatings of RGO on the anode surface.

The anodes with artificial SEI exhibit lower corrosion current density and dendritic as evident from the Tafel and CA measurements. The aqueous lithium batteries with the RGO-based artificial SEI anodes show a considerable improvement in initial discharge capacity ($102.72 \text{ mA h g}^{-1}$) and cycling stability (82 % after 300 cycles).

SEM images after 1 hour of CA confirmed that dendrites were suppressed underneath the RGO coating in the anodes with artificial SEI. Furthermore, a uniform zinc deposition process was observed in the regions covered with the RGO. SEM and Raman results confirmed an increase in the thickness of the RGO coating after 1 hour of CA, possibly due to the intercalation of the graphene layers by the zinc ions. The EIS measurement also showed a lower charge transfer resistance in the anodes with artificial SEI. Moreover, GIXRD indicates that RGO-based artificial SEI promotes more of a zinc deposition that is parallel to anode surface than the one on the blank sample.

Chapter 5: Summary of Thesis

Batteries provide a versatile means of storing energy in chemical form and are extensively researched and applied in various fields, such as green transportation and energy generation systems. Specifically, aqueous batteries are an attractive alternative to current commercially available batteries because they mitigate most of the economic, ecological, and safety issues posed by commercially available battery systems. A class of aqueous batteries known as the rechargeable hybrid aqueous batteries (ReHABs) uses lithium and zinc as their cathode and anode material, respectively. In particular, zinc is a readily available, cheap material that has the high metal capacity (820 mAh/g), high electronic conductivity, low toxicity, and suitable redox potential. Moreover, ReHABs are safer, cheaper, and easier to assemble and manufacture because they use aqueous electrolyte.

However, ReHABs suffer from poor cycling performance compared to their organic counterparts. One of the main reason for poor cycling performance is that the anode undergoes detrimental oxidation and zinc dendritic growth during cycling. With successive cycling, as the surface of the anode gets oxidized, the electrochemically active surface area of the anode decreases and leads to a loss of capacity. Moreover, sharp dendritic structure grows from the anode surface due to non-uniform zinc deposition during battery charging. With cycling, these dendrites grow taller, can pierce the separator along the way and ultimately make contact with the cathode. This contact leads to short-circuiting and ultimate failure of the battery. Various strategies to overcome this problem in the ReHAB have been reported, including the application of additives in the electrolyte, adding additives on the zinc anode and replacing the aqueous electrolyte with the gel electrolyte. However, these strategies are either expensive or cannot be applied in large-scale battery systems which, limits their use in commercial applications. Furthermore, many literature reports on

minimizing dendritic growth in organic lithium battery systems have been discussed in this thesis (refer to section 1.2.3). The most-worthy mention includes the application of 2D materials as solid electrolyte interface (SEI) on the anode surface. This strategy provides the research motivation for this thesis work.

In this work, an ultra-thin layer of reduced graphene oxide (RGO) or graphene is used as the 2D material for use as an artificial SEI on the anodes of ReHAB systems. Properties of graphene make it an ideal candidate for its use as an artificial SEI (refer to section 1.3.5). It has the high mechanical strength to suppress dendritic growth, has high zinc ion permeation, so it does not impede its movement to and from the anode surface during battery operation. Moreover, it has high chemical stability and hence does not undergo undesirable side reactions.

First, the porous zinc anode is fabricated and implemented in ReHAB battery systems (see Chapter 3). The porous anode fabrication parameters, including the zinc powder types, binder concentrations, and zinc powder particle sizes, were optimized based on their effect on battery cycling performance. Next, the optimized porous anode was compared with a commonly used planar zinc anode. SEM and AFM analysis show that the porous anode provides a higher electrochemically active surface area than the planar anode. Furthermore, contact angle measurements show that the porous anode has a higher wettability compared to the planar anode, which is a desirable anode surface property for aqueous batteries. In the cycling test, batteries with the porous anode show a significantly higher initial discharge capacity ($136.3 \text{ mA h g}^{-1}$ compared to $103.4 \text{ mA h g}^{-1}$ of the planar anode at a current density of 1C) and higher cycling retention (87 % retention compared to 80 % retention of planar anode after 100 cycles). Additionally, batteries with the porous anode show an improvement in rate performance at various C-rates ranging from 0.2C to 2C. This rate performance improvement was also observed in big batteries (7 mA h), which

demonstrates the potential use of the porous anode for large-scale commercial battery applications. Also, float charge and gas evolution tests show that the porous anode undergoes less of the undesirable side-reactions and hence, it generates less gas during cycling. Tafel extrapolation in linear polarization curve and current-time profile show that the porous anode has slightly lower oxidation rate and has significantly higher suppression of dendritic nucleation and growth. CV plot shows higher current density for the porous anode, which corresponds to higher zinc diffusion to and from the porous anode during reduction and oxidation, respectively, due to the presence of larger electrochemically active surface area. XRD shows all the peaks corresponding to zinc before and after chronoamperometry for the planar and porous zinc anodes. It was interesting to note that zinc ions preferably deposited on the (103) plane on the porous anode; this plane direction is relatively flat to the anode surface.

Next, graphene oxide (GO) was coated on the porous zinc anode as artificial solid electrolyte interphase (SEI) for ReHABs (see Chapter 4). GO was synthesized using improved Hummer's method and the porous anode was fabricated using the slurry method. GO with different thicknesses was coated on the porous anode using scalable Langmuir trough technique. GO on the anode surface was then reduced to reduced graphene oxide (RGO) using water vapor exposure. SEM, AFM and contact angle measurements confirmed the successful transfer of GO onto the porous anode surface. Tafel extrapolation and current-time profile showed a significantly lower corrosion rate, and a better zinc dendritic nucleation and growth suppression on RGO coated anodes, respectively. Batteries with an artificial SEI coated anodes show a significant improvement in initial discharge capacity and cycling retention (best cycling performance with 100-layered RGO at initial discharge capacity of $102.72 \text{ mA h g}^{-1}$ and cycling retention of 82 % after 300 cycles under a current density of 4C). SEM images after 1 hour of CA confirmed that

dendrites were suppressed underneath the RGO coatings. Furthermore, a uniform zinc deposition process was observed within the regions covered with RGO coatings. SEM and Raman results confirmed an increase in the thickness of the RGO coating after 1 hour of chronoamperometry, possibly due to the intercalation of the graphene layers by the zinc ions. The EIS measurement also showed a lower charge transfer resistance in the artificial SEI coated anodes. Moreover, GIXRD indicates that the RGO coating promotes zinc deposition that is parallel to the anode surface, as opposed to dendritic deposition.

References

- [1] Avicenne Energy, “No Title,” 2017.
- [2] X. Wu *et al.*, “The electrochemical performance improvement of LiMn₂O₄/Zn based on zinc foil as the current collector and thiourea as an electrolyte additive,” *J. Power Sources*, vol. 300, pp. 453–459, Dec. 2015.
- [3] J. Zhang, C. Chen, X. Zhang, and S. Liu, “Study on the Environmental Risk Assessment of Lead-Acid Batteries,” *Procedia Environ. Sci.*, vol. 31, pp. 873–879, Jan. 2016.
- [4] G. Majeau-Bettez, T. R. Hawkins, and A. Hammer Strømman, “Life Cycle Environmental Assessment of Lithium-Ion and Nickel Metal Hydride Batteries for Plug-In Hybrid and Battery Electric Vehicles,” *Environ. Sci. Technol.*, vol. 45, pp. 4548–4554, 2011.
- [5] X. Wu *et al.*, “The electrochemical performance improvement of LiMn₂O₄/Zn based on zinc foil as the current collector and thiourea as an electrolyte additive,” *J. Power Sources*, vol. 300, pp. 453–459, 2015.
- [6] Z. Chang *et al.*, “A lithium ion battery using an aqueous electrolyte solution,” *Sci. Rep.*, vol. 6, no. 1, p. 28421, Sep. 2016.
- [7] J. Yan, J. Wang, H. Liu, Z. Bakenov, D. Gosselink, and P. Chen, “Rechargeable hybrid aqueous batteries,” *J. Power Sources*, vol. 216, pp. 222–226, 2012.
- [8] *Fundamental Aspects of Electrometallurgy*. Boston: Kluwer Academic Publishers, 2002.
- [9] M. M. Thackeray, P. J. Johnson, L. A. de Picciotto, P. G. Bruce, and J. B. Goodenough, “Electrochemical extraction of lithium from LiMn₂O₄,” *Mater. Res. Bull.*, vol. 19, no. 2, pp. 179–187, Feb. 1984.
- [10] X. Sun, X. Q. Yang, M. Balasubramanian, J. Mcbreen, Y. Xia, and T. Sakai, “In Situ Investigation of Phase Transitions of Li_{1-y}Mn₂O₄ Spinel during Li-Ion Extraction and Insertion,” 2002.
- [11] X. Zhu, T. Hoang, and P. Chen, “Novel Carbon Materials in the Cathode Formulation for High Rate Rechargeable Hybrid Aqueous Batteries,” *Energies*, vol. 10, no. 11, p. 1844, Nov. 2017.
- [12] N. Alias and A. A. Mohamad, “Morphology study of electrodeposited zinc from zinc sulfate solutions as anode for zinc-air and zinc-carbon batteries,” *J. King Saud Univ. - Eng. Sci.*, vol. 27, no. 1, pp. 43–48, Jan. 2015.
- [13] K. E. K. Sun *et al.*, “Suppression of Dendrite Formation and Corrosion on Zinc Anode of Secondary Aqueous Batteries,” *ACS Appl. Mater. Interfaces*, vol. 9, no. 11, pp. 9681–9687, Mar. 2017.
- [14] C. A. Loto, “Electrodeposition of Zinc from Acid Based Solutions: A Review and Experimental Study,” *Asian J. Appl. Sci.*, vol. 5, no. 6, pp. 314–326, Jun. 2012.

- [15] K. Wongrujipairoj, L. Poolnapol, A. Arpornwichanop, S. Suren, and S. Kheawhom, "Suppression of zinc anode corrosion for printed flexible zinc-air battery," *Phys. status solidi*, vol. 254, no. 2, p. 1600442, Feb. 2017.
- [16] S. Higashi, S. W. Lee, J. S. Lee, K. Takechi, and Y. Cui, "Avoiding short circuits from zinc metal dendrites in anode by backside-plating configuration," *Nat. Commun.*, vol. 7, p. 11801, Jun. 2016.
- [17] A. Mitha, A. Z. Yazdi, M. Ahmed, and P. Chen, "Surface Adsorption of Polyethylene Glycol to Suppress Dendrite Formation on Zinc Anodes in Rechargeable Aqueous Batteries," *ChemElectroChem*, Jun. 2018.
- [18] T. K. A. Hoang *et al.*, "Sustainable Gel Electrolyte Containing Pyrazole as Corrosion Inhibitor and Dendrite Suppressor for Aqueous Zn/LiMn₂O₄ Battery," *ChemSusChem*, vol. 10, no. 13, pp. 2816–2822, Jul. 2017.
- [19] T. K. A. Hoang, M. Acton, H. T. H. Chen, Y. Huang, T. N. L. Doan, and P. Chen, "Sustainable gel electrolyte containing Pb²⁺ as corrosion inhibitor and dendrite suppressor for the zinc anode in the rechargeable hybrid aqueous battery," *Mater. Today Energy*, 2017.
- [20] Y. M. Lee, J. E. Seo, Y.-G. Lee, S. H. Lee, K. Y. Cho, and J.-K. Park, "Effects of Triacetoxymethylsilane as SEI Layer Additive on Electrochemical Performance of Lithium Metal Secondary Battery," *Electrochem. Solid-State Lett.*, vol. 10, no. 9, p. A216, Sep. 2007.
- [21] F. Ding *et al.*, "Dendrite-free lithium deposition via self-healing electrostatic shield mechanism," *J. Am. Chem. Soc.*, vol. 135, no. 11, pp. 4450–4456, Mar. 2013.
- [22] K. Yan *et al.*, "Ultrathin Two-Dimensional Atomic Crystals as Stable Interfacial Layer for Improvement of Lithium Metal Anode," *Nano Lett.*, vol. 14, no. 10, pp. 6016–6022, Aug. 2014.
- [23] K. Park *et al.*, "New battery strategies with a polymer/Al₂O₃ separator," *J. Power Sources*, vol. 263, pp. 52–58, Oct. 2014.
- [24] Z. Tu, Y. Kambe, Y. Lu, and L. A. Archer, "Nanoporous Polymer-Ceramic Composite Electrolytes for Lithium Metal Batteries," *Adv. Energy Mater.*, vol. 4, no. 2, p. n/a-n/a, 2014.
- [25] Z. Wang *et al.*, "Self-Assembly of PEI/SiO₂ on Polyethylene Separators for Li-Ion Batteries with Enhanced Rate Capability," *ACS Appl. Mater. Interfaces*, vol. 7, no. 5, pp. 3314–3322, Feb. 2015.
- [26] W.-K. Shin, A. G. Kannan, and D.-W. Kim, "Effective Suppression of Dendritic Lithium Growth Using an Ultrathin Coating of Nitrogen and Sulfur Codoped Graphene Nanosheets on Polymer Separator for Lithium Metal Batteries," *ACS Appl. Mater. Interfaces*, vol. 7, no. 42, pp. 23700–23707, 2015.
- [27] T. Foroozan *et al.*, "Synergistic Effect of Graphene Oxide for Impeding the Dendritic Plating of Li," *Adv. Funct. Mater.*, vol. 28, no. 15, p. 1705917, Apr. 2018.

- [28] S. C. Ray, *Applications of graphene and graphene-oxide based nanomaterials*. .
- [29] D. R. Dreyer, A. D. Todd, and C. W. Bielawski, "Harnessing the chemistry of graphene oxide," *Chem. Soc. Rev.*, vol. 43, no. 15, p. 5288, Jul. 2014.
- [30] H. He, J. Klinowski, M. Forster, and A. Lerf, "A new structural model for graphite oxide," *Chem. Phys. Lett.*, vol. 287, no. 1–2, pp. 53–56, Apr. 1998.
- [31] B. C. Brodie, "On the Atomic Weight of Graphite," *Philos. Trans. R. Soc. London*, vol. 149, no. 0, pp. 249–259, Jan. 1859.
- [32] L. Staudenmaier, "Verfahren zur Darstellung der Graphitsäure," *Berichte der Dtsch. Chem. Gesellschaft*, vol. 31, no. 2, pp. 1481–1487, May 1898.
- [33] W. S. Hummers and R. E. Offeman, "Preparation of Graphitic Oxide," *J. Am. Chem. Soc.*, vol. 80, no. 6, pp. 1339–1339, Mar. 1958.
- [34] D. C. Marcano *et al.*, "Improved synthesis of graphene oxide," *ACS Nano*, 2010.
- [35] A. M. Dimiev and J. M. Tour, "Mechanism of Graphene Oxide Formation," *ACS Nano*, vol. 8, no. 3, pp. 3060–3068, Mar. 2014.
- [36] H. C. Schniepp *et al.*, "Functionalized single graphene sheets derived from splitting graphite oxide," *J. Phys. Chem. B*, 2006.
- [37] C. Mattevi *et al.*, "Evolution of electrical, chemical, and structural properties of transparent and conducting chemically derived graphene thin films," *Adv. Funct. Mater.*, 2009.
- [38] K. H. Liao, A. Mittal, S. Bose, C. Leighton, K. A. Mkhoyan, and C. W. MacOsco, "Aqueous only route toward graphene from graphite oxide," *ACS Nano*, 2011.
- [39] S. Pei and H.-M. Cheng, "The reduction of graphene oxide," *Carbon N. Y.*, vol. 50, no. 9, pp. 3210–3228, Aug. 2012.
- [40] C. Ramakrishnan Minitha, V. Sukumaran Anithaa, V. Subramaniam, and R. Thangavelu Rajendra Kumar, "Impact of Oxygen Functional Groups on Reduced Graphene Oxide-Based Sensors for Ammonia and Toluene Detection at Room Temperature."
- [41] O. C. Compton and S. T. Nguyen, "Graphene Oxide, Highly Reduced Graphene Oxide, and Graphene: Versatile Building Blocks for Carbon-Based Materials," *Small*, vol. 6, no. 6, pp. 711–723, Mar. 2010.
- [42] L. Suo *et al.*, "How Solid-Electrolyte Interphase Forms in Aqueous Electrolytes."
- [43] E. Peled and S. Menkin, "Review—SEI: Past, Present and Future," *J. Electrochem. Soc.*, vol. 164, no. 7, pp. A1703–A1719, Jun. 2017.
- [44] W. Primak and L. H. Fuchs, "Electrical Conductivities of Natural Graphite Crystals," *Phys. Rev.*, vol. 95, no. 1, pp. 22–30, Jul. 1954.
- [45] C. Gó Mez-Navarro *et al.*, "Electronic Transport Properties of Individual Chemically

Reduced Graphene Oxide Sheets.”

- [46] J. W. Suk, R. D. Piner, J. An, and R. S. Ruoff, “Mechanical Properties of Monolayer Graphene Oxide,” *ACS Nano*, vol. 4, no. 11, pp. 6557–6564, 2010.
- [47] R. K. Joshi *et al.*, “Precise and Ultrafast Molecular Sieving Through Graphene Oxide Membranes,” *Science (80-.)*, vol. 343, no. 6172, pp. 752–754, 2014.
- [48] F. -Cl -Br -I -, “Ca 2+ Ba 2+ Variation in hydrated radius of ions,” *Geochim. Cosmochim. Acta*, pp. 61–3331, 1981.
- [49] O. C. Wells, *Scanning electron microscopy*. McGraw-Hill, 1974.
- [50] “Scanning Electron Microscopy | Central Microscopy Research Facility.” [Online]. Available: <https://cmrf.research.uiowa.edu/scanning-electron-microscopy>. [Accessed: 01-Jul-2018].
- [51] N. Jalili and K. Laxminarayana, “A review of atomic force microscopy imaging systems: application to molecular metrology and biological sciences,” *Mechatronics*, vol. 14, no. 8, pp. 907–945, Oct. 2004.
- [52] D. Pang, A. R. Thierry, and A. Dritschilo, “DNA studies using atomic force microscopy: capabilities for measurement of short DNA fragments.,” *Front. Mol. Biosci.*, vol. 2, p. 1, 2015.
- [53] R. R. L. De, D. A. C. Albuquerque, T. G. S. Cruz, F. M. Yamaji, and F. L. Leite, “Measurement of the Nanoscale Roughness by Atomic Force Microscopy: Basic Principles and Applications,” in *Atomic Force Microscopy - Imaging, Measuring and Manipulating Surfaces at the Atomic Scale*, InTech, 2012.
- [54] M. Raposo, Q. Ferreira, and P. a Ribeiro, “A Guide for Atomic Force Microscopy Analysis of Soft- Condensed Matter,” *Mod. Res. Educ. Top. Microsc.*, 2007.
- [55] “Heavy Mineral Sand Analysis for Industrial Process Control - Used Screeners.” [Online]. Available: <http://www.usedscreeners.com/news/heavymineralsandanalysisforindustrialprocesscontrol>. [Accessed: 01-Jul-2018].
- [56] “X-ray diffraction method.” [Online]. Available: <https://textilestudycenter.com/x-ray-diffraction-method/>. [Accessed: 01-Jul-2018].
- [57] U. Welzel, J. Ligot, P. Lamparter, A. C. Vermeulen, and E. J. Mittemeijer, “Stress analysis of polycrystalline thin films and surface regions by X-ray diffraction,” *J. Appl. Cryst. J. Appl. Cryst*, vol. 38, no. 38, pp. 1–29, 2005.
- [58] N. Widjonarko, “Introduction to Advanced X-ray Diffraction Techniques for Polymeric Thin Films,” *Coatings*, 2016.
- [59] “Principle of X-ray photoelectron spectroscopy (XPS) | TikZ example.” [Online]. Available: <http://www.texample.net/tikz/examples/principle-of-x-ray-photoelectron->

- spectroscopy-xps/. [Accessed: 01-Jul-2018].
- [60] G. S. Bumbrah and R. M. Sharma, "Raman spectroscopy – Basic principle, instrumentation and selected applications for the characterization of drugs of abuse," *Egypt. J. Forensic Sci.*, vol. 6, no. 3, pp. 209–215, Sep. 2016.
- [61] "The Raman Spectrophotometer." [Online]. Available: <https://www.sas.upenn.edu/~crulli/TheRamanSpectrophotometer.html>. [Accessed: 01-Jul-2018].
- [62] A. C. Ferrari, "Raman spectroscopy of graphene and graphite: Disorder, electron–phonon coupling, doping and nonadiabatic effects," *Solid State Commun.*, vol. 143, no. 1–2, pp. 47–57, Jul. 2007.
- [63] Natarajan, "Advances in Corrosion Engineering," 2014.
- [64] X. Zhang, G. Xiao, B. Liu, C. Jiang, and Y. Lu, "Influence of processing time on the phase, microstructure and electrochemical properties of hopeite coating on stainless steel by chemical conversion method," *New J. Chem.*, vol. 39, no. 7, pp. 5813–5822, Jun. 2015.
- [65] A. J. Bard and L. R. Faulkner, *Electrochemical methods : fundamentals and applications*. Wiley, 1980.
- [66] B.-Y. Chang and S.-M. Park, "Electrochemical Impedance Spectroscopy," *Annu. Rev. Anal. Chem.*, vol. 3, no. 1, pp. 207–229, Jun. 2010.
- [67] E. P. Randviir and C. E. Banks, "Electrochemical impedance spectroscopy: an overview of bioanalytical applications."
- [68] N. Elgrishi, K. J. Rountree, B. D. Mccarthy, E. S. Rountree, T. T. Eisenhart, and J. L. Dempsey, "A Practical Beginner's Guide to Cyclic Voltammetry."
- [69] M. Minakshi, D. Appadoo, and D. E. Martin, "The Anodic Behavior of Planar and Porous Zinc Electrodes in Alkaline Electrolyte," *Electrochem. Solid-State Lett.*, vol. 13, no. 7, pp. A77–A80, Jul. 2010.
- [70] H. Li *et al.*, "Enhancement on Cycle Performance of Zn Anodes by Activated Carbon Modification for Neutral Rechargeable Zinc Ion Batteries," *J. Electrochem. Soc.*, vol. 162, no. 8, pp. A1439–A1444, Jan. 2015.
- [71] H. Tao, X. Tong, L. Gan, S. Zhang, X. Zhang, and X. Liu, "Effect of adding various carbon additives to porous zinc anode in rechargeable hybrid aqueous battery," *J. Alloys Compd.*, vol. 658, pp. 119–124, Feb. 2016.
- [72] C. W. Lee, K. Sathiyarayanan, S. W. Eom, H. S. Kim, and M. S. Yun, "Effect of additives on the electrochemical behaviour of zinc anodes for zinc/air fuel cells," *J. Power Sources*, vol. 160, pp. 161–164, 2006.
- [73] M. Minakshi and D. R. G. Mitchell, "The influence of bismuth oxide doping on the rechargeability of aqueous cells using MnO₂ cathode and LiOH electrolyte," *Electrochim.*

Acta, vol. 53, no. 22, pp. 6323–6327, Sep. 2008.

- [74] J. Phillips, S. Mohanta, C. Maske, D. Bose, J. Wu, and McKinney Bryan, “Pasted zinc electrode for rechargeable nickel-zinc batteries,” 18-May-2009.
- [75] Y. Li and H. Dai, “Recent advances in zinc–air batteries,” *Chem. Soc. Rev.*, vol. 43, no. 15, pp. 5257–5275, Jul. 2014.
- [76] J. Huang and Z. Yang, “A one-pot method to prepare a ZnO/Ag/polypyrrole composite for zinc alkaline secondary batteries,” *RSC Adv.*, vol. 5, no. 43, pp. 33814–33817, Apr. 2015.
- [77] A. Konarov, D. Gosselink, Y. Zhang, Y. Tian, D. Askhatova, and P. Chen, “Self-Discharge of Rechargeable Hybrid Aqueous Battery,” *ECS Electrochem. Lett.*, vol. 4, no. 12, pp. A151–A154, Nov. 2015.
- [78] Y. Wang *et al.*, “High-Capacity and Long-Cycle Life Aqueous Rechargeable Lithium- Ion Battery with the FePO₄ Anode.”
- [79] R. Articles, “Electrodeposition of copper : the nucleation,” vol. 47, pp. 45–47, 2010.
- [80] S. J. Banik and R. Akolkar, “Suppressing Dendrite Growth during Zinc Electrodeposition by PEG-200 Additive,” *J. Electrochem. Soc.*, vol. 160, no. 11, pp. 519–523, 2013.
- [81] D. Menshykau and R. G. Compton, “The Influence of Electrode Porosity on Diffusional Cyclic Voltammetry.”
- [82] N. Pistofidis, G. Vourlias, D. Chaliampalias, G. Stergioudis, and E. K. Polychroniadis, “A combined microscopical and XRD study of zinc coatings,” *Solid State Phenom.*, vol. 163, pp. 93–96, 2010.
- [83] D. J. Mackinnon, J. M. Brannen, and P. L. Fenn, “Characterization of impurity effects in zinc electrowinning from industrial acid sulphate electrolyte,” *J. Appl. Electrochem.*, vol. 17, pp. 1129–1143, 1987.
- [84] K. Instruments, “Operation Manual: LB device.” KSV Instruments.
- [85] D. Prasai, J. C. Tuberquia, R. R. Harl, G. K. Jennings, and K. I. Bolotin, “Graphene: Corrosion-Inhibiting Coating,” *ACS Nano*, vol. 6, no. 2, pp. 1102–1108, Feb. 2012.
- [86] P. Wang, D. Zhang, L. Zhang, and Y. Fang, “The SERS study of graphene deposited by gold nanoparticles with 785 nm excitation,” *Chem. Phys. Lett.*, vol. 556, pp. 146–150, Jan. 2013.
- [87] D. Kostiuik *et al.*, “Reliable determination of the few-layer graphene oxide thickness using Raman spectroscopy,” *J. Raman Spectrosc.*, vol. 47, no. 4, pp. 391–394, Apr. 2016.
- [88] Q. Yang, G. Yang, W. Peng, and S. Song, “Adsorption of Zn(II) on graphene oxide prepared from low-purity of amorphous graphite,” *Surf. Interface Anal.*, vol. 49, no. 5, pp. 398–404, May 2017.
- [89] A. Gomes and M. I. da Silva Pereira, “Pulsed electrodeposition of Zn in the presence of

- surfactants,” *Electrochim. Acta*, vol. 51, no. 7, pp. 1342–1350, Jan. 2006.
- [90] K. O. Nayana and T. V. Venkatesha, “Bright zinc electrodeposition and study of influence of synergistic interaction of additives on coating properties,” *J. Ind. Eng. Chem.*, vol. 26, pp. 107–115, Jun. 2015.
- [91] J. Zhi, A. Z. Yazdi, G. Valappil, J. Haime, and P. Chen, “Artificial solid electrolyte interphase for aqueous lithium energy storage systems,” *Sci. Adv.*, vol. 3, no. 9, p. e1701010, Sep. 2017.

Appendix

Appendix A: AFM Nano-indentation of graphene oxide (GO) layer

Graphene oxide (GO) solution in water (30 ml of 1 mg/ml GO solution) was coated on glass fiber substrate via vacuum filtration. AFM nanoindentation was performed on GO coating to measure its modulus. The modulus was measured at each point over a scan area and the modulus range obtained is tabulated below. Antimony (n) doped silicon tip was used for these measurements. The modulus of control (substrate) sample is lower than the minimum detectable modulus of the tip. The modulus of the GO coating was measured in the range of 4-5 GPa.

Table 7: Modulus of control (substrate) and GO coating

Sample	Modulus (GPa)
Control (substrate without GO coating)	0
GO coating on a substrate	4-5

Appendix B: Rate performance of planar and porous zinc anode in 7 mAh batteries

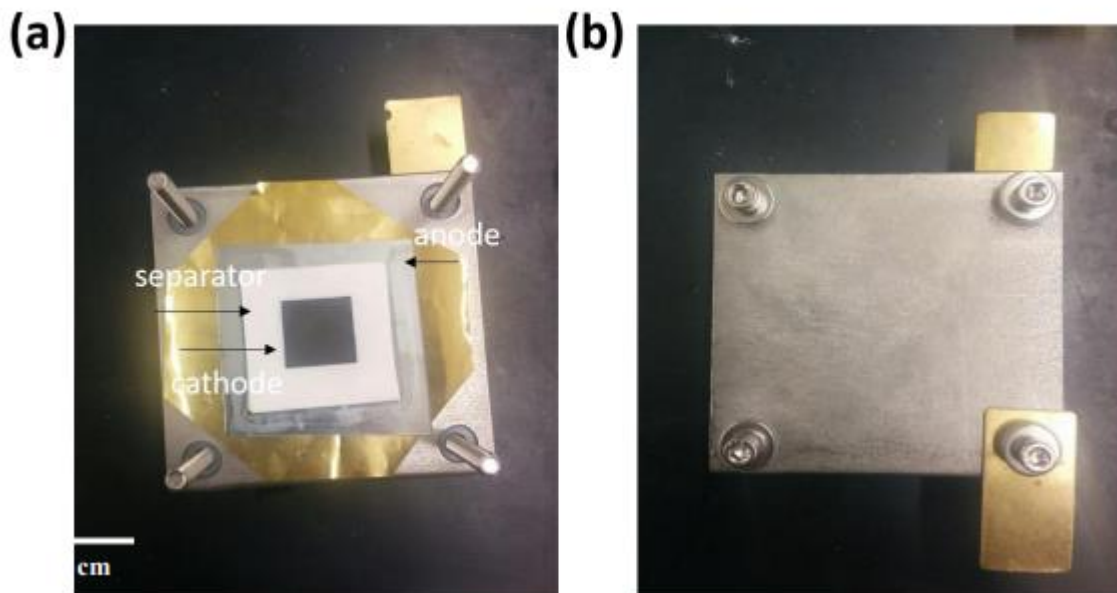


Figure 59: Picture showing (a) inner and (b) outer part of 7 mAh battery with a cathode surface area of 9cm^2 [91]

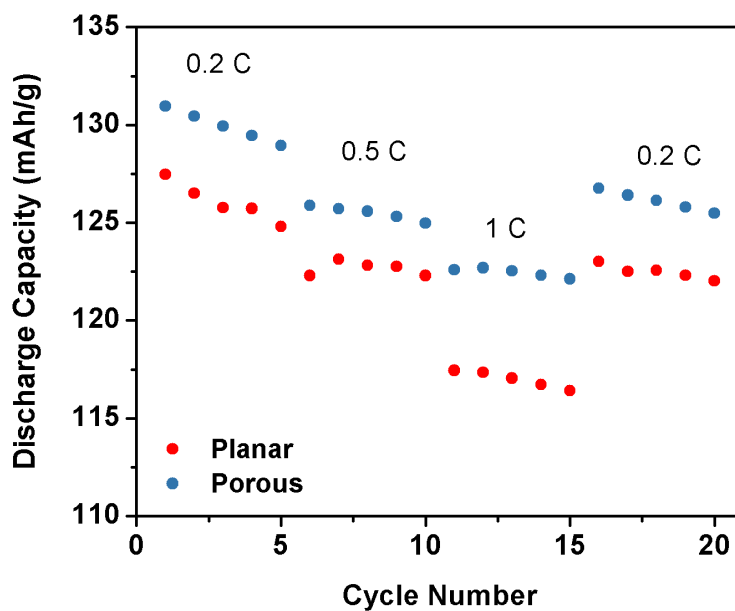


Figure 60: Discharge capacity at different C rates of planar and porous zinc anodes in 7 mAh batteries

Appendix C: Gas evolution test apparatus

A



B



Figure 61: (A) inside and (B) outside of gas evolution apparatus

Appendix D: XRD of porous anode before and after water vapor exposure

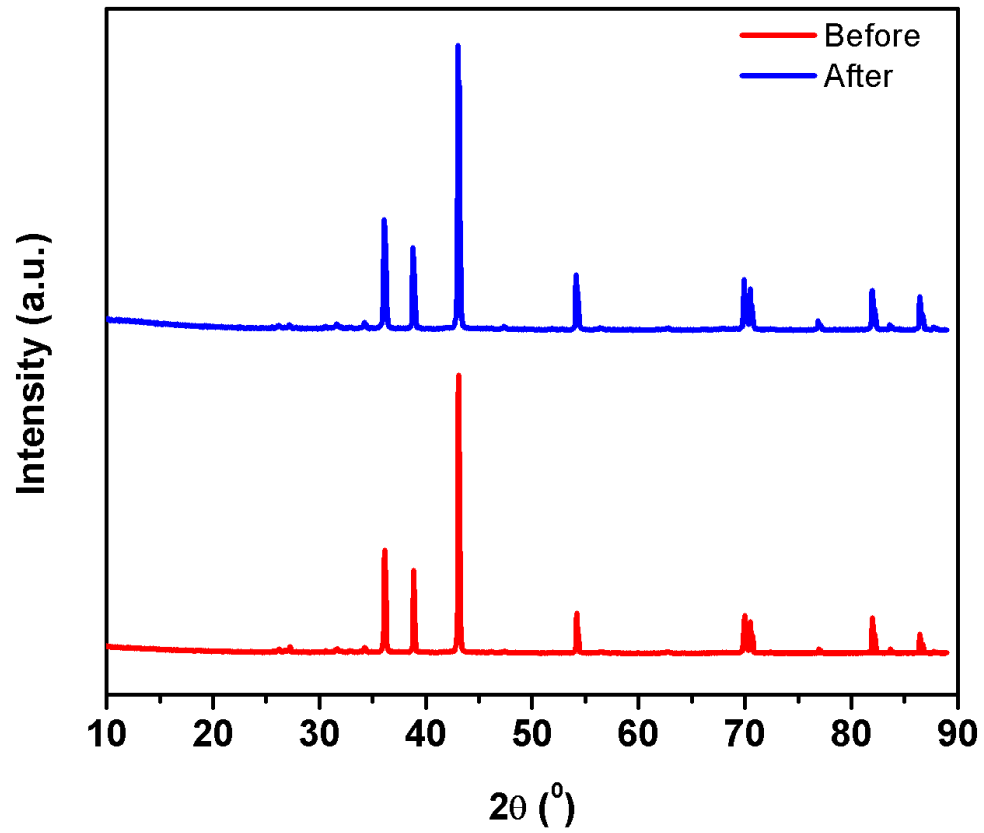


Figure 62: XRD of the porous anode before and after 5 hrs of water vapor exposure